Piezoelectric degradation and circuit protection in fibre Bragg grating and piezoelectric stack based low voltage transducers

Lloyd Clayburn

Institute for Energy and Environment, Electronic and Electrical Engineering

University of Strathclyde, Glasgow

lloyd.clayburn@strath.ac.uk

A thesis submitted in partial satisfaction of the requirements for the degree of MPhil

in the EEE department of the University of Strathclyde

August 17, 2018

This thesis is the result of the author's original research. It has been composed by the author and has not been previously submitted for examination which has led to the award of a degree.

Signed: Lloyd Clayburn

August 17, 2018

Abstract

With rising global electricity demand and increasing penetration of intermittent renewable energy sources, monitoring and protection of power networks is increasingly important for transmission and distribution network operators. It is, therefore, desirable to increase the coverage of, and reduce the cost per unit of monitoring systems. Fibre optic based transducers present a low cost, multiplex-able alternative to conventional methods of current and voltage measurement for monitoring and protection of power networks, however, prior to adoption by industry, it is desirable to characterise and improve sensor accuracy as much as possible. This thesis presents an investigation of several factors affecting the accuracy of piezoelectric stack and fibre Bragg grating based low voltage sensors in particular, with a focus on piezoelectric behaviour in the immediate aftermath of a grid fault, with the aim of developing engineering solutions to maximise sensor accuracy.

Fiber Bragg grating technology is introduced and applications are highlighted. Conventional and proposed voltage and current sensors are described and the advantages of fibre Bragg grating based voltage and current sensors elucidated. The phenomena of piezoelectric ageing, creep and fatigue are reviewed. The effects of piezoelectric degradation on the measurement accuracy of optical fibre and piezoelectric stack based low voltage transducers (LVTs) were experimentally investigated. An accelerated life test to determine the most fatigue resistant bonding method for connecting fibre Bragg gratings to the piezoelectric transducer is discussed. Finally, the proposed protection circuitry for the prototype LVT is revised, based on experimental and theoretical considerations.

Acknowledgements

Firstly, I'd like to thank Dr Paweł Niewczas for his encouragement, guidance and for providing me with the opportunity to undertake this interesting project.

Special thanks are also due to Dr Philip Orr and Dr Neil Gordon of Synaptec for their support and great interest in discussions regarding piezoelectric stack behaviour.

Thanks very much to Dr Grzegorz Fusiek, particularly for discussions regarding the protection circuit design review.

Thanks to Dr Paul Wright at National Physical Laboratory (NPL) for inviting me conduct this research in the first place, and for his enthusiasm in discussing the project subsequently.

Finally, thanks to rest of the Advanced Sensors Team for making my time at Strathclyde an interesting and enjoyable one.

This project was funded by the University of Strathclyde and NPL.

Overview

Fibre optics based current and voltage sensors have the potential to replace conventional electrical sensors on the power grid, but there are still challenges to overcome. This thesis consists of a review of the literature on piezoelectric ageing and fatigue, and experimental investigations into their effect on the measurement accuracy of low voltage transducers (LVTs) comprising piezoelectric stacks and fibre Bragg gratings (FBGs), followed by a thorough design review of a protection circuit for current sensors using said LVTs.

Chapter 1 provides an introduction to fibre Bragg gratings and a broad view of their sensing applications. Existing current and voltage sensor designs are reviewed and the operation of FBG-based current and voltage sensors introduced. The inverse piezoelectric effect is introduced, and an explanation as to how piezoelectric hysteresis is compensated for is presented. A review of piezoelectric degradation mechanisms and the accuracy requirements of the most relevant standard to the LVTs are presented.

In Chapter 2, extensive experimental investigations of piezoelectric degradation in FBG and piezoelectric stack based LVTs are discussed, along with other effects arising as a result of hysteresis. The conditions required to initiate piezoelectric *ageing* and *deageing* are investigated. The dependence of the piezoelectric ageing rate on frequency, grid fault transient voltage magnitude and pulse duration are investigated and the repeatability of degradation in the piezoelectric constant analysed. A piezoelectric constant degradation

compensation procedure is presented, the change in remnant polarisation of the stack throughout the degradation period is likened to a mechanical viscoelastic creep response and a sensor burn in period recommended.

In Chapter 3, results of accelerated lifetime testing at 10 kHz on two different LVT builds are presented. Two bonding methods are compared; in one, the fibre Bragg grating was bonded directly to the piezoelectric stack whilst in the other, alumina end blocks were bonded to either end of the stack and the FBG bonded to these and suspended above the stack.

Chapter 4 presents a protection circuit design review. Options regarding transient voltage suppression are investigated, and a refined design of the LVT protection circuitry is delivered, taking into account critical constraints. These include the LVT maximum voltage withstand, TVS (transient voltage suppression) diode characteristics, accuracy standards pertaining to phase and amplitude errors, and resistor current and power ratings. The error in voltage phase and magnitude measurements due to the inherent RC filter in the LVT device, formed by the capacitive piezoelectric stack and current limiting resistor combination, are discussed and an improved circuit design recommended.

Finally, Chapter 5 presents a summary of the key results in the preceding chapters and discusses future work.

Contents

Abstract **ii**

Acknowledgements **iv**

Overview **v**

1 Introduction **2**

1.1 Research objectives 2

1.2 Background 4

1.2.1 Fibre Bragg gratings (FBGs) 4

1.2.2 FBGs as sensors 7

1.2.3 FBGs as strain sensors 8

1.3 Review of existing current and voltage sensors 8

1.3.1 Existing current sensor designs 8

1.3.2 Existing voltage sensor designs 12

1.3.3 FBG-based current and voltage sensors 13

1.4 The inverse piezoelectric effect 15

1.5 LVT strain-voltage hysteresis compensation 16

1.6 Mechanisms of degradation of the piezoelectric constant in bulk PZT 18

1.6.1 Piezoelectric ageing, fatigue, creep and degradation 18

1.6.2 Fatigue mechanisms 22

1.6.3 Factors influencing fatigue rate . . . 23
1.6.4 Fatigue recovery . . . 24
1.6.5 Ageing mechanisms . . . 25
1.6.6 Volume mechanism . . . 26
1.6.7 Domain mechanism . . . 30
1.6.8 Grain boundary mechanism . . . 30
1.6.9 Factors influencing ageing rate . . . 31
1.6.10 Deageing . . . 35
1.7 Accuracy requirements for LVTs . . . 37

2 Investigation of effects due to piezoelectric stacks affecting LVT accuracy 41
2.1 Introduction . . . 41
2.2 Experimental set-up . . . 42
2.3 Optical sensitivity decay . . . 43
2.3.1 Modification of ageing rate . . . 46
2.3.2 Compensation of ageing process in software . . . 47
2.4 Ageing / deageing transition . . . 50
2.5 Test of deageing relation of Carl and Härdtl . . . 58
2.6 Frequency dependence of normalised OS decay B parameter . . . 59
2.7 Voltage step decrease magnitude dependence of normalised ageing decay B parameter . . . 62
2.8 Voltage step increase magnitude dependence of normalised deageing curve B parameter . . . 64
2.9 Effect of DC voltage offset on LVT response . . . 66
2.10 Characterisation of repeatability of normalised OS degradation curves . . . 68
2.11 Effect of ageing of PS at 0 V on LVT accuracy upon return to nominal voltage 71
2.12 Transient pulse duration impact on normalised degradation curve B parameter 74

2.13 Change in LVT sensitivity dependent on magnitude and phase of voltage transient . . . 75
2.14 Investigation into sensor interference in parallel circuit . . . 79
2.15 Temperature characterisation of piezoelectric response . . . 80
2.16 Summary and further work . . . 80

3 Accelerated fatigue testing of two unpackaged LVTs 83
3.1 Introduction . . . 83
3.1.1 Effect of bond length on reproducibility and strain transfer . . . 84
3.2 LVT builds . . . 85
3.3 Method . . . 87
3.4 Results . . . 88
3.5 Discussion . . . 93
3.6 Further work . . . 95
3.7 Conclusion . . . 97

4 Design review of prototype LVT protection circuit 98
4.1 Introduction . . . 98
4.2 Transient voltage suppression device selection . . . 98
4.2.1 Introduction and motivation . . . 98
4.3 Transient voltage suppression devices . . . 101
4.3.1 TVS diode critical parameters . . . 102
4.3.2 TRIAC critical parameters . . . 103
4.3.3 Critical steps involved in selecting a TVS diode . . . 104
4.3.4 Observations regarding TVS diode performance . . . 108
4.3.5 Determination of required TVS diode power rating . . . 109
4.3.6 Observations regarding TRIAC performance . . . 110
4.4 Current limiting resistor selection . . . 110
4.4.1 Resistor choice for a 5P20 class OCS . . . 110

4.4.2 Determination of power rating of CLR 115
4.5 Piezoelectric stack maximum voltage investigations 117
4.6 UNR 4-3425 burden resistor testing 118
4.6.1 Introduction 118
4.6.2 I-V characterisation 120
4.7 Alternative burden resistor testing 123
4.8 Summary 125

5 Conclusions and further work **127**

A LVT construction **142**
A.1 Unpackaged LVTs 142
A.2 Packaged LVTs 144

B TVS device I-V characterisation results **145**
B.1 Transil TVS diode I-V Plots for 10 ms DC V_{IN} 145
B.2 Transil TVS diode I-V Plots for 20 ms AC V_{IN} 147
B.3 Littelfuse TVS diode I-V characterisation 148
B.4 TRIAC I-V curves 150

List of Figures

1.1 Refractive index modulation pattern of FBG 4
1.2 FBG reflected Bragg peak. 5
1.3 Faraday effect based current sensor. 10
1.4 Packaged LVT assembly 13
1.5 Example piezoelectric hysteresis plots. 16
1.6 Hysteresis compensation procedure 17
1.7 Comparison of strain and polarisation changes when undergoing a reorientation of the PZT unit cell of 90 and 180 degrees respectively 26
1.8 The DW becomes trapped within a potential well with increasingly steep sides with time in the volume ageing mechanism 28
1.9 Variation in internal bias field with Fe dopant concentration 31
1.10 Arrhenius plots of deageing time for PZT 36

2.1 Experimental set-up for ageing investigation experiments 42
2.2 Example normalised OS decay and fit. 44
2.3 15 OS fits from an unpackaged LVT 45
2.4 Packaged LVT OS 51
2.5 Mean accuracy of Naïve Bayes classifier versus threshold voltage 56
2.6 Test of relation of Carl and Härdtl 58
2.7 Ageing curve fits upon dropping to 0.6±0.3 V_{RMS} 60

2.8 Ageing curve fits upon dropping to 0.6±0.3 V_{RMS} 61
2.9 Ageing curve fits upon dropping to 0.6±0.3 V_{RMS} 61
2.10 Ageing curve fits upon dropping to 0.6±0.3 V_{RMS} 62
2.11 Average normalised ageing curves for steps down from 20.4 to 10, 4, 2, 1 and 0.6±0.3 V_{RMS} for an unpackaged LVT 63
2.12 Normalised ageing curves for voltage step decreases 64
2.13 Normalised linear OS degradation fits 65
2.14 Normalised linear OS degradation fits 65
2.15 Normalised linear OS degradation fits 66
2.16 Effect of DC offset on LVT mean reflected Bragg wavelength for four LVTs. 67
2.17 Repeatability of B parameter 69
2.18 Repeatability of fit 69
2.19 Repeatability of B parameter 70
2.20 Repeatability of fit 70
2.21 OS data normalised by value of fit at time of final OS data-point for an unpackaged LVT. 72
2.22 Mean of first 2.5 minutes of OS data normalised by 2 hour value of fit for an unpackaged LVT. 72
2.23 Average normalised OS degradation curves for 10, 40, 80 and 15000 ms transients for a packaged LVT 74
2.24 Quantities defined 76
2.25 Linear relationship between percentage ΔOS and $\Delta\lambda_{Bav}$ 77

3.1 Schematic of fiber-tensioning set-up 85
3.2 Experimental set-up. 87
3.3 Normalised temperature compensated mean wavelength average over 20-25 minute values versus EY 50 Hz for both sensors. 88

3.4 Mean chamber temperature at interrogator position between 20 and 25 mins of 50 Hz sections and ratio of mean wavelength of sensor B to sensor A between 20 and 25 minutes versus EY 50Hz. 89
3.5 Directly-bonded stack, voltage normalised, ageing compensated OS mean over 20-25 minutes, normalised to first value 90
3.6 Directly-bonded stack, voltage normalised, ageing compensated OS mean over 20-25 minutes, normalised to first value 91
3.7 Ratio of sensor A OS to sensor B OS 20-25 min mean versus EY 50 Hz. . . 92
3.8 Normalised decay curves with B values in legend from Eqn 2.3 93

4.1 Present LVT protection circuit comprising burden resistor R_{B}, current limiting (protection) resistor R_{P}, a bidirectional TVS diode, and the PS (piezoelectric stack). 99
4.2 TVS (left) and TRIAC (right) test circuit diagrams. 100
4.3 Double exponential waveform from ST P6KE datasheet 102
4.4 I-V curve with parameter annotations for a bidirectional TVS diode from ST P6KE datasheet 103
4.5 I-V curve with symbol parameter annotations for a TRIAC from ON Semiconductor BTA30-600CW3G datasheet 104
4.6 Bode plot of first order RC low pass filter produced by the combination of the PS capacitance and the CLR 114
4.7 Peak Bragg wavelength versus time (top) and versus voltage (bottom) . . . 119
4.8 Experimental set-up for I-V characterisation of Vishay UNR-4325 2 Ω precision burden resistor. 121
4.9 Vishay UNR-4325 2 Ω precision burden resistor I-V curve with linear fit. . 122
4.10 Resistor case temperature versus time for duration of test. 123
4.11 2 Ω resistor foil damage due to heating 124

4.12 Top: Ohmite 850F1ROE 1Ω burden resistor I-V curve with linear fit. Bottom: Resistor case temperature versus time for duration of experiment . . . 125
4.13 Top: Arcol 1Ω burden resistor I-V curve with linear fit. Bottom: Resistor case temperature versus time for duration of experiment 126

B.1 Linear fit to I-V curve data under a 10 ms DC V_{IN} for TVS P6KE22CA . 146
B.2 Linear fits to I-V curve for the data obtained for TVS P6KE22CA 147
B.3 Temperature compensated I-V curves for five Littelfuse SMCJ24CA TVS diodes with linear fit to all those value pairs whose current exceeds 0.1 A . 149
B.4 I-V curve for TRIAC BTA30-800CW3G. 150

List of Tables

1.1 Accuracy requirements for protection class CTs 38
1.2 Harmonic accuracy requirements for protection class CTs. 39
1.3 Accuracy requirements for metering class CTs 39
1.4 Harmonic accuracy requirements for metering class CTs. 40

2.1 Table of ageing and deageing events 53

4.1 Comparison of minimum and maximum breakdown voltages 107

Glossary of abbreviations

AC Alternating Current.

AST Advanced Sensors Team.

BBL Broadband Light.

BBLS Broadband Light Source.

BS British Standard.

CLR Current Limiting Resistor.

CT Current Transformer.

CTE Coefficient of Thermal Expansion.

DC Direct Current.

DMM Digital Multimeter.

DW Domain Wall.

EY Equivalent Years.

FBG Fibre Bragg Grating.

FE Ferroelectric.

FFT Fast Fourier Transform.

GB Grain Boundary.

GE General Electric.

IEC International Electro-technical Commission.

LC Liquid Crystal.

LVT Low Voltage Transducer.

MOV Metal-Oxide Varistor.

NI National Instruments.

NPL National Physical Laboratory.

OS Optical Sensitivity.

PCB Printed Circuit Board.

PD Potential Divider.

PLZT Lead Lanthanum Zirconium Titanate.

PMN Sodium Potassium Bismuth Titanate.

PMN Lead Magnesium Niobate.

ppm Parts per Million.

PS Piezoelectric Stack.

PZT Lead Zirconium Titanate.

RC Resistive Capacitive.

RMS Root Mean Square.

SHM Structural Health Monitoring.

SMF Single Mode Fibre.

TCR Temperature Coefficient of Resistance.

TOC Thermo-optic Coefficient.

TRIAC Triode for Alternating Current.

TVS Transient Voltage Suppression.

UV Ultraviolet.

VT Voltage Transformer.

Chapter 1

Introduction

1.1 Research objectives

Due to the rise of intermittent renewable energy sources and consequent increased complexity of the challenge in balancing the grid, transmission and distribution network operators have heightened interest in increasing coverage of current and voltage monitoring systems. One such monitoring system involves a piezoelectric stack acting as a voltage-strain transducer, with the resulting strain shifting the reflected Bragg peak wavelength of an attached FBG. The advantages of such sensors over conventional systems are that they are small, lightweight, passive, robust to magnetic field and easily multiplexed.

The purpose of this work was to identify and investigate factors introducing voltage measurement uncertainty in low voltage transducers (LVTs) using FBGs and piezoelectric stacks (PSs), with a focus on factors originating from the sensor components themselves. Characterising and improving the accuracy of the sensors is a step towards providing a cheaper, easily multiplexed, proven alternative to conventional sensors.

The research objectives can be summarised as follows:

- Characterise and compensate for the LVT response to voltage transients such as would be experienced by the LVT under grid fault conditions. This work is an important step in ensuring that the LVTs meet the stringent accuracy requirements of BS EN 60044:2002 [1].
- Compare the fatigue lifetime of LVTs built with the FBG directly bonded to the PS, when compared to a configuration in which the fibre is suspended above the stack and bonded to end blocks either side of it. This information would inform a refined design of the LVT.
- Thoroughly review the prototype LVT protection circuit. This is a prerequisite for an upcoming demonstration of the LVT design, in which it will be compared with commercially available alternatives.

The primary source of novelty in this work is the investigation of piezoelectric ageing and deageing, in a configuration in which the displacement of the PS is unconstrained (open loop configuration) and is used for voltage measurement, rather than mechanical actuation. This differs from the conventional configuration in which the stack's displacement is constrained (closed loop operation) via mechanical loading, as in such applications stroke degradation may be compensated through driving voltage adjustments. This work was undertaken with the aim of developing compensation algorithms for piezoelectric effects affecting the accuracy of the LVTs, under grid fault conditions, and throughout their operational lifetime, and to understand the immediate behaviour of the LVTs upon installation.

1.2 Background

1.2.1 Fibre Bragg gratings (FBGs)

An FBG consists of a length of fibre with a periodic modulation in the refractive index of the fibre core of typical amplitude 10^{-4} [2]. Fig 1.1 from [3] illustrates this. The first permanent FBG (as opposed to self induced) was produced in 1989 through the exposure of Ge doped silica fibre cores to a ~5 eV UV interference pattern normal to the fibre axis [4].

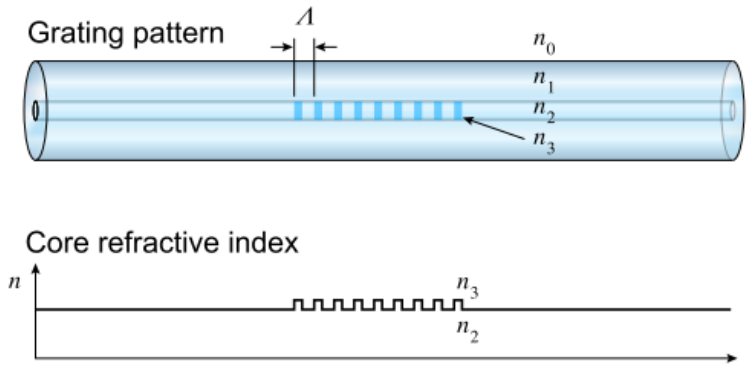

Figure 1.1: Refractive index modulation pattern of FBG. Fig from [3]

When broadband light is incident on an FBG, most of the light is transmitted but where the first order Bragg condition is met, light reflecting from the spatially separated refractive index boundaries constructively interferes, producing an approximately Gaussian peak in reflection about wavelength λ_B. Fig 1.2 shows example FBG reflection and transmission spectra obtained using an optical spectrum analyser, with broadband reference input.

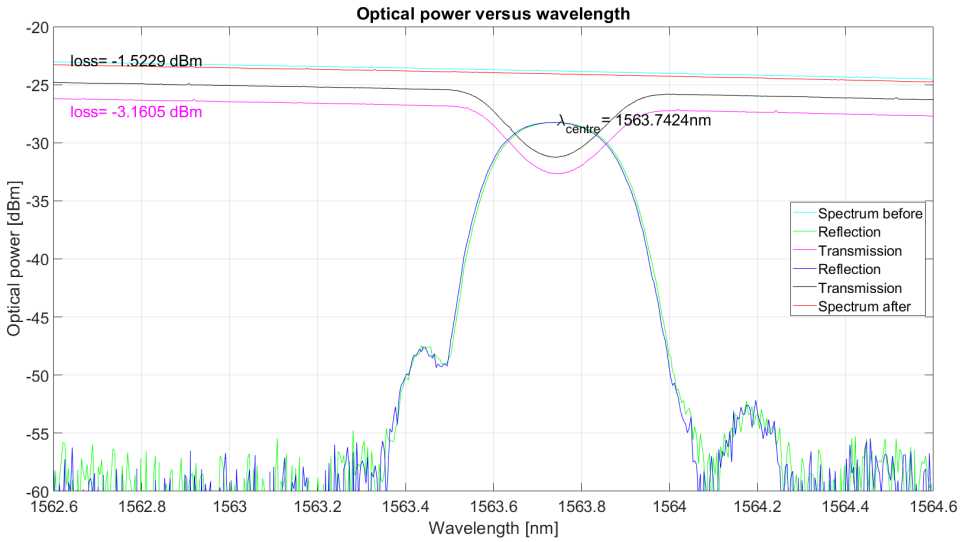

Figure 1.2: FBG reflection and transmission spectra obtained using an optical spectrum analyser, with broadband reference input.

In Canning's revised nomenclature of FBG categorisation, FBGs come in two distinguished types; type I, associated with refractive index change below the fibre damage threshold, and type II, associated with index change above the damage threshold. They are subdivided into type I, IH, In, IHp, IHs, Id, II and R gratings. Type I gratings that have undergone hydrogenation to enhance fibre photo-sensitivity are referred to as type IH gratings [5]. This process involves keeping the fibre at high pressure in hydrogen for several days to allow hydrogen absorption into core. Upon continued UV exposure, subsequent to type I grating formation, there is a reduction in the magnitude of the refractive index modulation in the FBG, and then a subsequent increase. Gratings which have been produced in this way are termed type In (formerly IIA) gratings [6]. If instead, UV exposure is continued beyond formation of a type IH grating, a type IHp grating is formed. The 'p' in IHp represents the observed positive change in λ_B with respect to the IH grating's λ_B, whilst the 'n' in In represents the observed negative change in λ_B with respect to the λ_B of

the type I grating from which it is derived [5]. Type IHs gratings are type IH gratings that have been pre-exposed to alter their predisposition towards particular photo-sensitivity altering processes and type Id gratings are type I gratings that have been exposed just below the damage threshold. Finally, type R gratings are 'regenerated'; they are produced by heating type I gratings until they deteriorate and new gratings form [5].

The reflected wavelength as a function of effective refractive index, n_{e} (1.47 for SMF-28 optical fibre [7]), and grating spacing Λ, is given by the first order Bragg condition (Eqn 1.1).

$$\lambda_B = 2n_e\Lambda \tag{1.1}$$

The strain dependence of the reflected wavelength is given by Eqn 1.2 [8].

$$\frac{\Delta\lambda_B}{\lambda_B} = \epsilon(1 - \frac{n^2}{2}[\rho_{12} - \nu(\rho_{11} - \rho_{12})]) \tag{1.2}$$

where ρ_{xx} are photoelastic constants, ϵ is the applied strain, and ν is the fibre Poisson's ratio. Eqn 1.2 can be simplified to Eqn 1.3 [8], where P_e is the effective photo-elastic constant of fused silica, commonly quoted as 0.22 in the literature.

$$\frac{\Delta\lambda_B}{\lambda_B} = \epsilon(1 - P_e) \tag{1.3}$$

The linear dependence of $\Delta\lambda_B$ on strain makes FBGs ideal for use as strain gauges, and as the strain information is spectrally encoded, such sensors can be easily multiplexed. The temperature dependence of the reflected wavelength is given by Eqn 1.4 [9].

$$\frac{\Delta\lambda_B}{\lambda_B} = 2(\frac{1}{n_e}\frac{dn_e}{dT} + \frac{1}{\Lambda}\frac{d\Lambda}{dT})\Delta T = (\alpha_n(T) + \alpha_\Lambda(T))\Delta T \tag{1.4}$$

where α_Λ and α_n are the optical fibre longitudinal coefficient of thermal expansion (CTE) with typical value $0.6 \times 10^{-6}{}^{\circ}\mathrm{C}^{-1}$ [10] and thermo-optical coefficient (TOC) with typical value $7 \times 10^{-6}{}^{\circ}\mathrm{C}^{-1}$ [11] respectively. Eqn 1.5 therefore gives the combined strain

and temperature dependence of λ_B.

$$\frac{\Delta\lambda_B}{\lambda_B} = (1 - P_e)\epsilon + (\alpha_\Lambda - \alpha_n)\Delta T \tag{1.5}$$

The temperature dependence of λ_B is approximated well by a linear fit in the 268-313 K range considered in the present application [12], though Flockhart et al demonstrated that a quadratic fit provides a more accurate description [13]. The temperature range studied by Flockhart et al extends beyond that required in the present application, and so the residuals to linear fits across this range should be reduced, compared to those of Flockhart et al. If we estimate the residuals to reach 10 pm for a given temperature, then temperature measurement at that temperature would be off by ~0.3 °C. Thus, it is generally desirable to assume a $\Delta\lambda_B$ with quadratic temperature dependence.

1.2.2 FBGs as sensors

Advantages of using FBGs as sensors are that they are physically small (bare industry standard SMF-28 fibre has a diameter of 125 µm), lightweight, immune to EM interference (whilst a conventional electrical strain gauge is not), easily multiplexed and interrogated over distances of kilometres, and can be designed to withstand temperatures >1000 °C [14].

In cases of transduction of multiple measurands of interest into strain, the sensing of multiple parameters is made possible. For example, in the case of simultaneous temperature and strain measurement, a nearby unstrained reference sensor can be used to measure temperature for compensation of the strained sensor. Alternatively, as is the case with simultaneous temperature and AC voltage measurement, the former can be monitored via the mean reflected Bragg wavelength, λ_{Bav}, and the latter by the amplitude of modulation of the reflected wavelength. This concept is detailed in section 1.3.3. FBGs have been used for a wide variety of sensing applications including vibration, humidity, pH, position, refractive index, pressure, magnetic field, and fluid flow velocity sensing.

1.2.3 FBGs as strain sensors

A conventional strain gauge consists of a length of current carrying wire wrapped around the component whose strain is to be measured. The resistance of the wire is then monitored as a function of time. The strain on the material can be determined as a function of resistance, given the resistivity and dimensions of the wire. The same principle applies to electrical foil strain gauges, in which the wire is a fraction of a nanometre thick and is printed over a plastic backing. Another type of electrical strain gauge is the semiconductor (piezoresistive) strain gauge, in which application of an electric field causes a change in inter-atomic spacing of a doped Si or Ge wafer. Electrical strain gauges are commercially available for strain measurements of up to 10% strain, and can perform up to 350 $^{\circ}C$ [15].

The primary application of FBGs as strain sensors is structural health monitoring (SHM) of, for example, steel pre-stressing tendons in concrete structures [16], helicopter blades, aircraft and wind turbine blades [17], bridges [18], ship hulls [19], rail infrastructure, concrete foundations [20], and deep oil wells [21, 22]. Several companies manufacture FBG based strain sensors, operating in the range $\pm$ 5 mϵ with typical sensitivity $\sim$1 pm$\mu\epsilon^{-1}$ [23, 24]. For context, commercial FBG interrogators are available with resolution $<$0.5 pm [25] and the best resolution reported in the academic literature is 0.05 pm [26].

1.3 Review of existing current and voltage sensors

This section gives a brief introduction to existing current and voltage sensor designs that have potential for use in power systems measurement. This measurement paradigm has specific requirements, among them; high accuracy and data acquisition rate, electrical insulation of the sensors from line faults, and immunity to strong magnetic fields.

1.3.1 Existing current sensor designs

The conventional way to measure current in power lines is to use a current transformer (CT). CTs however, require a lot of insulation from the line making them bulky and

expensive [27]. With the increasing uptake of renewable energy to the grid, there is a need to reduce the size and cost of current sensors to enable widespread implementation. This section highlights alternative current sensor designs that have been proposed.

Pilling et al suggested a optical fibre based current sensing scheme using twisted nematic liquid crystals (LCs) [27]. A CT feeds the LC voltage to optical intensity transducers, through which BBL (broadband light) is transmitted and detected. The scheme uses variation in light attenuation during the electric field induced transition from the chiral to the nematic phase of the LC, to obtain a measurement of the line current. The drawbacks of this system are that the response time of LCs is much slower than that of the PS used in the present application, and the measurement's dependency on the absolute intensity of transmitted light, which leaves the system vulnerable to error when light is attenuated by, for example, a kink in the optical fibre.

In magnostriction based sensors, an alternating current induces an alternating magnetic field via Ampère's law, which in turn strains a magnetostrictive alloy upon which an FBG is bonded. Reilly et al used SmCo permanent magnets to bias a magnetostrictive alloy so that a positive strain change coincides with an increase in current and a negative strain change coincides with a decrease in current [28]. Such sensors require compensation of temperature-dependent hysteresis, just as in sensors used in this project.

The Faraday effect is a magneto-optic effect in which circular birefringence produces a rotation in the polarisation of linearly polarised light, as it travels through a medium in a magnetic field co-linear with the propagation axis of the light. In sensors using this effect, polarisation maintaining fibre is wrapped around a current carrying wire. The rotation in polarisation due to the magnetic field surrounding the wire is then measured by one of the following methods.

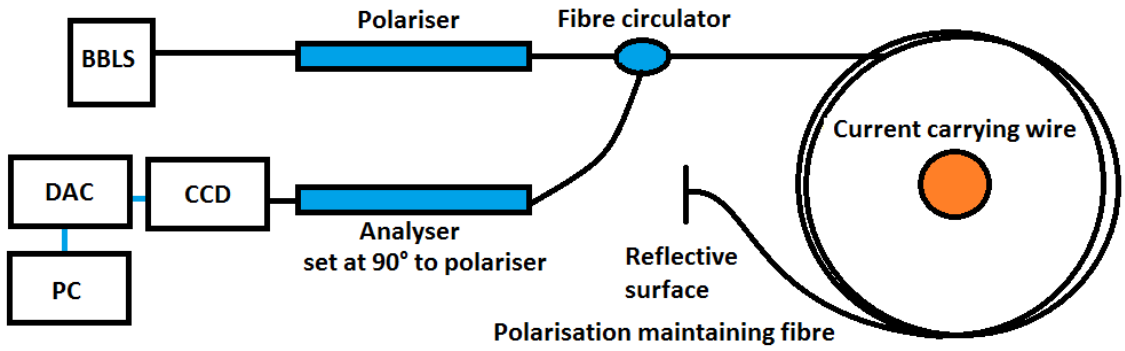

Figure 1.3: Faraday effect based current sensor; a BBL source emits light which is linearly polarised by a fibre polariser. The light circulates around the current carrying wire in polarising maintaining fibre and Faraday rotation occurs. The light is reflected, and further Faraday rotation occurs on the return trip. The voltage recorded at the PC is proportional to the current in the current carrying wire.

The first involves measuring the component of Faraday rotated light orthogonal to its original polarisation by means of a second polariser. Fig 1.3 depicts a basic implementation of such a sensor. The rotation in polarisation, θ, is then related to the magnetic field strength, B, by Eqn 1.6 [29], where v is the Verdet constant; a temperature-dependent [30] material parameter of typical value ~8×10^{-1} radT^{-1}m^{-1} at ~1300 nm in silica [8], and L is the optical path length traversed by the light in the magnetic field.

$$\theta = vBL \tag{1.6}$$

A second method uses an interferometer to measure the phase difference between the left- and right-handed circularly polarised modes. Eqn 1.7 relates the difference in refractive indices for left- and right-circularly polarised modes Δn to the magnetic field strength B [29].

$$\Delta n = \frac{vB\lambda}{\pi} \tag{1.7}$$

The current in the wire is then determined via the contour integral of the magnetic field around it via Ampère's law. These sensors, however, usually require polarisation maintaining optical fibre, relatively short interrogation distances, are sensitive to light intensity fluctuations[1], and cannot be easily multiplexed. Such sensors do, however, have advantages over FBG-based sensors introduced in section 1.3.3; including higher signal to noise ratio (in the interferometer based sensing scheme phase shift noise cancels), and higher AC current bandwidth, as the sensor is not limited by the resonant frequency of mechanical components, or electrical filtering effects due to piezoelectric capacitance, as in the FBG-based sensors, but rather by signal processing time. Furthermore, they have wider dynamic range, as this is not limited by the piezoelectric stack's nominal voltage range but rather theoretically by the saturation magnetisation of the diamagnetic fibre. Commercially available fibre sensors are typically based on the Faraday effect, with major industry players ABB [31], Toshiba [32], GE [33] and Arteche [34] having investigated this approach.

Ouyang et al introduced a current sensor based on the giant magneto-resistance (GMR) effect [35]. GMR is a property of some multilayer devices in which a 'giant' change in resistance is seen upon application of a magnetic field. The source of the magnetic field in this application is, again, the current carrying wire. The device requires a power supply and is therefore large, and also cannot be multiplexed.

Fluxgate magnetometers involve a magnetically permeable core with two coils around it in a transformer-like configuration. An alternating current is passed through the primary and another induced in the secondary winding. In the presence of an external magnetic field, the core is saturated at a lower current amplitude and from this discrepancy the external magnetic field present can be deduced. Yang et al [36] introduced a current sensor based on the fluxgate magnetometer. This sensor requires two magnetic cores, so is bulky and expensive.

[1]This can be compensated to a degree through normalisation of the AC optical signal by the DC optical signal

Finally, Tsai et al [37] introduced a current sensor based on the Hall effect. When a magnetic field is present perpendicular to the direction of an electric current in a conductor, the Lorentz force acting upon the conduction electrons induces a potential difference perpendicular and proportional to both magnetic field and current - this is called the Hall effect. In Tsai et al's measurement scheme, the sensor is mounted onto the surface of a power cable, such that the magnetic field from the cable is aligned perpendicular to a current flowing in the device. These sensors, again, do not offer the advantage of multiplexing.

1.3.2 Existing voltage sensor designs

Conventional voltage sensing on power transmission and distribution systems involves stepping voltage down using potential or capacitative voltage transformers, then monitoring voltage using a transducer. A capacitative voltage transformer incorporates a capacitative divider so that the transformer ratio may be reduced. This section introduces select alternative voltage sensor designs that have been proposed.

Potential dividers (PDs) are expected to be increasingly adopted as a substitute for voltage transformers (VTs) for voltage measurement applications due to their higher bandwidth, improved linearity and usability in DC applications. One disadvantage of PDs compared with VTs is the lack of galvanic isolation of voltage sensors from the line. In the event of a grid fault, over-voltage can damage the protective/measurement circuit if the PD is incorrectly grounded.

In the Pockels effect, birefringence induced in light traversing an electro-optic crystal is proportional to the electric field applied across the crystal. Pan et al used this effect to measure voltage [38]. Again, this type of sensor cannot be easily multiplexed and is sensitive to source fluctuations.

Alternative FBG-based schemes have been used, such as Fusiek et al's design [39], in which the voltage measurand is transduced into optical power. Such sensors are, however, sensitive to fibre attenuation. Lastly, voltage sensors based on electrostatic induction have been investigated by, for example Zhou et al [40], and are again, not easily multiplexed.

1.3.3 FBG-based current and voltage sensors

This section presents the working principle of the current and voltage sensors, which are the subject of this thesis. Suggested applications for the sensors include; protection and metering of power transmission and distribution networks, sub-sea and underground cable monitoring, for example, monitoring terminals of electrical submersible pump motors [41], and offshore vessel or aircraft electronics systems monitoring and protection [42].

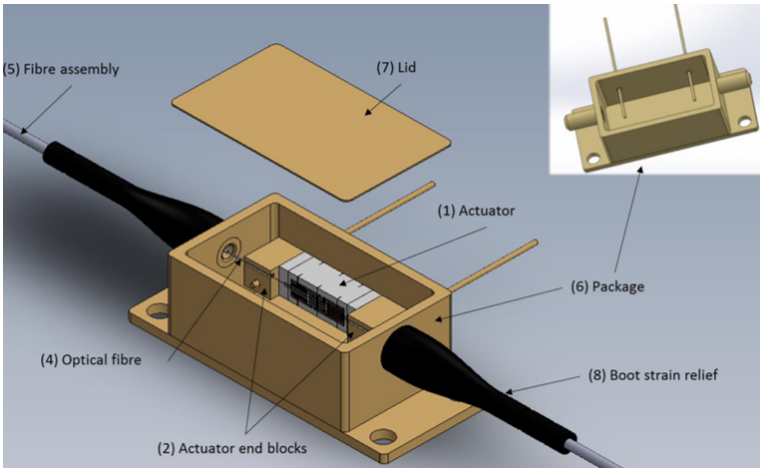

Figure 1.4: Packaged LVT assembly. Soldered wire leads from PS to package pins and package encapsulant not shown. Fig from [43]

During operation the input voltage is applied across the kovar pins seen entering the hermetically sealed package in Fig 1.4. The pins suspend the actuator within an encapsulant to provide isolation from vibrations on the package floor and provide the electrical connection to the PS. These pins are electrically connected to the PS via soldered wire leads (not shown), and the voltage strains the PZT (Lead Zirconium Titanate) PS via the inverse piezoelectric effect. A polyimide coated, pre-stressed SM fibre with inscribed 7 mm FBG is suspended parallel to the stack actuation axis, with FBG aligned with the stacks centre. The actuated stack indirectly transfers strain to the FBG via the route; end block - epoxy bond - polyimide coat - fibre cladding - fibre core[2]. Upon illuminating the fibre

[2]The PS and FBG based sensor described was patented in 2005 by Dr Paweł Niewczas and published

with a broadband light source, this strain causes the FBG's reflected Bragg peak to shift in wavelength in accordance with Eqn 1.5.

A commercial FBG interrogator is used to determine the wavelength of the maxima of λ_B via a centre-of-gravity peak detection algorithm. The peak's position is plotted against time and a fast Fourier transform (FFT) is used to extract the 50 Hz signal, whose peak-peak amplitude indicates the magnitude of the applied voltage. A large number of LVTs can be interrogated along a single fibre, however, with increasing number of sensors multiplexed, the severity of the consequences to the measurement system upon fibre damage too increases. Further limiting factors depend on the interrogation system used and will not be discussed here.

For voltage measurement, the LVT is connected directly across a VT secondary, or for current measurement, a CT secondary is connected to a precision burden resistor, with the LVT measuring the voltage across the resistor. Rogowski coils present a lighter, higher dynamic range alternative to conventional CTs. In accordance with Ampère's Law, alternating current from the transmission lines generates an alternating magnetic field between the Rogowski coil wire loops. By Faraday's law, this generates an electric field within the coil. The voltage generated in the coil is given by Eqn 1.8, where M is the coils mutual inductance.

$$V = -M\frac{dI}{dt} \tag{1.8}$$

This voltage is measured by the LVT, and can be integrated with respect to time to reconstruct the primary current [45].

by the World Intellectual Property Organisation under patent number WO 2005/029005 A1 [44]. The packaged sensor described was designed by Synaptec Ltd.

1.4 The inverse piezoelectric effect

Ferroelectric (FE) materials exhibit a permanent electric polarisation. In the most commonly used piezoelectric material; PZT, this arises as a result of the Ti^{4+} ion existing slightly off-centre in the unit cell. When an electric field is applied across these materials, this polarisation is increased in proportion to the dielectric susceptibility and a strain is induced on the material. This is called the inverse piezoelectric effect[3]. The piezoelectric constitutive equations for isothermal processes are given by equations 1.9 and 1.10 [46].

$$x_m = s_{mn}^{T,E}\Pi_n + d_{im}^{T,\Pi}E_i \tag{1.9}$$

$$D_i = d_{im}^{T,E}\Pi_m + \epsilon_{ij}^{T,\Pi}E_j \tag{1.10}$$

Here, superscripts are held constant, and x is strain, s elastic compliance, Π stress, d piezoelectric constant, E electric field, D charge density and ϵ the permittivity. The d_{33} component of the piezoelectric constant is typically of the order of several hundred pCN^{-1} in commercially available PZT [47]. When an electric field is applied, the piezoelectric material minimises its internal energy through splitting into domains of varying polarisation. Commercial piezoelectric actuators are poled. Poling is the term used to describe application of an electric field of sufficient strength to align the electric dipoles within the material and hence enhance its piezoelectric properties. The material is often first heated above the Curie temperature to release existing anisotropies, then cooled under a poling field to 'lock in' the anisotropy due to poling.

[3] In contrast to the direct piezoelectric effect; in which an applied strain generates an electric field.

1.5 LVT strain-voltage hysteresis compensation

Hysteresis is apparent in the piezoelectric strain-voltage response, due to resistance to domain wall motion caused by pinning sites in the piezoelectric material. Example $P - E$ and $\epsilon - E$ major hysteresis loops with initial poling curves are plotted in Fig 1.5. During LVT operation, only minor loops are observed as the coercive field is not exceeded.

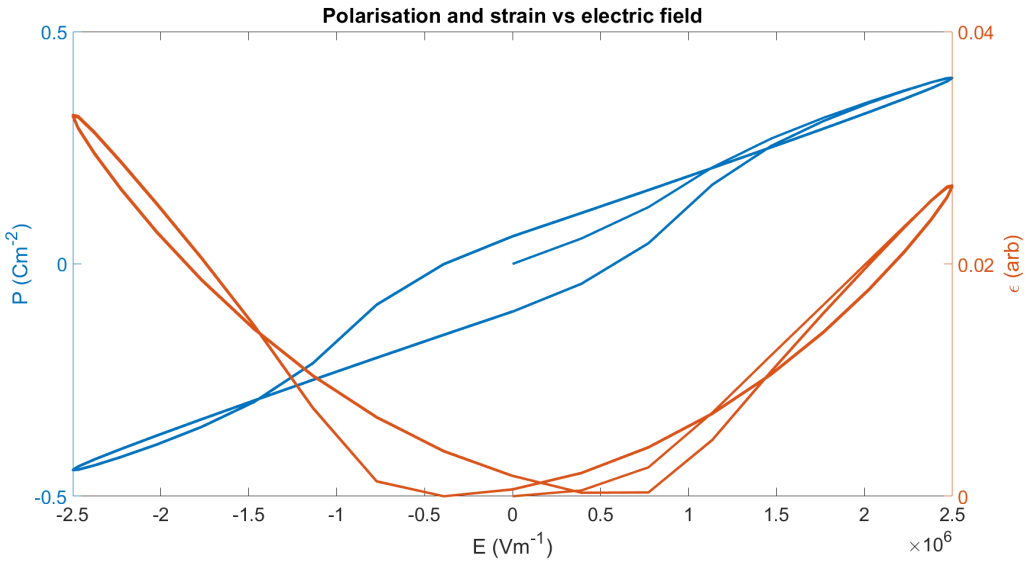

Figure 1.5: Example major loop piezoelectric hysteresis plots. This plot is an example only, based on the model of Muliana [48] and does not reflect the parameters of PIC 252.

This section describes the compensation procedure for temperature-dependent piezoelectric hysteresis in the LVTs, based on work of Fusiek et al [49].

Prior to device installation

- λ_{Bav} as a function of temperature T is characterised and stored.
- The peak-peak wavelength of the LVT as a function of temperature, $\lambda_{\mathrm{pkpk}}(T)$, is recorded at nominal voltage, and stored.

- One polynomial function of λ_{B}, applied voltage V and maximum applied voltage is recorded at reference temperature T_0 and stored.

During operation

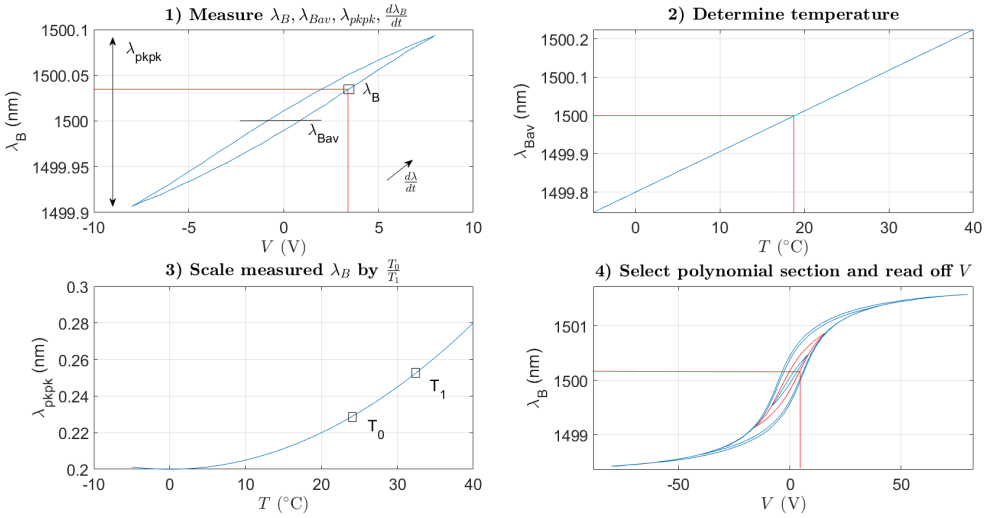

Figure 1.6: Hysteresis compensation procedure; functions are examples only and may differ from functions observed in practice. Hysteresis loops generated using Szewczyk's implementation [50] of the Jiles-Atherton model [51]

Figure 1.6 provides a visual guide to the process outlined below.

- During operation λ_{B} and λ_{Bav} are measured and the latter is used to determine the device temperature.
- λ_{B} is multiplied by ratio $\frac{\lambda_{pkpk}(T_0)}{\lambda_{pkpk}(T_1)}$ found from stored function $\lambda_{\mathrm{pkpk}}(T)$ and the most recently measured value of λ_{pkpk} is stored.
- The rate of change of λ_{B} is monitored in real time to determine which section of the stored polynomial should be used to determine V.

- Finally the most recent scaled and stored value of λ_{pkpk} is used to select the appropriate section of the polynomial to use, and the V corresponding to the present value of λ_{B} is read off.

1.6 Mechanisms of degradation of the piezoelectric constant in bulk PZT

This section first clarifies the semantic difference between piezoelectric ageing, fatigue, creep and degradation; phenomena that will be investigated in Chapters 2 and 3. The terminology used in this thesis is then clarified before taking a closer look at the literature on mechanisms involved in each phenomenon. The reported dependencies of ageing and fatigue on relevant physical parameters are highlighted and comment is passed where appropriate on the applicability of the results to the present application. The section ends with an introduction to the concept of deageing, which again will be investigated in Chapter 2.

1.6.1 Piezoelectric ageing, fatigue, creep and degradation

This section clarifies the semantic difference between piezoelectric ageing, fatigue, creep and degradation.

Ageing

Ageing is described by Genenko et al [52] as 'gradual changes of a materials properties with time under external equilibrium changes' and as 'degradation with time in the absence of an external electrical or mechanical load'. This definition is extended by Lupascu and Genenko in [53] to mean the contraction along the polarisation axis and expansion along the electric field axis of the piezoelectric hysteresis loops with time after cooling from the para-electric phase. Kholkin et al [54], extend this to include changes after 'electrical pre-treatment to reach the deaged initial state' and this is in agreement with Damjanovic's [46] 'change in

material properties with time, provoked by temperature change or application of strong electric fields'. Morozov and Damjanovic [55] then increased the terms scope to include changes of material properties with time upon changing thermal, electrical or mechanical environment. Schulze and Ogino [56] limit the definition to changes under strictly 'zero external stress and isothermal conditions' that can be reversed through thermal cycling above the Curie temperature. To complicate matters, among others, Zhang and Ren [57] use the term ageing to describe changes under weak AC electric field, and Kholkin et al too [58], use the term to describe degradation in electrical properties in the presence of an AC field. The trigger in this experiment is the removal of a poling field. Genenko's aforementioned later definition directly contradicts this useage of the term.

For the purpose of this thesis then, the term ageing is defined as gradual changes in material properties such as, but not limited to, remnant polarisation, piezoelectric, dielectric and electro-strictive tensor, coercive field and domain configuration. The term is limited to applications characterised by the absence of electrical or mechanical loading, in which the process is triggered by an external factor such as change in temperature, electric field, or stress. It is assumed in this thesis, that the absence of external mechanical or electrical load is not a requirement for the degradation to take place, but rather is used to separate the degradation effect from that of fatigue, defined below. Under this definition, the addition of a cycling electric field such as is used by Zhang and Ren, and Kholkin et al, is considered ageing in the presence of fatigue, to acknowledge that the ageing process just defined is thought to be the primary cause of the decay observed, but the conditions for fatigue are also present.

Creep

The term creep is used to describe behaviour analogous to mechanical creep, in which the PS polarisation and displacement with time exhibit a response similar to that seen in viscoelastic materials. This is thought to be due to thermally activated pinning and unpinning of domain walls [59]. According to PI Ceramic [47], creep is the term used to

describe the 'change in displacement over time with an unchanged drive voltage', with creep rate decreasing logarithmically with time according to Eqn 1.11 with L_0, the magnitude of the PS displacement 0.1 s after the the voltage change that caused it and γ a constant of order 10^{-2} [60]. L_0 and γ show hysteresis when plotted against applied voltage [60].

$$L(t) = L_0(1 + \gamma log_{10}(10t)) \tag{1.11}$$

Jung et al [60] are in agreement with this definition, noting that the above equation 'excludes dynamic response'. Here they refer to a dynamic transient initial response to an applied voltage of the order of milliseconds in duration. Zhou and Kamlah [61] too are in agreement with this definition, defining creep as 'a drift from the desired position when positioning is required over a long period of time'. This is attributed to microscopic motion of domain walls. Confusingly, Kholkin et al include a creep study under the heading of ageing [54].

Degradation

Sherrit et al [62] refer to the change in piezo stroke due to electric field cycling as degradation without specific mention of mechanisms, whilst Kholkin et al [54] use degradation as a general term describing changes through both ageing and fatigue. Sherrit et al [62] also list creep as separate to degradation of material properties. The usage of the term in the fatigue definition of Jiang et al [63] further strengthens the case for the usage of degradation as a general term describing the change in material properties with time and this is the definition that is used from here in, in this thesis. In contrast, Schulze and Ogino [56] specifically denote degradation as a 'catastrophic change or failure that destroys the function of the device'.

Fatigue

Genenko et al [52] vaguely define fatigue as the 'gradual change of material properties during service', whilst Damjanovic [46] provides a more descriptive definition; 'loss of switchable remnant polarisation in FEs as a function of number of bipolar switching cycles'. This is in agreement with usage of the word by Kholkin et al [54], and the definition of Jiang et al; [63] 'degradation of electrical properties under action of an AC field applied for a long time'. Lupascu and Genenko [53] note that fatigue was referred to as 'dynamic ageing' in the early literature, but this description should be avoided to prevent confusion. The term fatigue is not limited to bipolar operation, with both Luo et al [64], and Genenko et al [52] referring to unipolar fatigue. Fatigue is characterised by degradation of material properties due to the the presence of applied external cycling electrical or mechanical stress *during* degradation, and does not require an external trigger such as temperature change or application of electric field. Sherrit et al [62] observed a <4% decrease in PS stroke over 10^{11} cycles at 2 kHz during fatigue (equivalent to 63 years at 50 Hz).

Summary of definitions used in this thesis

- *Ageing*: Change in material properties with time, in the absence of electrical or mechanical loading, from an initial de-aged state, triggered by an external factor such as application of electric field, heat, or stress. The addition of a cycling electric field is considered ageing in the presence of fatigue.
- *Creep*: Drift in piezoelectric displacement with time upon subjection to an unchanged drive voltage, excluding the initial dynamic response.
- *Degradation*: General term describing the change in material properties with time.
- *Fatigue*: Change in material properties with time, under the action of an applied external cycling electrical or mechanical stress.

1.6.2 Fatigue mechanisms

There are four fatigue mechanisms postulated in the literature; micro-cracking, accumulation of a non-FE surface layer at the FE - electrode interface, domain wall (DW) pinning by charge carriers and localised phase 'freezing'. Genenko explains that the ageing mechanisms described in section 1.6.5 may also contribute to fatigue, but mechanisms of fatigue extend beyond these.

Both Wang et al, [65] and Jiang et al [63] attribute fatigue in PZT and PLZT, (lead lanthanum zirconium titanate), respectively, to intergranular micro-cracking of the ceramic due to internal stress caused by a cycled electric field, particularly at defect locations. The formation of cracks reduces the dielectric permittivity of the sample, reducing sensitivity to applied electric field. Genenko et al [52] state that this mechanism is not relevant for ageing.

Jiang et al [63] attributed fatigue in PMN (Lead Magnesium Niobate) ceramics[4] to charge carriers accumulating in voids and pinning domains. The idea is that the cycling field assists the redistribution of charges. which makes it increasingly difficult to reorientate the polarisation of domains, upon reaching a state in which the free energy of the system is minimised.

The polarisation of a given domain is given as the sum of the external applied electric field, and the depolarising field[5] together multiplied by the dielectric permittivity of the material. Shur et al explain that, upon a polarisation switching event, the depolarising field is instantly largely compensated by charge redistribution at the electrodes. The remaining depolarising field is slowly compensated by the accumulating internal bias field, arising as a direct result of domain stabilisation by diffusion of charge within the bulk material. In regions of strong internal bias field, domains become 'frozen' and polarisation switching is

[4]PMN used in this study is classified as a relaxor FE rather than a piezoelectric material. The electrostrictive effect is similar to the piezoelectric effect, with the strain induced by an electric field quadratically, rather than linearly dependent on the sample polarisation. Relaxor FEs exhibit high electrostrictive constants. The term ceramic is used in this thesis, in the usual sense of the word, but is additionally intended to identify a bulk, as opposed to a thin film sample.

[5]Analogous with the demagnetising H field in ferromagnets.

incomplete [66].

Fatigue has further been attributed to accumulation of a non-FE surface layer on electrodes at the FE-electrode interface, which acts to increasingly screen the applied electric field with time [67]. Finally, during electric field cycling, the crystallographic phase composition of PZT changes with applied electric field [68]. Fatigue may be caused by 'freezing' of the phase of a fraction of the material [52].

1.6.3 Factors influencing fatigue rate

A variety of factors have been observed to affect the fatigue rate of FE ceramics in the literature. Wang et al observed a lower fatigue rate with increasing temperature. At higher temperatures, the electric field and hence strain required to depole the sample is reduced, and thus they propose that the defects undergo less stress by domains in the process of reorientation [65]. They attribute micro-cracking as the dominant fatigue process in their experiment, which they claim requires a threshold stress of 50 MPa. In their experiment they achieve a stress of 55 MPa under an electric field of magnitude 2 MVm^{-1} and a temperature of 23 °C. Given that the electric field in the present application, at nominal voltage, is 2×10^4 times less than field, micro-cracking should be an irrelevant fatigue mechanism for the LVTs. Thus, the temperature dependence of fatigue reported by Wang et al, may not be the same as that in the LVTs. Instead, the fatigue process may be dominated by the effects relevant to ageing described later in this chapter.

The fatigue rate is reported to be frequency dependent. Pojprapai et al reported that in the 10 - 100 Hz regime, increasing frequency leads to a reduction in fatigue degradation and inhibits crack propagation [69]. Furthermore, in PLZT thin films, Zhang et al observed a considerable decrease in fatigue degradation at 100 and 500 kHz applied field [70]. Increasing frequency leads to self-heating of the PS, which should act to reduce the fatigue experienced. In an accelerated life test, the stack temperature should, therefore, drop during lower frequency periods during which the optical waveform is monitored. Equation 1.12 gives the relationship between dissipated power through self-heating P, and frequency f,

where $\tan(\delta)$ is the electric loss tangent, C is the stack capacitance, and V_{PP} is the applied peak-peak voltage [47].

$$P = \frac{\pi}{4} \cdot tan(\delta) \cdot f \cdot C \cdot V_{PP}^2 \tag{1.12}$$

Wang et al noted that increasing field strengths accelerate the fatigue rate of PZT at 10 Hz in the region ± 0.85 to ± 3 MVm^{-1} [65], with fatigue much worse in bipolar operation. This is in agreement with the results of Luo et al in $0.94Bi_{1/2}Na_{1/2}TiO_3 - 0.06BaTiO_3$ [64]. Both Wang et al and Luo et al used electric field strengths orders of magnitude above those seen in the present application and that they in fact cycled beyond the coercive fields of the samples. Therefore, again, this dependency may not be the same as that seen in the LVTs.

Lee et al studied fatigue in thin film PZT in Pt/PZT/YBCO and YBCO/PZT/YBCO and found a significant reduction in fatigue rate in the latter samples. The dependence on electrode material was seen to be much greater than the dependence on crystal quality. They also observed slower fatigue degradation in polycrystalline PZT thin films when compared with epitaxial and high crystal quality films, indicating a dependence on grain size [71]. Lastly, Jiang et al [63] suggest that materials with fewer defects fatigue at a slower rate, as there are fewer defects to pin domains.

1.6.4 Fatigue recovery

Warren et al achieved ~90% polarisation fatigue recovery in PZT thin films through illumination with UV light of wavelength corresponding to the energy of the electronic bandgap in combination with a polarisation saturating electric bias field. They propose that through illumination with UV light, valence electrons are energised to the conduction band and electrons and/or holes migrate towards charged pinned domains, neutralising trapped charge and de-pinning the DWs [72]. They suggest that the primary mechanism involved in fatigue in their experiment is DW pinning by trapped electronic charge and

that the remaining ~10% of fatigue may be due to DW pinning by lattice defects [72].

Wang et al [65] achieved less than 20% recovery of lost piezoelectric constant upon repoling at 'high electric field' and 350 °C for two hours. This supports their theory that micro-cracking was the dominant fatigue mechanism in their experiment. Sherrit et al [62] achieved ~50% recovery of lost piezo stroke in the same material as is used in the present application (PI Ceramic's PIC 252), after fatiguing samples using a sinusoidal unipolar electric field cycling between 0 and 20 V, then repoling at 100 VDC for a period of minutes. This corresponds to an electric field two to three times greater than that seen by the stacks in the present application under a grid fault and thus it is unclear whether the electric field experienced by the stack in the event of a fault will be sufficient in magnitude to recover lost stroke. It is additionally unclear whether the faults would be of sufficient duration for repoling. Grid fault conditions are further discussed Chapter 4.

1.6.5 Ageing mechanisms

During ageing, piezoelectric materials display a deterioration in dielectric ϵ and piezoelectric constant d, coupling factor, and loss factor. They further display an increasing mechanical quality factor, and resonance frequency [56, 73]. The mechanisms of piezoelectric ageing are still a subject of debate, but there are three major domain pinning mechanisms thought to be at play during the piezoelectric ageing process; the so-called volume, domain and grain boundary (GB) mechanisms [52].

Each mechanism is associated with lattice defects such as impurities, dopants and lattice vacancies[6] increasingly impeding the motion of non-180° DWs (that is DWs between adjacent domains having a non-180° difference in polarisation) with time. Different mechanisms are proposed to be dominant for bulk vs thin film samples.

[6] Missing ions in the unit cell

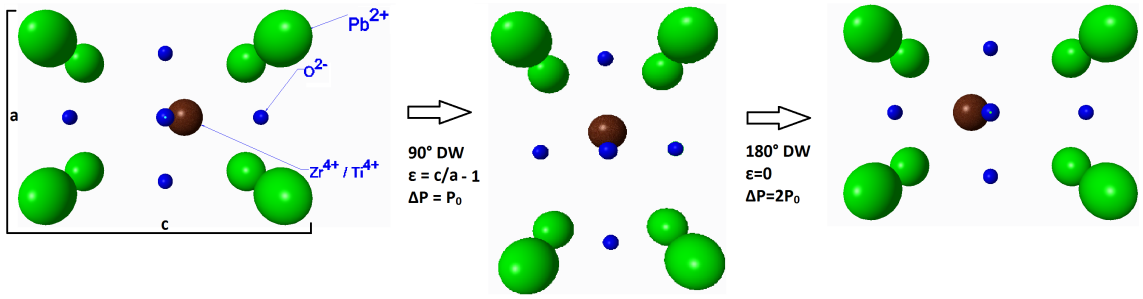

Figure 1.7: Comparison of strain and polarisation changes when undergoing a reorientation of the PZT unit cell of 180 and 90 degrees respectively. c and a represent tetragonal unit cell inter-atomic distances.

Non 180° DW motion is considered the dominant factor governing the piezoelectric constant. To understand why, consider the PZT unit cell shown in 1.7. The diagram shows that upon a 180° rotation, the polarisation - governed by the position of the Zr^{4+} / Ti^{4+} ion - undergoes a greater change than compared with a 90° rotation, whilst under a 90° rotation, the length undergoes a much greater change than that compared with the 180° rotation [74].

1.6.6 Volume mechanism

This mechanism concerns the stabilisation of whole domains. In acceptor doped[7] ceramic ageing, a shift in the piezoelectric hysteresis loop along the E axis (hardening) occurs over time. This increase in coercive field is attributed to the internal bias field, which accumulates in PZT due to a slow relaxation of defect dipoles consisting of an acceptor ion at the Ti^{4+} site and an oxygen vacancy in the same unit cell [75]. In poled PZT ceramics, this internal bias field can be observed as a shift of the $P - E$ hysteresis loop along the E axis.

After poling field removal, elastic and electric defects within domains are initially ran-

[7]In donor doping, an ion is replaced with a dopant of higher valence whilst in acceptor doping, an ion is replaced with a dopant of lower valence.

domly oriented [46]. With time, to minimise the free energy, these defects are re-orientated towards the direction of the spontaneous polarisation or spontaneous strain [73]. After this energy minimisation takes place an energy barrier associated with the internal bias field caused by reorientation of aligned defects must be overcome to alter the spontaneous polarization or strain direction [46].

Robels and Arlt [75] introduced a physical theory of ageing via the volume mechanism for FEs in an alternating elastic or electric field. They claim that the activation energy for diffusion of an oxygen vacancy at an acceptor doped site in PZT is 1.2 eV. Thermal energy at room temperature is around 0.03 eV therefore these sites need time to settle to equilibrium. For free energy minimisation, defect dipoles must be oriented in the same direction as the polarisation of the domain which they inhabit. Therefore, when a 90° DW is displaced, there is a free energy cost associated with altering the polarisation in a region where some defects are already in their minimum energy configurations. Fig 1.8 shows the DW becoming trapped in a potential well with increasingly steep walls with ageing [75].

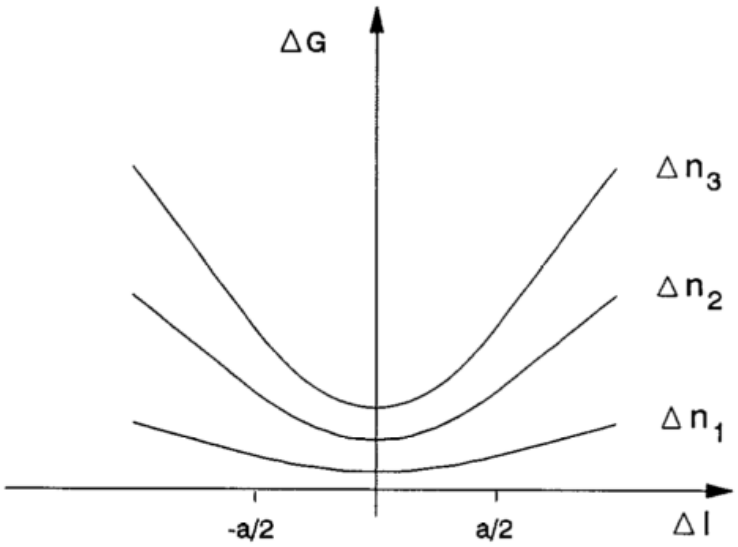

Figure 1.8: The DW becomes trapped within a potential well with increasingly steep sides with time in the volume ageing mechanism. DW displacement is given on the x axis and free energy on the y axis. Δn_i represents the number of defects oriented in the minimum energy configuration per unit volume, with increasing i corresponding to longer ageing times. In the model of Robels and Arlt, the DW width (i.e. the finite distance over which the local dipoles twist at the domain boundary) is denoted a. Fig from [75]

The contribution to d_{33} due to 90° DW motion for a piezoelectric ceramic with z axis parallel to the net polarisation is given by Eqn 1.13 [75] .

$$d_{33(90^\circ DW)} = \frac{P_0 S_0 f_{d33}}{a c_{55} S_0^2 + b \frac{P_0^2}{\epsilon_0 \epsilon_{11}}} \tag{1.13}$$

P_0: Polarisation of domain

S_0: Spontaneous strain of domain

f_{d33}: Function of remnant polarisation

ϵ_0: Permittivity of free space

ϵ_{11}: Dielectric permittivity

c_{55}: Elastic constant

a, b: constants $0.3 < x < 2.0$

When clamping by defects is considered, the contribution to d_{33} due to 90° DW motion is reduced, and is instead given by Eqn 1.14 [75].

$$d_{33(90^\circ DWCL)} = \frac{P_0 S_0 f_{d33} w}{2d\Delta n(t)} \frac{f_e}{\Delta W_e} = \frac{P_0 S_0 f_{d33} a}{2d} \frac{f_e}{P_0 E_i} \tag{1.14}$$

w: DW width

d: Domain width

ΔW_e: Increase in electric field energy of domain per unit area due to DW displacement

f_e: Ratio of macroscopic internal bias field to domain internal bias field

E_i: Macroscopic internal bias field due to applied electric field

This assumes a single tetragonal lattice phase and a linear change in DW clamping pressure across the width of the DW. The reduction in d_{33} observed due to 90° DW clamping can be attributed to increasing either internal electric bias or stress fields, however the stress field dependence is irrelevant in the present application and so is omitted for simplicity. The dependence on domain width must introduce a statistical nature to the ageing rate, as domain nucleation is a stochastic process. New oxygen vacancies may be created over time, altering Eqn 1.14 through the $\Delta n(t)$ term.

The next two major ageing mechanisms considered are based on DW pinning. Zhang and Ren examined the ageing of a single domain $BaTiO_3$ crystal and concluded that the volume mechanism is dominant in this system due to the existence of significant ageing in the absence of DWs. [57]

1.6.7 Domain mechanism

In this mechanism, after removal of a field comparable to the poling field, DWs initially have some freedom to relax. Subsequently, both charged and neutral defects diffuse towards DWs due to their electric and elastic fields. This pins the DWs in place upon contact, owing to the energy barrier associated with increasing their surface area.

Lambeck and Jonker [73], however, dispute the significance of this effect, as it has been shown that for monocrystalline samples, the electric field strength required to nucleate domains is comparable to that required for DW motion and thus pinned DWs could remain stationary whilst newly formed domains without pinned walls envelope them. Owing to a lack of defects, domain stabilisation ageing is not seen in very pure materials [73].

1.6.8 Grain boundary mechanism

The GB mechanism concerns the stabilisation of whole grains[8]. In this mechanism, the electric fields - originating from polarisation discontinuities at GBs due to the presence of another phase of PZT [76] - attract space charges in the form of charged dopant particles and vacancies [73]. These charges stabilize the DW configuration after structural equilibrium is reached. [46] A positively charged oxygen vacancy can occur when one metal ion is replaced by two dopant ions. Recall that, in donor doping, an ion is replaced with a dopant of higher valence whilst in acceptor doping, an ion is replaced with a dopant of lower valence. In this mechanism, oxygen vacancies and negatively charged acceptor ions, couple and diffuse to the GB forming a dipole which resists non-180° DW motion.

[8]Crystalline regions with varying orientation of the crystallographic axes with respect to one another

1.6.9 Factors influencing ageing rate

This section reviews factors influencing the rate of piezoelectric ageing, in preparation for Chapter 2, in which compensation or removal of the effect is considered.

Dopant concentration

Soft (donor doped) piezoelectric materials are those which are relatively easy to polarise, whilst hard materials are those which are relatively difficult to polarise. Donor doped FEs exhibit slower ageing than acceptor doped (hard) FEs [52]. For example Berlincourt and Krueger [77] noted that the addition of 1% by weight Nb_2O_5 improves ageing of PZT. Fig 1.9 indicates that the ageing rate is dependent on dopant concentration.

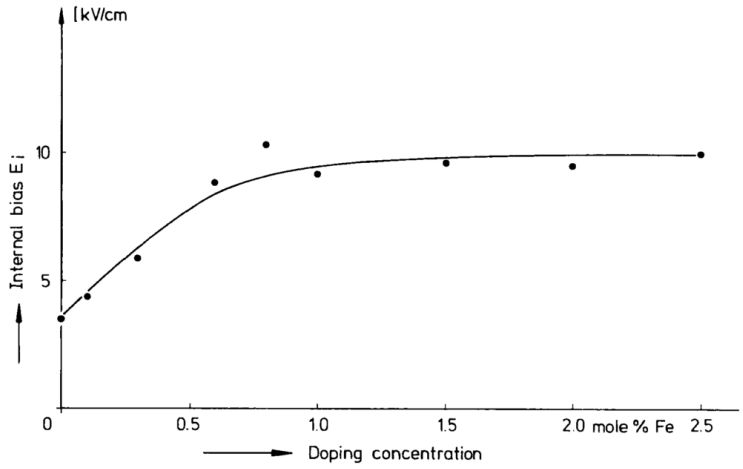

Figure 1.9: Variation in internal bias field with Fe dopant concentration for aged, poled, bulk PZT. A larger internal bias field indicates a smaller change in d_{33} due to ageing according to Eqn 1.14. Fig from [76]

There are multiple hypotheses as to why donor doping increases DW mobility. Slower ageing in donor doped FEs has been attributed to the introduction of lattice vacancies facilitating DW motion. For example, each replacement of Ti^{4+} with two La^{3+} ions will result in a Pb^{2+} vacancy. Possible donor dopants include Nb^{5+}, Ta^{5+}, W^{6+}, Th^{4+}, Bi^{3+} and Sb^{5+}. It has also been suggested that softening reduces charge accumulation at DWs

and that donor dopants neutralise acceptor cation impurities. [55]

It is thought that upon a change in externally applied electric field, the increased mobility of the DWs enables rapid internal strain relief. Thus what is observed as a slowed ageing process is really an instantaneous rapid ageing process upon change in external electric field [78]. Although it cannot be considered as acceptor nor donor dopant as it exhibits varying valences within the lattice, Cr doping has also been shown to slow ageing. [78]

Hard materials are associated with acceptor dopants and pronounced ageing [55]. Although the material used in the present application; PIC252, is classified as a soft material on the PI Ceramic website [47], it may be acceptor doped. This dopant concentration could be modified to adjust the ageing rate.

Zr and Ti concentration

The PZT unit cell exhibits greatest piezoelectric properties on the morphotropic phase boundary; the compositional boundary between tetragonal and rhombohedral phases. This is found at approximately $x = 0.47$ to 0.48 [76, 79] in the formula $Pb[Zr_xTi_{1-x}]O_3$. Jonker observed that the ageing rate is increased with increased tetragonality of the perovskite unit cell in unpoled BZT (Barium Zirconium Titanate) through constriction of the hysteresis loops [80]. The phase transition from orthorhombic to tetragonal was, however, achieved through an increase in temperature which would also increase the ageing rate as detailed below, so this relationship is inconclusive.

Grain size and purity

The ageing rate, in the presence of fatigue[9], of the dielectric constant has been shown to be slower and less sensitive to temperature and frequency with finer grain size in another FE; ceramic $BaTiO_3$ [81]. Grain size is determined by the cooling rate after sintering[10].

[9] Wu et al applied a <10 Vcm^{-1} field

[10] Application of heat and pressure during the manufacturing process to fuse together thin layers of PZT

From Eqn 1.11 it appears that through increasing the purity of the PZT, the change in d_{33} could also be minimised. This would also minimise the effects of other mechanisms due to lack of defects for diffusion.

AC parameters

Kholkin et al observed that the ageing rate of d_{33} is accelerated at high AC amplitude in PZT thin films. This was attributed to film depolarisation. They compared ageing of d_{33} at 5 and 90 Hz AC frequencies and observed no difference in ageing rate [58]. This is in contrast with the results of Zhang et al, who observed increasing ageing rate with decreasing AC frequency in piezoelectric NKBT (sodium potassium bismuth titanate) thick films in the region 1 - 100 kHz - vastly different to the fundamental frequencies which will be seen in the field by the LVTs.

The difference in frequency dependency may be due to varying relative strength of ageing mechanisms between the two experiments - Kholkin et al attribute ageing in PZT thin films to film depolarisation whilst Zhang et al point towards non-180° DW pinning by defects in NKBT. Kholkin et al also propose that the dominant ageing mechanism differs between bulk and thin film PZT. Care should therefore be taken when making ageing rate dependency comparisons between different piezoelectric materials and thicknesses.

Temperature

Diffusion exhibits an Arrhenius temperature dependence, given by equation 1.15, so ageing through the diffusion and GB mechanisms should also be slowed through cooling.

$$D = D_0 exp(-U/k_B T) \tag{1.15}$$

Here D_0 is a constant, U is the average energy required for defect diffusion, k_B is the Boltzmann constant and T is the temperature in Kelvin. Furthermore, the re-orientation of defects in the volume mechanism should also exhibit an Arrhenius temperature dependence.

The temperature dependence of ageing has also been attributed to the increased production of oxygen vacancies due to Ti^{4+} ion reactions with oxygen at the cathodes [82]. The hypothesis of reducing ageing rate through cooling has been confirmed by Adler and Cherry [83] in $BaTiO_3$ - they observed accelerated ageing at a temperature of 65° C upon poling field removal. This contrasts with the fatigue degradation rate which is observed to increase with decreasing temperature.

It can be seen from Eqn 1.14 that increased temperature may also decrease the magnitude of the step in d_{33} due to ageing through decreasing the spontaneous polarisation. Robels and Arlt, however, note that ΔW_e increases with decreasing temperature, again reducing the step change in d_{33} during ageing [75]. To summarise then, with increasing temperature, the ageing rate is accelerated due to Arrhenius dependencies and its impact on the step change in d_{33} must be governed by the relative temperature dependency of ΔW_e compared to spontaneous polarisation.

DC bias transients

A DC bias should increase the degradation rate of the piezoelectric constant through increase in temperature. Whether the magnitude of the ageing step increases or decreases with increasing temperature depends on the relative strength of the magnitude reducing term, $P_0(T)$, compared with the magnitude increasing term $P(E)$.

Poling field direction and duration of application

Kholkin et al reported that in cases where PZT thin films exhibited a strong spontaneous polarisation due to charge distribution inhomogeneity prior to poling, the ageing rate increases when poling was opposite to the initial spontaneous polarisation [54]. They also reported that the ageing rate decreases with increasing time under poling field prior to ageing. This was attributed to longer poling times allowing the formation of more energetically stable domain configurations. The dependence was observed to stabilise to a constant ageing rate above poling times of 'several tens of minutes' [54] .

Pre-stress

From Eqn 1.13 it appears that pre-stressing affects the magnitude of the change in d_{33} observed during ageing due to a change in S_0. Whether this is an increase or decrease in magnitude will depend on the relative orientation of the pre-stressing with respect to S_0.

Sequential voltage drops

In the case that the poling field is not removed, but instead reduced, the behaviour of subsequent degradation in the piezoelectric constant must depend on whether the DW escapes its pinning via defects. The energy required to enable DW displacement in the presence of DW clamping via the volume mechanism is given by Eqn 1.16 of Robels and Arlt [75].

$$\Delta W_{DW}(t) = \Delta n(t) A |\Delta L| \Delta W_e \tag{1.16}$$

Here $\Delta n(t)$ is again, the number of defects oriented in the minimum energy configuration per unit volume, A is the area of the DW, ΔL is the DW displacement and ΔW_e is again the increase in electric field energy per unit area due to DW displacement. This should be compared with the potential energy saving from DW rearrangement to determine whether DW motion occurs upon a drop in voltage. The ageing curve should begin anew with altered parameters according to the new $\Delta n(t)$ if the DW is shifted. Note that a voltage change should be accompanied by a temperature change due to Joule heating at the electrodes and dielectric heating of the stack.

1.6.10 Deageing

In addition to ageing, deageing should be considered. The deageing process is essentially the removal of the elastic and or electrostatic ordering of lattice defects [55]. This can be achieved through application of a bipolar AC electric field, or by heating above the Curie temperature [52]. Heating above T_C should deage ageing due to any of the three

mechanisms listed above as the pinned domains in each case would cease to exist above this temperature.

Deageing via bipolar AC electric field in hard PZT ceramic is seen to have an activation energy of 0.55 to 0.70 eV - close to that of charge hopping conduction of the oxygen vacancy (energy required to move oxygen vacancy within lattice) so the two are proposed to be related [55]. Note, however, that Morozov and Damjanovic [55], and Robels and Arlt [75] quote different estimates of hopping conduction energy in PZT at 0.6 to 0.8 eV and 1.2 eV respectively. Carl and Härdtl also found a correlation between electrical conductivity and the activation field for deageing [76].

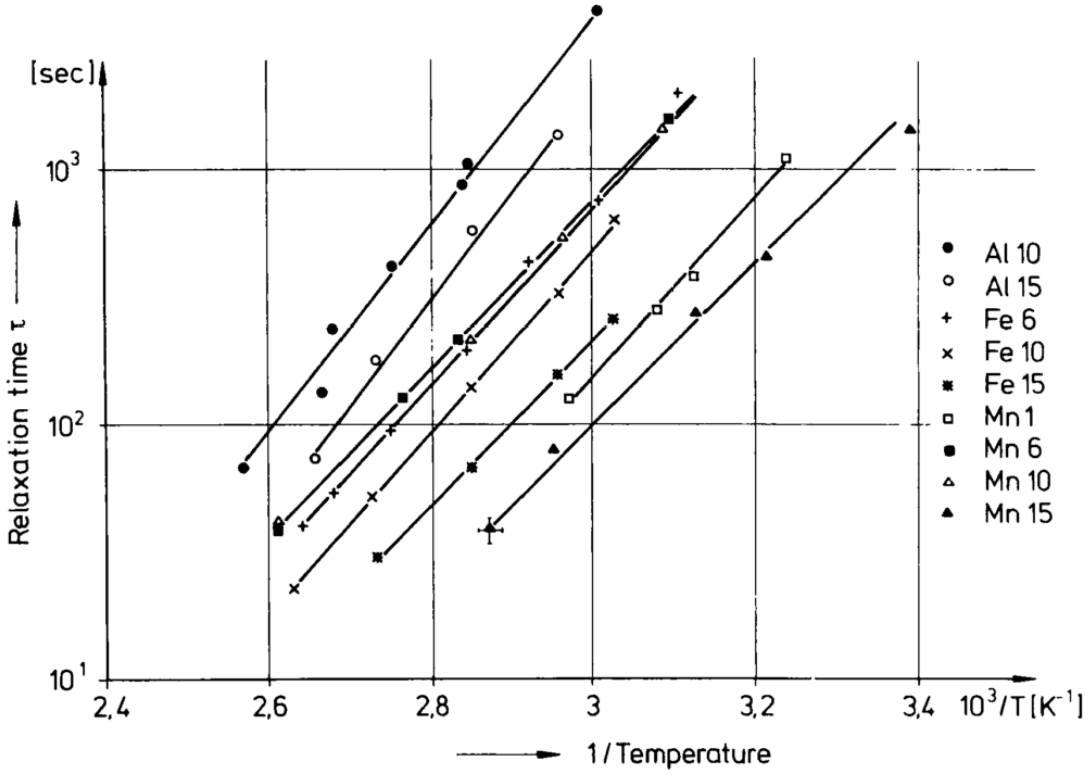

Figure 1.10: Arrhenius plots of deageing time for PZT subjected to a saw-tooth electric field function and doped with various dopants. Fig from [76].

The deageing duration is dependent on the amplitude of the AC electric field through

Eqn 1.17 and exhibits Arrhenius temperature dependence as shown in Fig 1.10 [76]. Genenko et al note that the deageing time is typically orders of magnitude less than the ageing duration [52].

It has been reported that the Arrhenius activation energy for deageing, U, is constant with varying electric field strength and time under field in the interval 25 kVcm^{-1} $\leq$ E $\leq$ 50 kVcm^{-1}. The activation energy was also observed to be dependent on both dopant species and concentration [76]. Carl and Härdtl fit an exponential function to their deageing curve. They noted that electric field strength affects the deageing time, τ, through Eqn 1.17 [76].

$$\tau = \tau_{\infty}(T)exp(\frac{E_A}{E}) \tag{1.17}$$

Here, τ_{∞} is a constant, E_A is an activation field strength and E is electric field strength. An estimate of the deageing temperature dependence could be made assuming an activation energy of 1 eV as it has been found to be 0.6, 0.7 and 0.8 eV for Mn, Fe and Al doped PZT respectively [76]. This would enable the determination of whether temperature need be taken into account in a deageing compensation procedure.

1.7 Accuracy requirements for LVTs

The University of Strathclyde is working to qualify the sensors against 5P20 protection class accuracy requirements outlined in IEC 60044-8-2002 [1]. Although this standard is intended for electronic CTs, it has been highlighted as the most relevant existing technical standard for the LVTs, as they are intended to monitor the secondary current of a CT. It is important to meet these standards if the sensors are to be adopted by industry. This section provides an overview of select accuracy requirements within IEC 60044-8-2002. The sensors have been demonstrated to meet these requirements under stable conditions, but there are concerns that this accuracy limit may be exceeded in the field due to cumulative error associated with undesirable PS behaviours, material degradation and inadequate temperature and hysteresis compensation.

The current error as defined in the relevant standard is given by Eqn 1.18

$$\epsilon(\%) = \frac{K_{ra} \cdot u_s - I_p}{I_p} \cdot 100 \tag{1.18}$$

where I_p is the RMS current through the transformers primary winding, u_s is the measured RMS secondary voltage and K_r is the rated transformer ratio. Furthermore, Eqn 1.19 gives the definition of composite error as defined in the relevant standard.

$$\epsilon_c(\%) = \frac{100}{I_p}\sqrt{\frac{1}{T}\int_0^T [K_{ra} \cdot u_s(t) - i_p(t - t_{dr})]^2 dt} \tag{1.19}$$

Composite error is an error term that takes into account both phase and magnitude error. This is given by the RMS value of the difference between, the instantaneous values of the primary current and the instantaneous values of the measured secondary current multiplied by the rated transformer ratio. It is expressed as a percentage of RMS primary current [1]. In the expression, t is time, t_dr is the rated time delay, T is the duration of one cycle and i_p is the instantaneous value of the primary current.

Table 1.1 shows accuracy requirements at rated primary current for protection class CTs and Table 1.2 shows harmonic accuracy requirements for protection class CTs.

Table 1.1: Accuracy requirements for protection class CTs from BS EN 60044-8:2002 [1].

Accuracy class	Current error at rated primary current %	Phase error at rated primary current		Composite error at rated accuracy limit Primary current %	At accuracy limit condition Maximum peak instantaneous error %
		Minutes	Centiradians		
5TPE	± 1	± 60	± 1,8	5	10
5 P	± 1	± 60	± 1,8	5	-
10 P	± 3	-	-	10	-

Table 1.2: Harmonic accuracy requirements for metering class CTs. Table from BS EN 60044-8:2002 [1].

Accuracy class	Percentage current (ratio) error (+/–) at harmonics shown below		Phase error (+/–) at harmonics shown below			
			Degrees		Centiradians	
	1/3rd (16,7 or 20 Hz only) harmonic	2nd to 5th harmonic	1/3rd (16,7 or 20 Hz only) harmonic	2nd to 5th harmonic	1/3rd (16,7 or 20 Hz only) harmonic	2nd to 5th harmonic
All protection classes XPXX	10 %	10 %	10	10	18	18

Table 1.3 shows accuracy requirements at rated primary current for metering class CTs and Table 1.4 shows harmonic accuracy requirements for metering class CTs. There are no composite error requirements for metering class CTs.

Table 1.3: Accuracy requirements for metering class CTs. Table from BS EN 60044-8:2002 [1]. Such CTs are used in combination with VTs for power metering. This table can also be found in the more recent IEC 61869-2:2012 Additional requirements for current transformers.

Accuracy class	± percentage current (ratio) error at percentage of rated current shown below				± phase error at percentage of rated current shown below							
					Minutes				Centiradians			
	5	20	100	120	5	20	100	120	5	20	100	120
0,1	0,4	0,2	0,1	0,1	15	8	5	5	0,45	0,24	0,15	0,15
0,2	0,75	0,35	0,2	0,2	30	15	10	10	0,9	0,45	0,3	0,3
0,5	1,5	0,75	0,5	0,5	90	45	30	30	2,7	1,35	0,9	0,9
1,0	3,0	1,5	1,0	1,0	180	90	60	60	5,4	2,7	1,8	1,8
NOTE The limit of current error and phase error prescribed for 120 % of rated primary current should be retained up to the rated extended primary current.												

Table 1.4: Harmonic accuracy requirements for metering class CTs. Table from BS EN 60044-8:2002 [1]. The current errors are chosen such that they add to 15%.

D.4.1.1 Power metering

Accuracy class	Percentage current (ratio) error (+/–) at harmonics shown below				Phase displacement (+/–) at harmonics shown below							
					Degrees				Centiradians			
	2nd to 4th harmonic	5th and 6th harmonic	7th to 9th harmonic	10th to 13th harmonic	2nd to 4th	5th and 6th	7th to 9th	10th to 13th	2nd to 4th	5th and 6th	7th to 9th	10th to 13th
0,1	1 %	2 %	4 %	8 %	1	2	4	8	1,8	3,5	7	14
0,2	2 %	4 %	8 %	16 %	2	4	8	16	3,5	7	14	28
0,5	5 %	10 %	20 %	20 %	5	10	20	20	9	18	35	35
1	10 %	20 %	20 %	20 %	10	20	20	20	18	35	35	35

Chapter 2

Investigation of effects due to piezoelectric stacks affecting LVT accuracy

2.1 Introduction

Experiments were conducted in order to simulate and characterise low voltage transducer (LVT) behaviour during an electrical fault on the power system under test, with the aim of characterising and compensating for piezoelectric ageing. This chapter describes the experimental set-up used, then looks for dependencies on physical parameters of the behaviour observed and examines the options regarding compensation and mitigation of the errors induced by undesirable piezoelectric behaviour.

2.2 Experimental set-up

Fig 2.1 displays the set-up used in experiments in this chapter. Up to four LVTs were connected electrically in parallel and optically in series via coaxial cables and single mode fibre respectively. LVTs referred to as packaged are immersed in a viscous gel and hermetically sealed in a kovar package. Both unpackaged and packaged LVTs were included in these tests so that any unintended effects on LVT behaviour due to the packaging could be identified. A broadband light source illuminated the FBGs via a fibre circulator, and four unique Bragg peak wavelengths were reflected into a fibre port of an OEM FBG interrogator. A Chroma 61512 current source was used in combination with Chroma Softpanel software to provide a sequence of predefined voltages for predefined durations. The FBG interrogator interfaced with a dedicated LabVIEW program, which post-processed and saved the data. The LVTs were contained within a Thermotron S16 environmental chamber for temperature control and chamber temperature was monitored via USB resistance temperature detector (RTD) and data logger, and data saved at the PC. In each test the optical signal recording was manually initiated immediately after starting the voltage stepping program. All applied voltages in this chapter are 50 Hz.

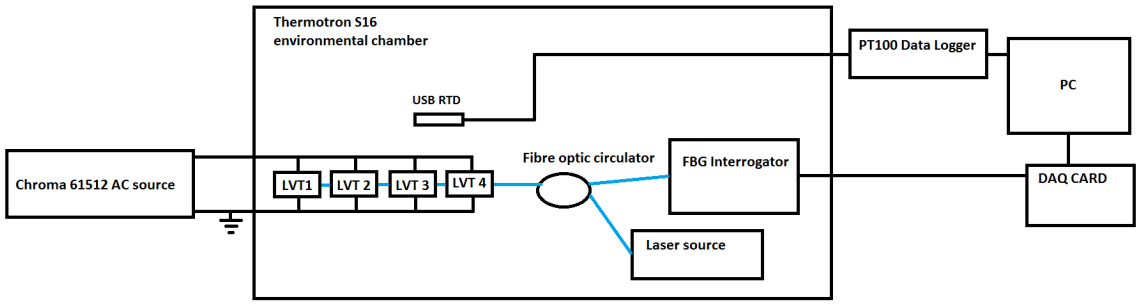

Figure 2.1: Experimental set-up for ageing investigation experiments

2.3 Optical sensitivity decay

An LVT was placed in an environmental chamber and supplied with a voltage signal from a Chroma 61512 source, whilst temperature was maintained at 25 °C. Upon subjection to 20.4±0.3 V_{RMS}[1] for ten seconds, then a return to 0.6±0.3 V_{RMS} the LVT was observed to undergo a logarithmic decay in RMS reflected Bragg peak wavelength on the time-scale of hours. Eqn 2.3 describes the empirically determined decay in the 50 Hz component of the RMS reflected Bragg peak wavelength; herein referred to as the optical sensitivity (OS).

$$OS = A - Bln(t/\tau) \tag{2.1}$$

Here t is time from decay initiation, τ and A are constants depending on the initial conditions and B is a constant indicating the rate of the decay. The function has been used by NASA [62] in describing PS (piezoelectric stack) stroke degradation (fatigue) over a much longer time-scale. It is used to fit the ageing curves of various physical properties of ferroelectrics [46, 84]. The decay should always take this form, whilst the parameters will vary. The logarithmic form arises from the sum of a range of exponential decays with different relaxation time-scales [76]. This degradation introduces an error into the LVTs voltage measurement, and the present chapter therefore looks for factors upon which the parameters in Eqn 2.3 are dependent, and considers reduction and compensation of the associated error. Fig 2.2 shows an example curve. The error is typically initially of the order of 1% of the optical sensitivity[2], and decays to zero on the time-scale of hours. In this example, the stack was subjected to a short 28.8±0.4 V_{pk} pulse, 0 V for 30 s, then

[1] Voltage errors in this chapter come from the Chroma 61512 uncertainty in voltage output. The values 20.4 V_{RMS} and 0.6 V_{RMS} roughly correspond to the maximum voltage required to be measured for a 5P20 sensor; 20 V_{RMS}, and nominal voltage; 1 V_{RMS}. The discrepancies between the values are due to an early calibration indicating that the voltage source output was slightly higher than programmed, however a more recent calibration indicated that the voltage source output was within the voltage output uncertainty.

[2] For context, recall that the 5P class current error accuracy requirement at rated primary current is also 1% [1]

0.6 V_{RMS} for 2 hr, to simulate a short transient followed by activation of circuit protection systems and a return to nominal voltage.

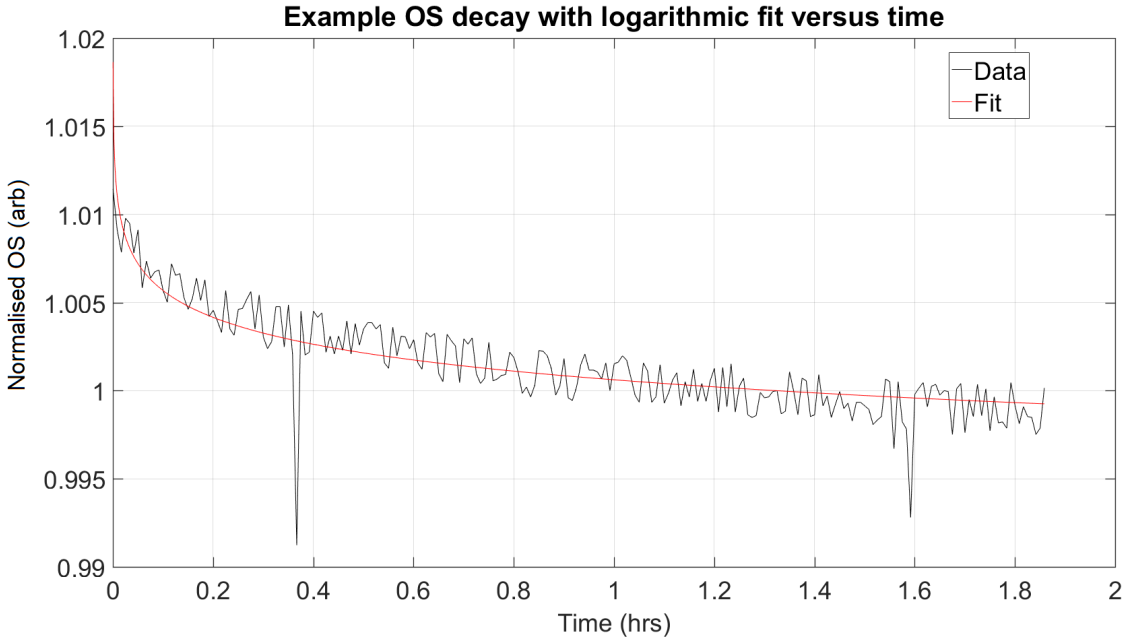

Figure 2.2: Example normalised OS decay and fit using Eqn 2.3. The stack was subjected to a short 28.8±0.4 V_{pk} pulse, 0 V for 30 s, then 0.6±0.3 V_{RMS} for 2hr, to simulate a short transient followed by activation of circuit protection systems and a return to nominal voltage.

In the aforementioned experiment and those that follow, the degradation in OS was initially attributed to ageing under fatigue conditions, though the discussion in section 2.13 subsequently called this into question. As stated in Chapter 1, Genenko et al [52] define ageing as 'degradation with time in the absence of an external electrical or mechanical load'. Although, in the present application the PS is not operating in the absence of external electrical field, this thesis proposes that the mechanisms of ageing may also be apparent in the short term degradation seen. The observed effect has been differentiated from fatigue because a trigger - reduction in voltage across the PS - is required to initiate decay. This degradation is relevant to the sensor performance in the event of a fault on the

electrical system under measurement for example, upon which the sensor will experience a short voltage transient up to 30 times the nominal voltage in the case of a 5P30 sensor[3]. Upon returning to nominal voltage, the device OS will have changed and will take time to return to its pre-fault state.

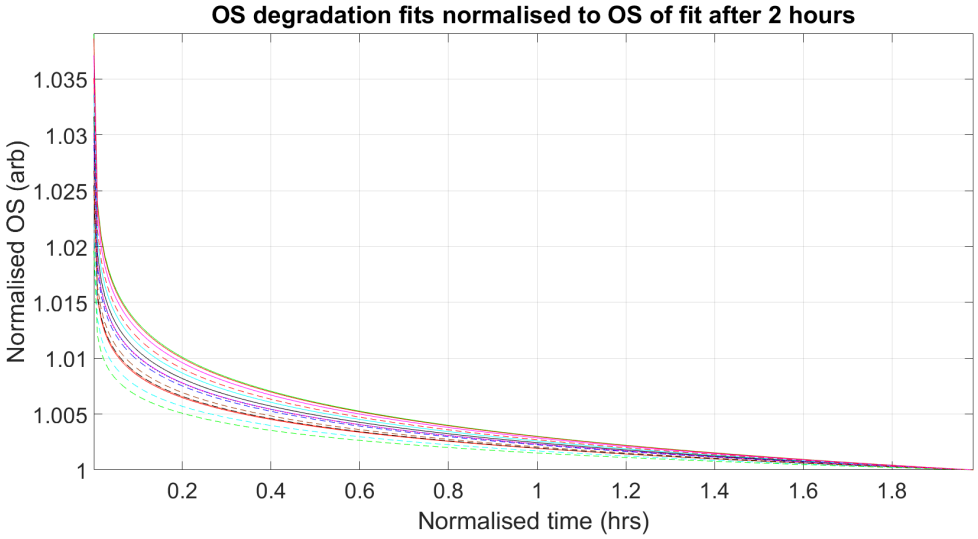

Figure 2.3: 15 OS degradation fits from 15 identical runs from an unpackaged LVT, each normalised to the fit value at ~2 hr. The stack was subjected to a short 28.8±0.4 V_{pk} pulse, 0 V for 30 s, then 0.6±0.3 V_{RMS} for 2 hr. Eqn 2.3 has again been used as the fitting equation.

This is illustrated in Fig 2.3, in which the decay in OS is shown over two hr at nominal voltage, directly following a transient of 28.8±0.4 V_{pk}. The degradation has been fitted with Eqn 2.3. 15 OS fits from an unpackaged LVT are shown, each normalised to the fit value at ~2 hr. The stack was subjected to a short 28.8±0.4 V_{pk} pulse, 0 V for 30 s, then 0.6 V_{RMS} for 2 hr. For each fit the initial OS change is observed to exceed the 1% error limit defined by IEC 60044 [1] relative to the final measurement point.

[3]Grid transients are discussed further in Chapter 4

2.3.1 Modification of ageing rate

If the observed degradation can be attributed to ageing, there exist two options in attempting to minimise its effect on voltage measurement accuracy; change the ageing rate, or compensate for the ageing using software.

In modifying the ageing rate, it can be either accelerated, such that the decay in OS is instantaneous, or reduced, such that the decay is over such a long time-scale so as to be unnoticeable. This would be achieved through modifying the physical make-up of the PZT (lead zirconium titanate). In order to increase the ageing rate, donor dopant concentration, Zr/Ti ratio, grain size or impurity concentration could be increased, or acceptor dopant concentration could be decreased. These modifications would require the following extra considerations. Increasing the donor dopant concentration and reducing the acceptor dopant concentration would soften the PZT, i.e increase its sensitivity to applied electric fields. The effect of modifying the Zr/Ti ratio would depend on the present ratio, but would likely involve a move away from the morphotropic phase boundary, lowering d_{33}. The effect of a reduction in grain size could be to increase sensitivity of the ageing rate to temperature and frequency of applied voltage signal. A combination of these modifications could also be applied.

Similarly, to reduce the ageing rate, donor dopant concentration, Zr/Ti ratio, grain size and impurity concentration could be decreased and acceptor dopant concentration increased. The opposite of the above listed caveats would apply. Finally maintaining a temperature conducive to fast or slow ageing could work to remove the problem, but this would necessitate active temperature control, increasing sensor complexity and as such will not be considered here.

Although presented here for completeness, changing the material composition of the PZT is likely to reduce the piezoelectric constant, thereby reducing LVT OS. Furthermore, finding a suitable alternative is beyond the scope of this thesis and as such the option of modifying the ageing rate through altering the chemical make-up of the PS is not

further considered. Further work may, however, experimentally investigate alternatives, as reducing the time taken to perform real time compensation subsequent to fault becomes a greater priority with increasing number of LVTs multiplexed.

Owing to the law of large numbers, it may be found that the reproducibility and repeatability of sensor ageing can be improved through using wider and longer PSs. Each ageing decay will be the result of a larger sample of diffusive events, and therefore the parameters in the logarithmic equation will exhibit a narrower Gaussian distribution around their expected values.

2.3.2 Compensation of ageing process in software

Having ruled out testing different materials in the present work, compensation of the ageing process in software is considered. Further investigation is required to determine which of the below listed cases best fits the requirements of the AST (Advanced Sensors Team). Each ageing curve is assumed to take the same form as Eqn 2.3, with parameters B and τ to be determined. Care must be taken not to use $t < \tau$ values to avoid computational error. In compensation a log term could be added to the OS to maintain the sensitivity at the value on initiation of the ageing process. Alternatively, a log term could be added, then the difference between the original wavelength and the totally aged wavelength subtracted, to always maintain the aged value. A proper treatment may also require the original poling direction to be taken into account. In this section, three separate cases requiring different compensation approaches are considered.

1. CASE: The ageing curve is to a good approximation the same every time.

   Constantly add a log term, resetting t upon any change in peak-peak voltage exceeding a predetermined threshold. This threshold could be decided based on experimental data and would correspond to the voltage change at which the stack is deaged enough to exhibit an unacceptable (1%) voltage measurement error due to difference in real and compensated-for ageing rate. A similar threshold for temperature

changes could also be implemented. The temperature dependence of ageing rate over the intended working range of -5 to 40° C should also be experimentally investigated, as a look-up table of parameters calibrated for increments within this range may be required. It may be found that the ageing rate is so much accelerated/retarded that compensation is only required within a subsection of this range.

2. CASE: The ageing curve parameters follow a statistical distribution.

   This scenario presents two options, with the optimal solution dependent on the distributions variance. Predetermined mean parameter values could be used, or alternatively, parameters measured using the process described in case 3 could be used for compensation. The former would introduce statistical error, whilst the latter would involve a delay due to processing time and the necessity of waiting out a few data points before the parameters can be accurately determined.

3. CASE: The ageing curve parameters take random values.

   In this case, Bayes' theorem can be used to improve the real time optical sensitivity degradation fitting through using a pre-determined distribution of parameter values. Bayes' theorem, Eqn 2.2,

$$P(X|Y) = P(Y|X) \cdot P(X)/P(Y) \tag{2.2}$$

   states that the posterior probability of obtaining data X, given hypothesis Y, is proportional to the likelihood of the hypothesis, given the data, $\mathrm{P}(Y|X)$, times the prior probability of the data $\mathrm{P}(X)$. An array of previous signal values could be stored on the interrogator's real-time processor, which would be reset upon breach of the voltage and temperature thresholds of case 1. This array would be used to produce an increasingly accurate fit with increasing number of data points acquired, using logarithmic least squares fitting. This would necessitate a delay due to processing. Upon reaching a number of points deemed enough to create a reliable fit, the pa-

rameters could be locked for the remainder of the ageing process to save processing time. Upon initiation of an ageing decay, the initial voltage measurements have the greatest error prior to compensation, however the information from which to obtain a fit for compensation is limited.

In order to minimise the error on instantaneous voltage data-points, Bayesian inference fitting based on previously measured and stored probability distributions of ageing parameters could be applied. The fitting would be initially weighted towards the mean values of the recorded probability distribution, and in the limit of a large number of optical sensitivity data points, the parameter estimation would tend towards least squares estimation.

A brief description of the proposed algorithm follows. An array of (dependent variable) optical sensitivity data and an array of (independent variable) logarithmic time data are taken as inputs, along with the prior covariance matrix of the fitting parameters for a linear fit, estimated using the mean and standard deviation of fits from prior experiments on a statistical sample of repeated simulated decays. An expression for the posterior covariance matrix of the probability distribution of fitting parameters is determined using Bayes' theorem, assuming Gaussian distributions for the likelihood function for the data, given the hypothesis (fitting parameters), and for the parameters of linear fit. Lastly, the posterior mean of the probability distribution of the array of fitting parameters is calculated. This contains the coefficients for a fit, which is subtracted from the data to achieve compensation.

When using adaptive compensation, i.e. that with parameters that update in real time, care must be taken to avoid unintentionally 'compensating out' real data trends. One approach to avoid unintentionally 'compensating out' real data trends further uses Bayesian inference. In this approach, the likelihoods that the deviation of incoming optical sensitivity data from constant is due to noise, ageing, and real data trends are estimated. The change is then assigned to whichever of these options has

the maximum likelihood, and the appropriate measure taken accordingly (compensate or do not). One further ageing compensation method is highlighted in section 2.13.

2.4 Ageing / deageing transition

The literature indicates that ageing via the volume mechanism can be reversed through application of a 'strong' bipolar electric field [80]. For example Cain et al observed significantly reduced degradation of piezoelectric samples when samples were intermittently subjected to a field of 300 $V_{pp}mm^{-1}$ [85]. This electric field, however, needn't exceed the coercive field [58]. If then, the OS degradation is attributed to ageing, above a threshold applied voltage, a transition from ageing to deageing is expected upon a voltage sequence involving an elevated voltage in the form of grid fault, then a return to nominal, and finally another step up in voltage. In the deageing process the sign of the logarithmic term in Eqn 2.3 is positive. Eqn 2.3 describes the increase in OS ascribed to piezoelectric deageing.

$$y = A + Bln(t/\tau) \tag{2.3}$$

If, after the experiment introduced in section 2.3, the voltage was to return to 20 V_{RMS}, an increase in OS with time towards an equilibrium OS would be expected. The OS for a packaged sensor shown in Fig 2.4 appears to demonstrate such a transition. The duration of this OS increase would correspond to the deageing time. Upon subsequent removal of deageing mechanisms, (in the present application, the large amplitude AC voltage) the ageing process would begin anew.

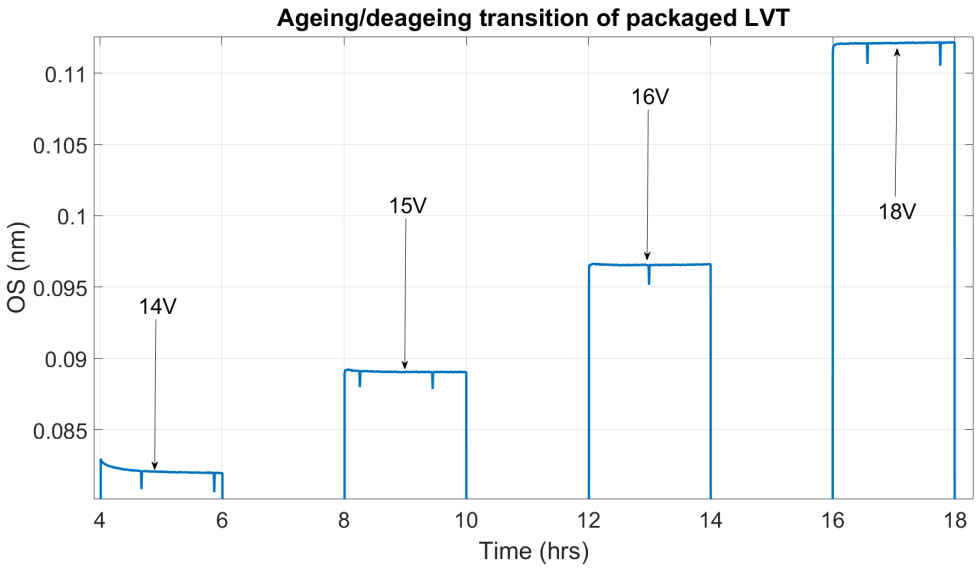

Figure 2.4: Packaged LVT OS; the driving voltage is stepped up from 0.6±0.3 V_{RMS} to increasing RMS voltage levels as enumerated in the plot. As the magnitude of the positive voltage step is increased, a change in the gradient of the initial OS subsequent to the voltage change is observed.

Fig 2.4 shows the OS of a packaged LVT, during which the driving signal is stepped up from a nominal of 0.6±0.3 V_{RMS} to increasing RMS voltage levels as enumerated in the plot. Four LVTs connected electrically in parallel were subjected to a 20.4±0.3 V_{RMS} transient for 80 ms, then 0.6±0.3 V_{RMS} for four hr, before the step increase to 14±0.3 V_{RMS} seen in the figure. As the magnitude of the positive voltage step is increased, a change in the gradient of the initial OS subsequent to the voltage change is observed between 16 and 18±0.3 V_{RMS} . The change has been attributed to a transition between ageing and deageing in the PS. Of the four LVTs in the test, however, only one displayed this behaviour, with the other packaged LVT and two unpackaged LVTs instead exhibiting deageing curves similar to that shown at 18±0.3 V_{RMS} in Fig 2.4 upon each step up in voltage.

After seeing the deageing curve in several runs, to better understand the LVTs behaviour, an algorithm was sought to predict whether, upon a change in voltage, an ageing or deageing behaviour would be seen. Upon a step increase in RMS voltage magnitude, the defects within the sample are thought to diffuse towards new energy minimising configurations producing the ageing characteristic. Above a threshold voltage, the energy provided by the electric field is great enough to de-pin the domains and deageing occurs. Initially therefore, a simple threshold electric field was sought. In total 93 runs between four LVTs, in which the OS was monitored upon a step increase in RMS voltage magnitude after a period of two hr at 0.6 V_{RMS}, were manually categorised by:

- LVT considered
- RMS voltage during run
- Class of ageing curve, deageing curve, ambiguous or no curve.

The results shown in Table 2.1 indicate that the investigated parameters are not enough to determine a rule, and that a model containing the hypothesis of a threshold voltage is an oversimplification of the problem.

Table 2.1: Table of ageing and deageing events, showing no clear threshold voltage. In each experiment represented by a coloured block, voltage was increased directly from 0.6±0.3 V_{RMS} to the voltage indexed in the left column after a period of two hr at 0.6±0.3 V_{RMS}.

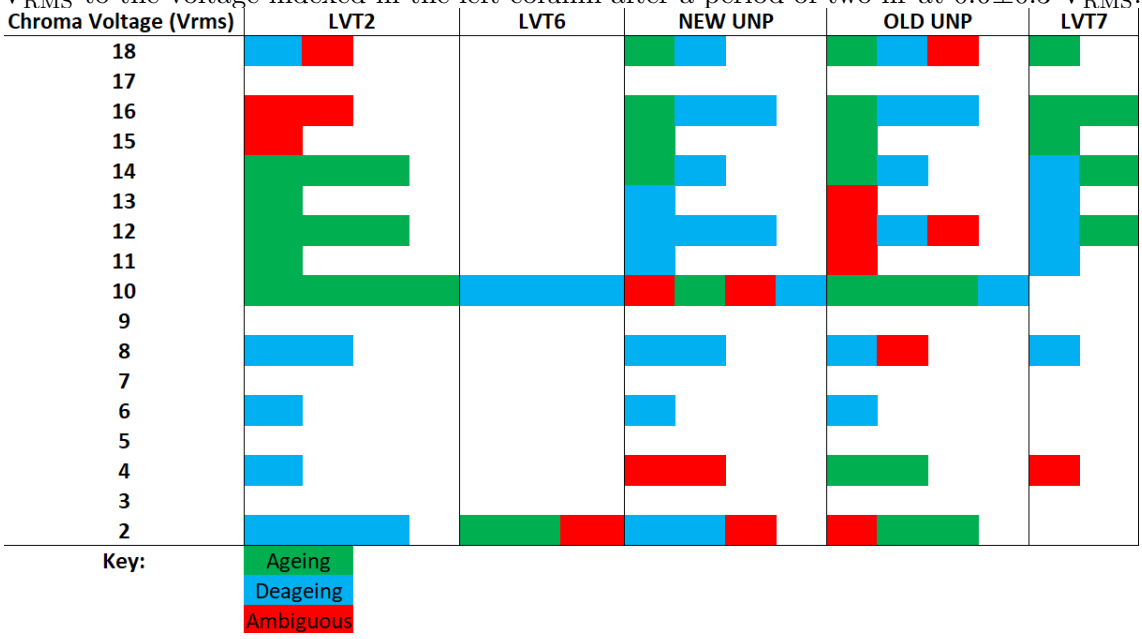

Next, characterisation of LVT behaviour using a multi-parameter model was tested. A Gaussian Naïve Bayes classifier[4] was used in an attempt to find a correlation between class and the aforementioned parameters. Advantages of using such a classifier over simply plotting the variables against class, are that it gives a numerical value of the accuracy of the prediction, which is useful in deciding which parameters to take forward in model improvement and also that it avoids the problem of visualising data correlations in multi-dimensional parameter spaces.

[4]The program can be summarised as follows. The training data is separated by class, and the probability of a given run in the training set belonging to each class respectively is calculated. For each class the mean and standard deviation is calculated for each of the parameters described in the text. These values are used to produce a Gaussian probability distribution function (PDF), for each parameter within each class. The test data is iterated through and the probability that a given run belongs to each class is calculated using the Gaussian PDFs, under the assumption that each parameter is independent of all others. If the conditional probability that a given run in the test data displays a deageing characteristic given its set of parameter values, is greater than 50%, it is classified as deageing, else it is classified as ageing.

Data for 178 runs, each containing up to four LVTs, was manually classified for the six LVTs in the study as ageing or deageing. Four of the LVTs were packaged, one unpackaged with end blocks and one unpackaged with the FBG directly bonded to a PS of different dimensions to that of the other LVTs. LVT construction is further detailed in Appendix A. For each run, the following parameters were recorded:

- RMS voltage during OS monitoring
- RMS voltage immediately before OS monitoring
- Change in RMS voltage (magnitude and sign) upon beginning OS monitoring
- Duration held at voltage immediately before beginning OS monitoring

The data was cleaned to remove the runs for which data was incomplete or ambiguous. It then consisted of 400 runs classified as ageing and 94 as deageing. Upon each iteration of the program, this data was randomly permuted using a random number generator and 67% was chosen for model training, with the remaining 33% used for testing.

Upon completion of all predictions using the Naïve Bayes classifier, the accuracy of the model was determined through comparison of the predicted test set classes to the actual test set classes. Given that 81% of the dataset used belongs to the ageing class, an accuracy of greater than 81% is required for a given model to be an improvement on simply guessing ageing for each class. Upon running the program five times, the mean accuracy of the models was 94.4%, indicating that one or more of the variables used, or the combination of them, was correlated with class. Upon testing individual parameters using the classifier, RMS voltage during OS monitoring, and change in RMS voltage (magnitude and sign) upon beginning OS monitoring both showed correlation; producing 87.1% and 89.9% accuracy respectively, again over five iterations of the program.

Given that these parameters showed correlation, they were taken forward into the next version of the model. The parameters RMS voltage immediately before OS monitoring, and duration held at voltage immediately before beginning OS monitoring, were removed from

the model. The behaviour of the PS was expected to depend on the history of PS exposure to electric field. For each run now, the two hour period immediately prior to the run, was characterised according to the sequence of RMS voltages seen by the PS during this period. The period was split into bins corresponding to 15 s intervals, a threshold voltage was subtracted from the RMS voltage versus time function, and any resulting negative values zeroed. Next the function was weighted using a mapping onto the interval ln(1) to ln(e). The increasing logarithmic weighting from zero to one across the time period is intended to reflect the logarithmic dependence of the ageing curve, and the threshold as a voltage above which domain wall de-pinning occurs. Finally, the function was integrated with respect to time to give a single parameter for each run. This process was iterated over thresholds in the range 1 to 20 V_{RMS}, in increments of 1 V_{RMS} .

This new parameter was used in the Naïve Bayes classifier along with the RMS voltage during OS monitoring, and change in RMS voltage (magnitude and sign) upon beginning OS monitoring parameters from the previous version. 412 runs were evaluated, of which 21% were characterised as deageing, therefore an accuracy above 79% was sought. The mean accuracy was seen to vary little with threshold (standard deviation of 1.6%) and the mean of the mean accuracy over 20 threshold values, and 10 iterations of the program was 77.4%; not an improvement over flipping a coin to decide class.

It was thought that the threshold voltage may vary between PSs, therefore the Naïve Bayes program was run once again, for a single unpackaged LVT, using the same parameters. 136 runs were evaluated, 30% of which belonged to the deageing class. Again, 20 threshold voltages were iterated over, and the classifier was iterated over 100 times for each threshold. The results are shown in Fig 2.5. The mean accuracy across all thresholds was 88.5% with standard deviation 7.8% and the mean accuracy was observed to drop significantly for threshold voltages above 14 V_{RMS} . The mean of the mean accuracy across thresholds up to and including 14 V_{RMS} was 93.1% with standard deviation 1.4%. The results indicate that the correct threshold voltage may lie between 13.7 and 15.3 V_{RMS} taking into account the error on the voltage output of the Chroma source, however, it

could also be the case that the weighted integral of voltage with respect to time holds the important information in this parameter and the drop in accuracy above a threshold of 14 V_{RMS} comes from a sharp decrease in the information available in the model. The same parameters were then used on data from an unpackaged LVT in which 78% of the runs were classed as ageing. With a threshold voltage of 1 V, over 100 iterations the model achieved an accuracy of only 75.8% indicating that the model is still incomplete.

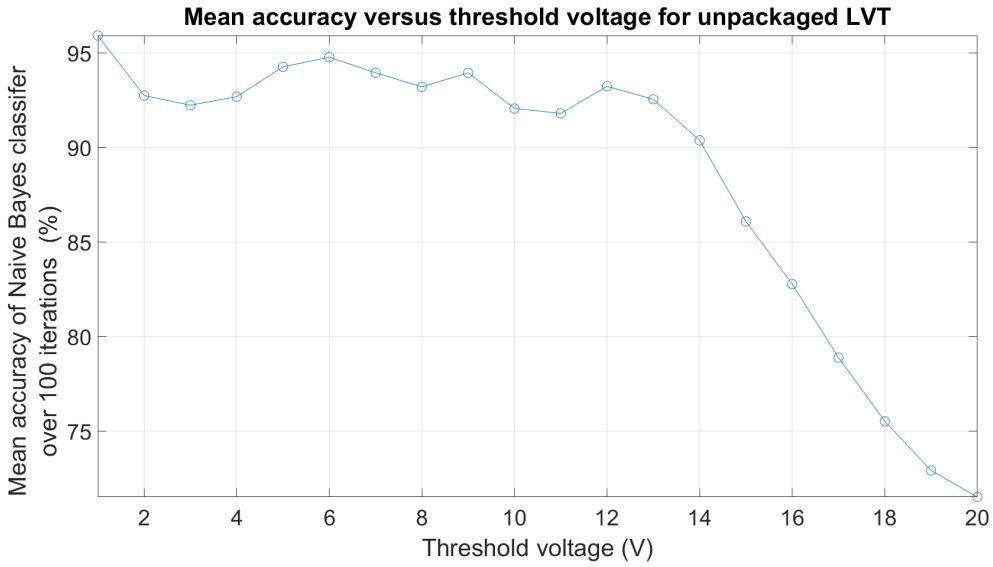

Figure 2.5: Mean accuracy of Naïve Bayes classifier versus threshold voltage for an unpackaged LVT. Each point represents the mean accuracy of 100 models.

A final measure was taken to attempt to improve the accuracy of the model. The approximate mean reflected Bragg peak wavelength, λ_{Bav}, was noted prior to each run for a packaged LVT and this was included in the model. Variations in this parameter should be due to variations in PS remnant polarisation or self heating of the PS, assuming that the chamber temperature is constant across all runs[5]. This parameter could further be affected by humidity absorption of the polyimide coating on the FBG. The results when this parameter was included, at a threshold of 1 V with 100 classifier iterations,

[5]Over the runs considered there is a variation in temperature of 26.4 to 27.0±0.1 °C

were not improved on those previously attained without the parameter. For this reason it is expected that models using these parameters would be unsuccessful upon application to the unpackaged LVT. It may be the case that this model can be improved through modifying the PDF functions in the classifier as the PDF of both the RMS voltage during OS monitoring of a considered run, and the thresholded, weighted integral of the RMS voltage prior to OS monitoring, would both be better approximated with skewed Gaussian functions.

To summarise, a boundary in parameter-space separating runs that display ageing and those that display deageing has not been found. For the most part, deageing should not be concerning for operation of the device under consideration, as accuracy requirements are relaxed during a voltage transient, and these are typically of order tens of milliseconds. The subsequent ageing upon returning to nominal, as shown in Fig 2.3, remains a concern however and must be compensated for in optical signal processing. In addition, deageing remains a problem upon activation of the LVTs, after a period of no applied voltage, as will be seen in section 2.11, and thus should be further investigated for a fuller understanding of LVT behaviour.

2.5 Test of deageing relation of Carl and Härdtl

According to the experimentally determined Eqn 1.17, a plot of DC voltage applied to deage a sample versus the natural logarithm of the characteristic deageing relaxation time should display a linear relationship. Such a relaxation time should be proportional to the rate of change of OS, which in Eqn 2.3 is proportional to the B parameter. Thus a linear relationship between V and $\ln(B)$ may be expected if this relation holds.

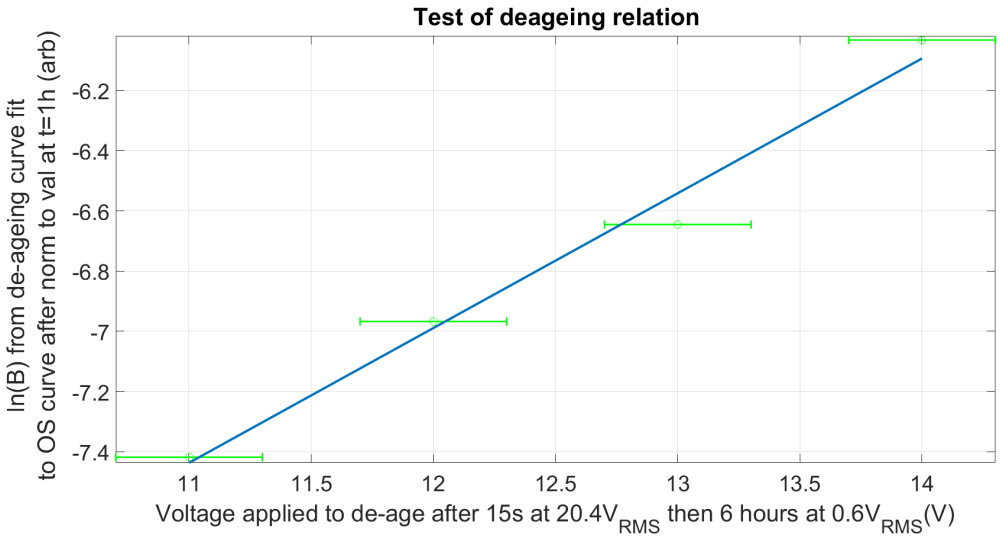

Figure 2.6: Test of relation of Carl and Härdtl; RMS voltage applied to deage sample after 15 s at 20.4±0.3 V_{RMS}, followed by six hr of 0.6±0.3 V_{RMS} V vs $\ln(B)$

Figure 2.6 shows that the relation appears to hold for a single packaged LVT, however further data-points should be plotted to confirm this.

2.6 Frequency dependence of normalised OS decay B parameter

Three otherwise identical programs were conducted on two packaged and two unpackaged LVTs at 100±0.15 Hz, one at 50±0.08 Hz and three at 15±0.02 Hz. Although the LVTs will not see such extreme fundamental frequencies as 100 Hz and 15 Hz, any frequency-dependent changes in degradation rate would be exaggerated in comparison with those seen within the nominal range and so could be determined with greater ease. The UK grid code specifies that the sensors will be subject to a fundamental harmonic frequency range of 49.5 - 50 Hz in the field and 47 - 52 Hz in exceptional circumstances.

Figures 2.7, 2.8, 2.9, and 2.10 show normalised fits to the degradation curves, plotted against the natural logarithm of time in seconds since removal of the trigger, for two packaged and two unpackaged LVTs. Results show no clear correlation between degradation rate and frequency. In each case the LVTs were subject to a 20.4±0.3 V_{RMS} sinusoidal waveform for 15 s, before returning to 0.6±0.3 V_{RMS}.

For some data, noise prevented convergence of the fitting program upon trying to fit a logarithmic fit, and as such linear fitting on a logarithmic time-scale has been used. Neither least squares nor robust regression algorithms were successful in those cases. The same result; no clear correlation between ageing rate and frequency, was seen when Eqn 2.3 was used as the fitting equation, upon omitting data that could not be fit. Linear fitting was chosen as the best alternative to logarithmic fitting, as upon testing, moving average smoothing introduced artefacts in the data.

Upon increasing the frequency, there should be an increase in work done per unit time by the PS, leading to self heating. If significant in the ageing process, the effect of the heating would be to accelerate diffusive processes and provide the domains with more energy to escape pinning. Thus the effect of increasing frequency should depend on the relative strengths of the these effects. For example, Lente and Eiras found that under a sinusoidal 'high' electric field greater than the coercive field, the magnitude change in

polarisation caused by fatigue in a donor doped PZT ceramic is increased at 60 Hz relative to that at 0.1 Hz. This was attributed to self heating[6] of the stack at the higher frequency [86]. The results presented in Figs 2.7 to 2.10 indicate that either these effects balance out at the frequency and electric field applied, or that the associated change in PS temperature with frequency is not pronounced enough to have a noticeable effect.

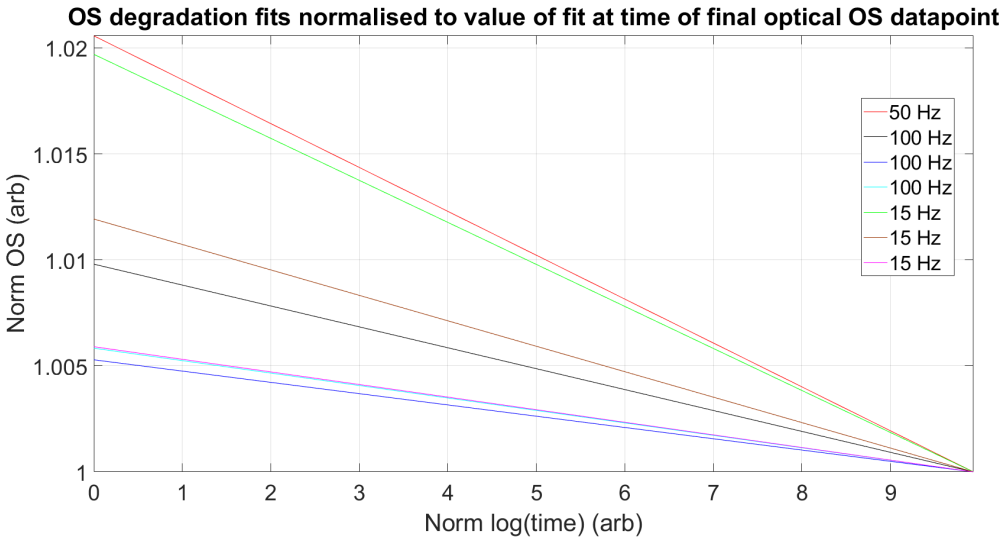

Figure 2.7: Ageing curve fits upon dropping to 0.6±0.3 V_{RMS}, after a 15 s period of 20.4±0.3 V_{RMS} at 15, 50 and 100 Hz for a packaged LVT

[6]Temperature was monitored using a thermocouple attached to the sample surface with thermally conductive adhesive and an increase in temperature of ~50 °C was measured upon initiating cycling at 60 Hz, whilst temperature remained constant at 0.1 Hz.

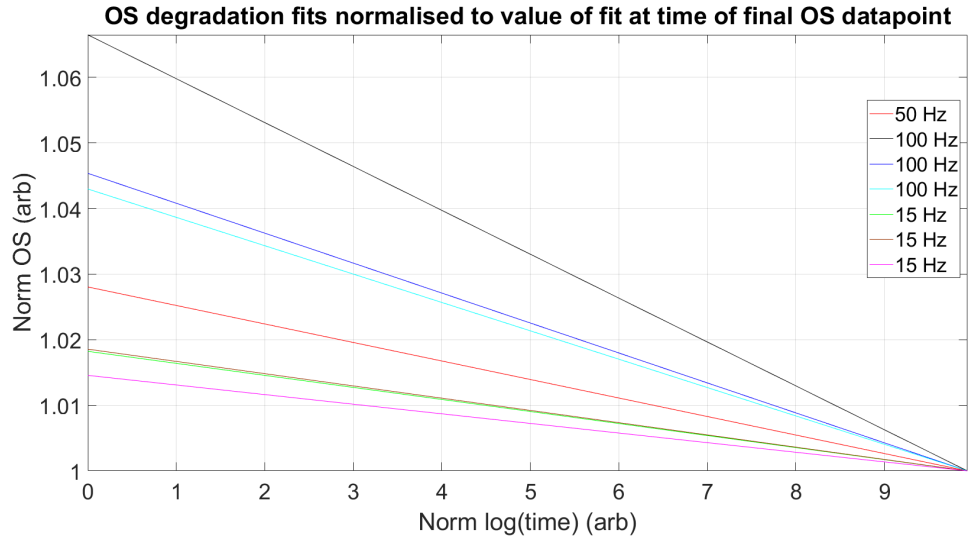

Figure 2.8: Ageing curve fits upon dropping to 0.6±0.3 V_{RMS}, after a 15 s period of 20.4±0.3 V_{RMS} at 15, 50 and 100 Hz for another packaged LVT

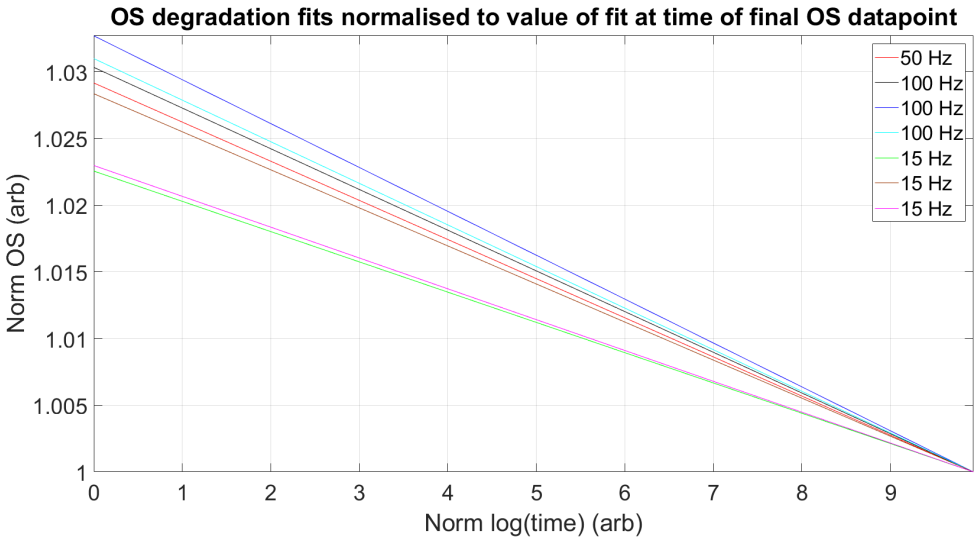

Figure 2.9: Ageing curve fits upon dropping to 0.6±0.3 V_{RMS}, after a 15 s period of 20.4±0.3 V_{RMS} at 15, 50 and 100 Hz for an unpackaged LVT with end blocks

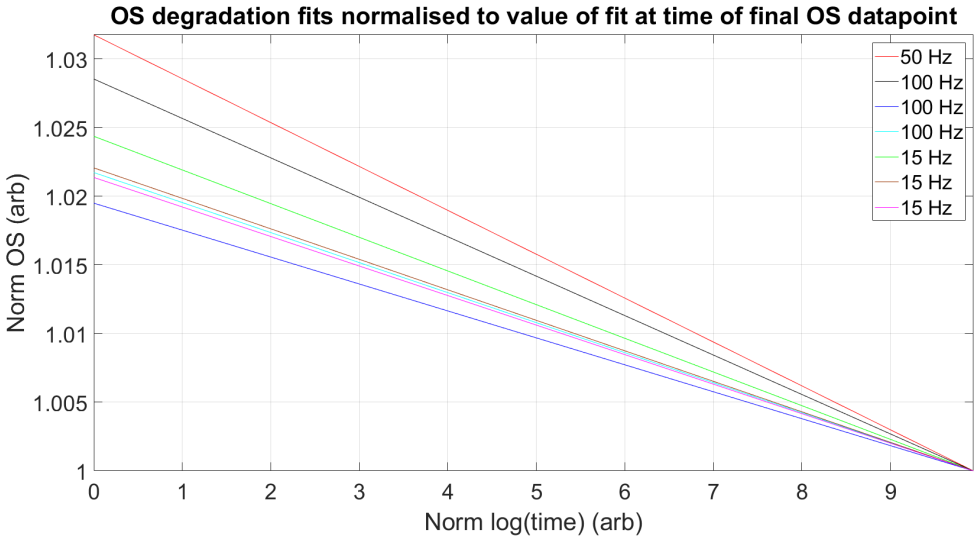

Figure 2.10: Ageing curve fits upon dropping to 0.6±0.3 V_{RMS}, after a 15 s period of 20.4±0.3 V_{RMS} at 15, 50, 100 Hz for a directly-bonded unpackaged LVT

2.7 Voltage step decrease magnitude dependence of normalised ageing decay B parameter

It was thought that the PS may exhibit greater B parameter in Eqn 2.3, upon return to nominal, if subjected to voltage transients of greater magnitude. In the ageing process, upon returning to a lower voltage from a higher voltage, the polarisation of the domains reorients instantaneously towards the spontaneous stack polarisation. The system has now changed and polar defects within the sample begin to rotationally diffuse to minimise the systems potential energy. It stands to reason that upon a greater change in spontaneous polarisation, corresponding to a greater change in applied electric field across the stack, that the potential energy of the polar defects should be displaced further from the minima. Furthermore, if said potential energy function is a parabola for example, the functions gradient may be expected to steepen, with greater displacement from the minima. This means that the defects may act to return to the minima, at a greater rate than they

otherwise would if they were displaced less on the potential energy parabola. For this reason, a greater change in voltage, could increase the rate of ageing via the domain mechanism.

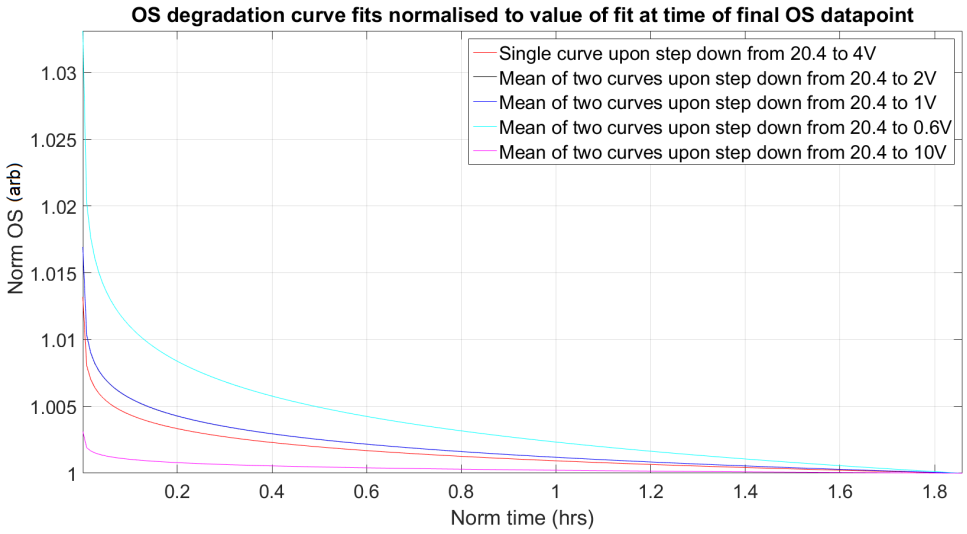

Figure 2.11: Average normalised ageing curves for steps down from 20.4 to 10, 4, 2, 1 and 0.6±0.3 V_{RMS} for an unpackaged LVT

Fig 2.11 displays average normalised ageing curves for steps down from 20.4 ± 0.3 V_{RMS} to 10, 4, 2, 1 and 0.6±0.3 V_{RMS} for an unpackaged LVT. The curve corresponding to the mean of two fits upon step down from 20.4 to 2±0.3 V_{RMS} is obscured by the curve corresponding to the mean of two curves upon step down from 20.4 to x±0.3 V_{RMS}. No dependency of the ageing rate on the magnitude of the voltage step decrease can be seen.

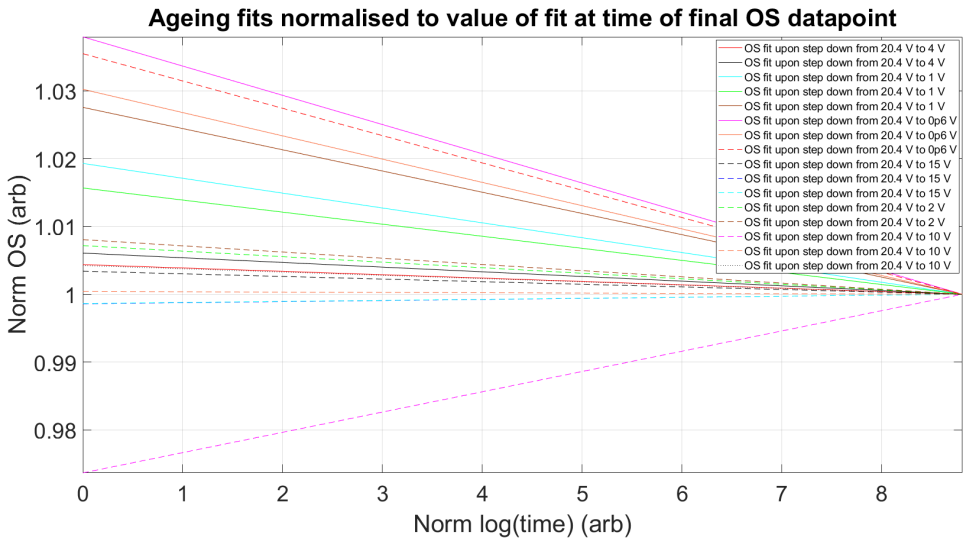

Figure 2.12: Normalised ageing curves for voltage step decreases from 20.4 to 10, 4, 2, 1 and 0.6±0.3 V_{RMS} for a single unpackaged LVT. The curves presented are linear fits on a logarithmic time-scale.

As Fig 2.11 required the omission of some data for which the fitting algorithm would not converge, the full larger sample size dataset is shown in 2.12 with linear fitting on a logarithmic time-scale. Still, no dependency of the degradation rate on the magnitude of the voltage step decrease is seen.

2.8 Voltage step increase magnitude dependence of normalised deageing curve B parameter

In analogy with the above section, it was thought that the PS may exhibit greater B parameter in Eqn 2.3, upon a greater step increase in voltage. Figures 2.13, 2.14 and 2.15 display normalised linear OS degradation fits for steps up in voltage to 4, 6, 8, 10, 11, 12, 13, 14, 15, 16 and 18±0.3 V_{RMS} from 0.6±0.3 V_{RMS} for two unpackaged LVTs and one packaged LVT.

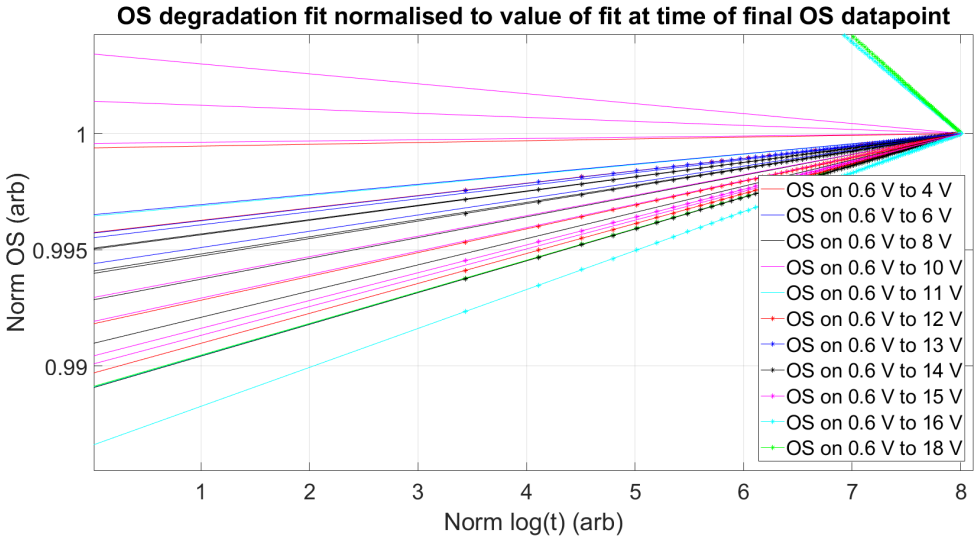

Figure 2.13: Normalised linear OS degradation fits for step increases in voltage to 4, 6, 8, 10, 11, 12, 13, 14, 15, 16 and 18±0.3 V_{RMS} from 0.6±0.3 V_{RMS} for an unpackaged LVT with end blocks

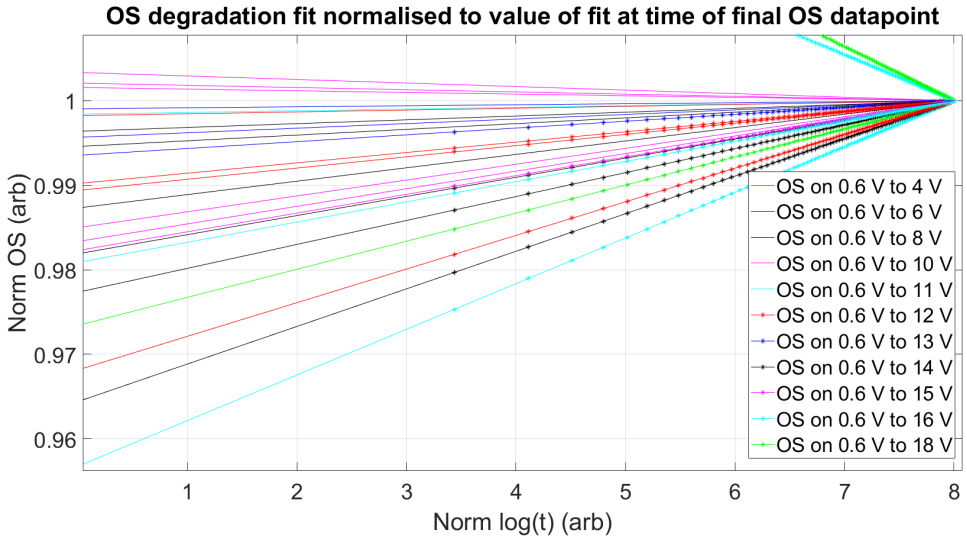

Figure 2.14: Normalised linear OS degradation fits for step increases in voltage to 4, 6, 8, 10, 11, 12, 13, 14, 15, 16 and 18±0.3 V_{RMS} from 0.6±0.3 V_{RMS} for a directly-bonded, unpackaged LVT

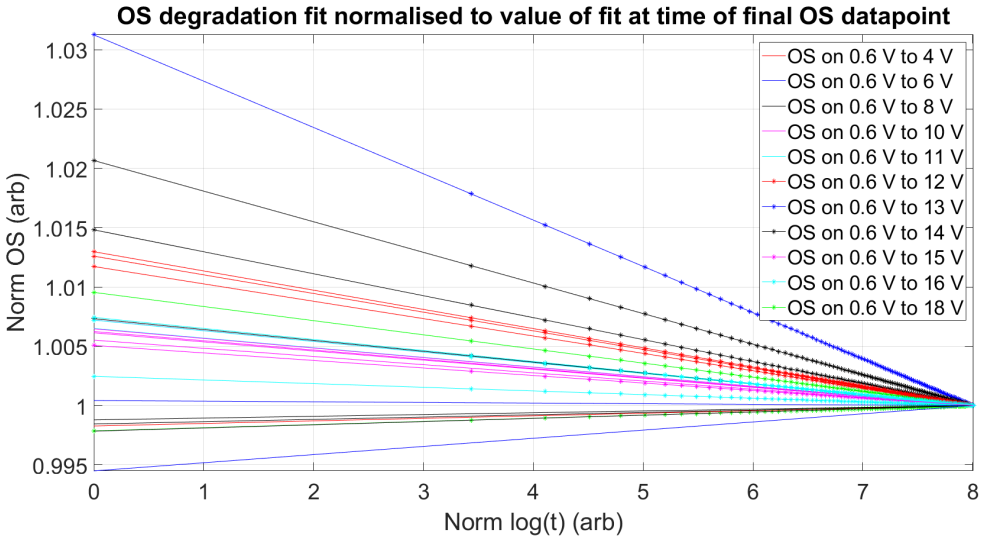

Figure 2.15: Normalised linear OS degradation fits for step increases in voltage to 4, 6, 8, 10, 11, 12, 13, 14, 15, 16 and 18±0.3 V_{RMS} from 0.6±0.3 V_{RMS} for a directly-bonded, unpackaged LVT

No clear dependency of the OS degradation rate on the magnitude of voltage step increase is observed.

2.9 Effect of DC voltage offset on LVT response

DC offsets due to faulty rectifiers can be a problem in the distribution network. The current sensors are not expected to see DC offsets as power is supplied via a transformer, however a voltage sensor fed by a resistive divider may encounter them. This section therefore looks at LVT performance under DC offsets of ±15 V.

Fig 2.16 shows mean reflected Bragg wavelength and corresponding OS for two packaged and two unpackaged LVTs, with the voltage sequence applied inset - the AC component is given as RMS. Also inset is a polarisation - electric field hysteresis loop displaying the region in which the the LVT operates at nominal voltage. If we apply a DC offset, it should have the effect of transforming the loop along the electric field axis. From the hysteresis

loop it can be seen that the mean wavelength should increase with positive applied field, and decrease with negative applied field. This is observed in the data. The corresponding change in OS can be predicted through considering the strain-electric field 'butterfly' hysteresis loop, and for a step increase in mean wavelength, a step decrease in OS is expected. Note that the shape of these loops is dependent on the temperature and electrical history. None of the sensors display this behaviour and each demonstrates different behaviour during the run considered. This may be due to the as yet unconfirmed electrical interference between sensors. Piezoelectric creep is evident in the mean wavelength plot. Subsequent to a fault on the electrical system under test, this could be compensated to improve temperature compensation.

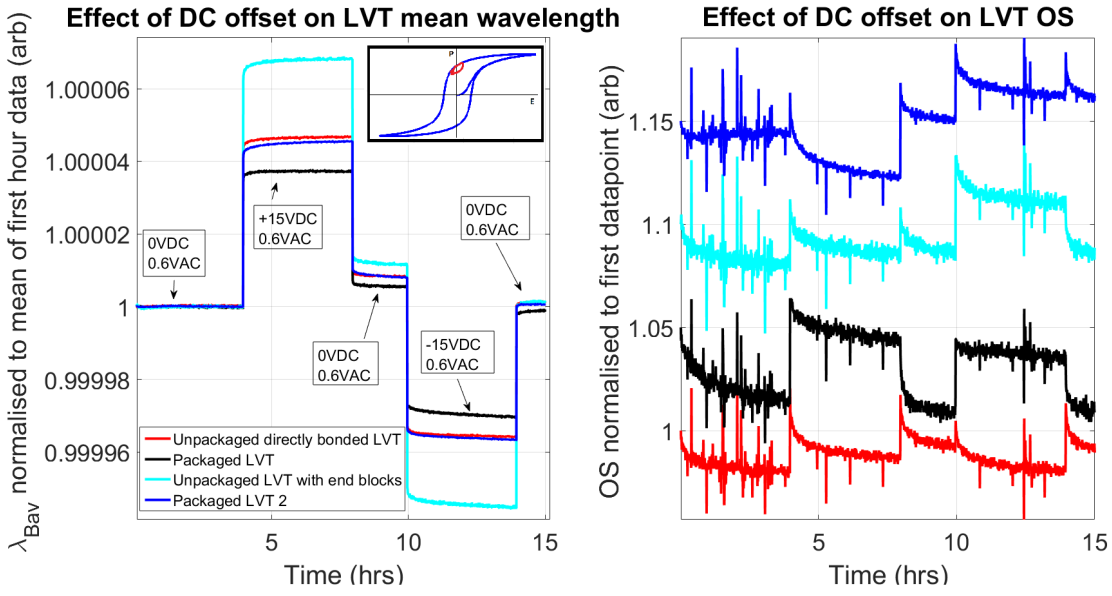

Figure 2.16: Left: Effect of DC offset on LVT mean reflected Bragg wavelength for four LVTs. Inset is a polarisation - electric field hysteresis loop displaying the approximate region in which the the LVT operates at nominal voltage. Right: Corresponding OS.

2.10 Characterisation of repeatability of normalised OS degradation curves

Fig 2.17, 2.18, 2.19 and 2.20 indicate the repeatability of OS degradation for an unpackaged LVT. This was investigated to determine the applicability of a one-size-fits-all ageing compensation code. Fig 2.17 shows a tending-towards-Gaussian distribution of individual B parameter percentage deviation from an average B parameter. From previous experiments, data with different run schedules (transient magnitude, voltage drop magnitude) was amassed. Mean B parameters for each run schedule were determined by fitting Eqn 2.3 to each degradation plot from measurements with the same run schedule, producing a mean line of best fit, then extracting the B parameter. From here, the percentage deviation of each individual degradation curves B parameter from its corresponding mean B parameter was determined.

Fig 2.18 uses the same dataset and shows the deviation of each fit two hr after subjection to a voltage transient in terms of a percentage of the OS of its corresponding average fit at $t = 30$ s. As the data in Fig 2.17 and 2.18 had a variety of different run schedules, Fig 2.19 and Fig 2.20 were produced to investigate the repeatability of the decay by the same measure for a single run schedule. Only ten runs were available for this study, but the charts indicate similar repeatability to Figures 2.17 and 2.18.

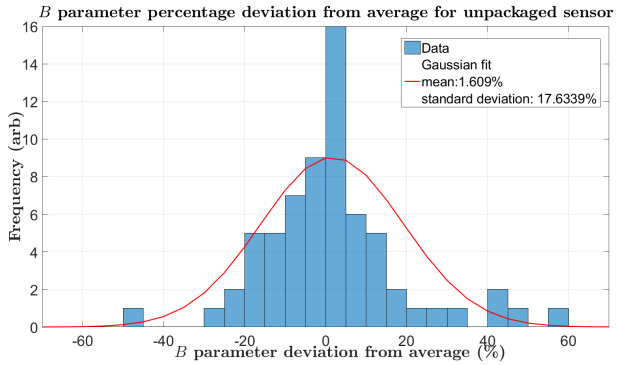

Figure 2.17: Repeatability of B parameter with Gaussian fit. 66 ageing decays were fit with Eqn 2.3. Fits with the same run schedule were grouped and mean average fits produced. The above chart shows the deviation of the B parameter for each fit as a percentage of the B parameter for its corresponding average fit.

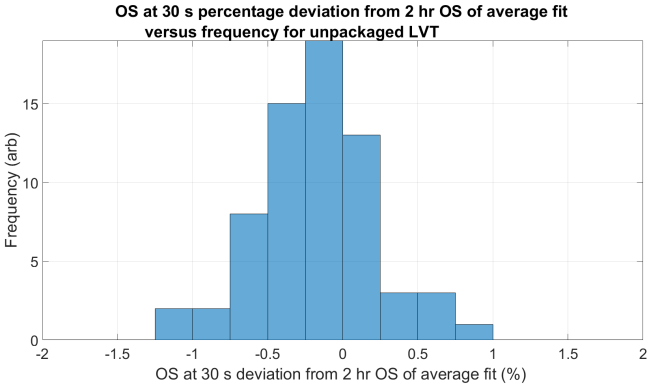

Figure 2.18: Repeatability of fit. 66 degradation curves were fitted with Eqn 2.3. Fits with the same run schedule were grouped and average fits produced. The above chart shows the deviation of each fit (as a percentage of the OS of the average fit at 2 hr) from its corresponding average fit at $t = 30$ s.

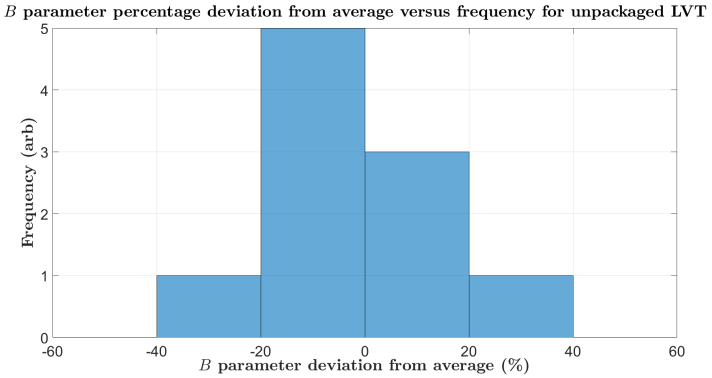

Figure 2.19: Repeatability of B parameter. Ten degradation curves were fit with Eqn 2.3. Data for each decay was recorded for 2 hr after initiation by a step down from 20.4±0.3 V_{RMS} to 0.6±0.3 V_{RMS}. An average fit was produced and the above chart shows the deviation of the B parameter for its average fit.

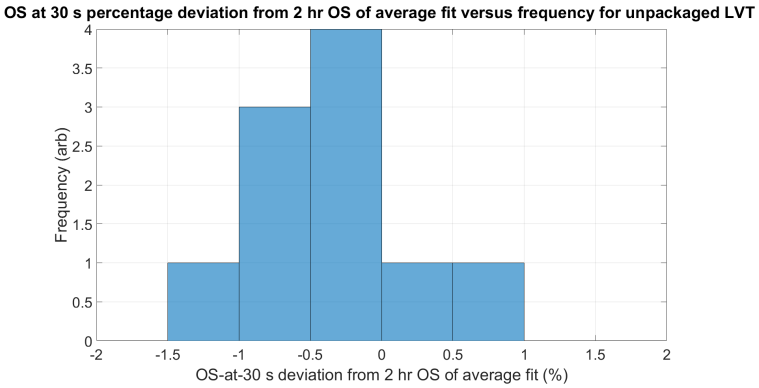

Figure 2.20: Repeatability of fit. Ten degradation curves were fit with Eqn 2.3. Data for each decay was recorded for 2 hr after initiation by a step down from 20.4±0.3 V_{RMS} to 0.6±0.3 V_{RMS}. An average fit was produced and the above chart shows the deviation of each fit (as a percentage of the OS of the average fit at 2 hr) from the average fit at t = 30 s.

There is an ongoing effort to compensate this effect in software. Early investigations indicate that a one-size-fits-all approach may be acceptable to achieve 5P30 accuracy requirements, subject to the magnitude of other errors. As seen in fig 2.18, the initial range of OS at 30 seconds deviation from the sensitivity after two hr of the average fit is ~1.25%.

In a one-size-fits all compensation procedure then, this would be the error due to compensation after two hr.

2.11 Effect of ageing of PS at 0 V on LVT accuracy upon return to nominal voltage

From a commercial perspective, it is likely that quality assurance testing will be performed on sensors before sale. This will inevitably involve cycling the sensors prior to a long period of inactivity, and leads to the question - how does piezoelectric ageing proceed in the absence of an external electric field across the terminals?, or similarly - how does the OS proceed upon return to nominal after a period of prolonged inactivity?

Tests were performed in which the sensors were subjected to a one minute AC 20.4±0.3 V_{RMS} pulse, then a two hour degradation period at 0.6±0.3 V_{RMS}, then a period of zero applied electric field[7], before a return to 0.6±0.3 V_{RMS}. Upon return to 0.6±0.3 V_{RMS}, an increase in OS is observed. This increase takes the form of Eqn 2.3. Results are shown for a single unpackaged LVT in Figs 2.21 and 2.22 and indicate that upon an increase in voltage, there is no critical voltage above which deageing is observed and below which ageing is observed.

In practice, the sensors will be transported and stored with their leads shorted to prevent charge build up due to mechanical shocks and the pyroelectric effect. Due to concerns that the sensors may be interfering with each other in the set-up, the tests were repeated with the PCI disconnected and the sensor terminals shorted during the periods of zero applied electric field periods. These tests are labelled as 'leads shorted' in Fig 2.22.

[7] electrodes not shorted

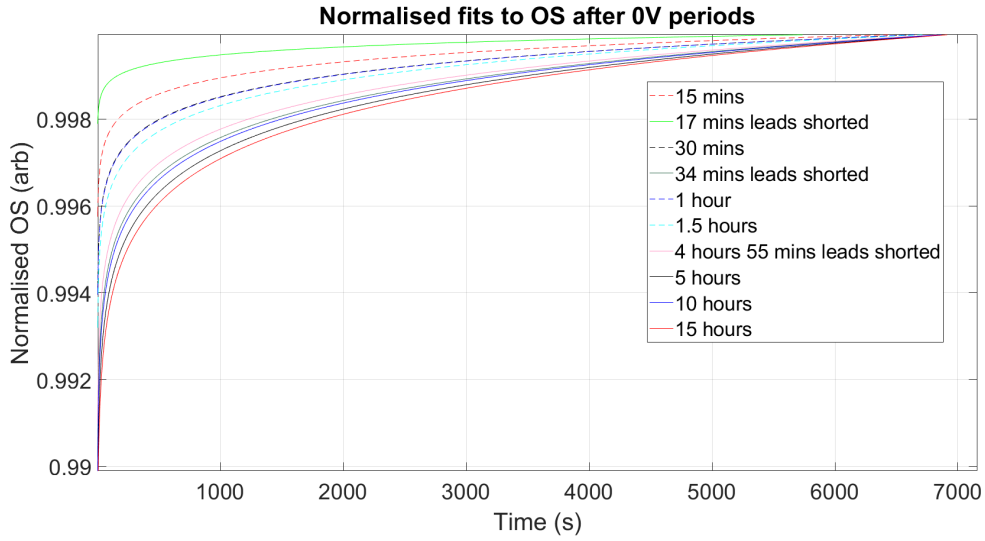

Figure 2.21: OS data normalised by value of fit at time of final OS data-point for an unpackaged LVT.

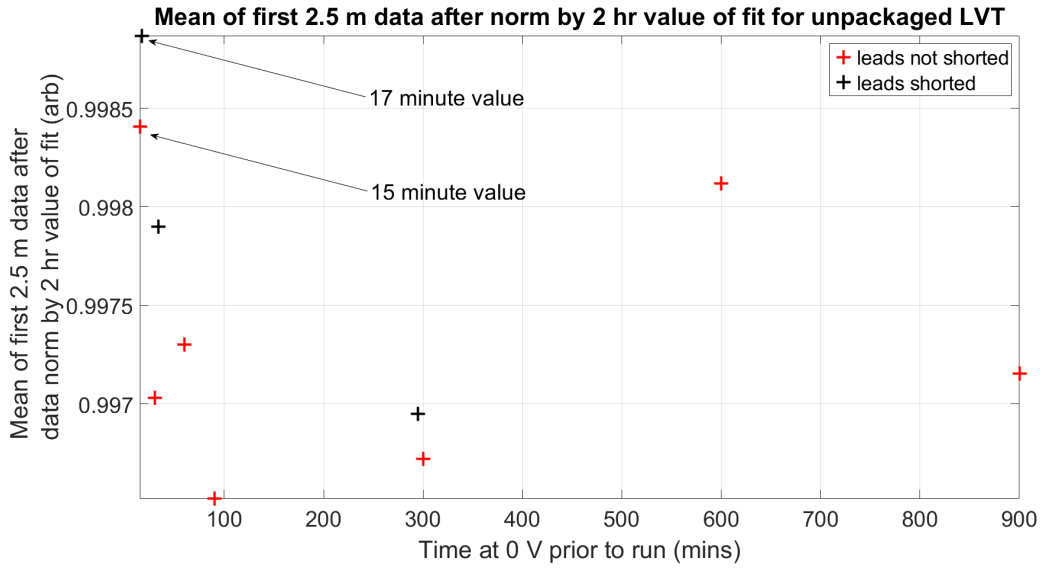

Figure 2.22: Mean of first 2.5 minutes of OS data normalised by 2 hour value of fit for an unpackaged LVT.

If it is assumed that the deageing curve has approximately the same PDF for parameter B as the ageing curve, then a Gaussian function, Eqn 2.4, should be expected.

$$\frac{1}{\sigma\sqrt{(2\pi)}}exp(-(\frac{x-\mu^2}{2\sigma})) \tag{2.4}$$

With mean μ and standard deviation σ. Taking those values from a Gaussian fit to the new unpackaged LVT ageing B distribution in Fig 2.17 the probability of getting a given B value with some percentage deviation from the mean can be calculated.

Looking at Fig 2.22, it is seen that if a correlation were to exist between B and duration at 0 V then upon conducting sufficient repeats, the 15 minutes initial normalised value would be expected to be above the 17 minutes value. The two values for 17 minutes and 15 minutes are 0.9974 and 0.9945 respectively, with centre point 0.996 between them. The B parameters for these curves are 2.9×10^{-4} and 6.2×10^{-4} respectively with a curve beginning on the centre point requiring a B parameter of 4.5×10^{-4}.

In order for these two data points to fit the trend, they are required to swap positions relative to one another. If the mean of the Gaussian distribution of B values for both points were at the midpoint, then this would require B corresponding to A=0.9945 to be 27% too high and B corresponding to 0.9974 to be 36% too low. Using a standard normal probability table in conjunction with the values μ and σ from above, it is concluded that the probability of B being within the range $B \pm 27\%$ is 85%. This estimate is on the low side, given the poor fitting of the Gaussian to the data.

This process needn't be repeated for the other anomalous value pair in the set; by observation of the discrepancy between the two values for 34 minutes and 1 hour it is very unlikely that this is a case of measuring unlikely values on the Gaussian distribution. Thus either the PDF for B is broader for the deageing curves when compared with that determined for the ageing curves, or there is another factor at play, as it is unlikely that these value have arisen from statistical variance.

2.12 Transient pulse duration impact on normalised degradation curve B parameter

The transient voltage dependence of the OS degradation curve was investigated for three LVTs; three packaged with end blocks and one unpackaged and directly bonded. The 28.8±0.4 V_{pk} pulse durations investigated were 10, 40, 80 ms. The voltage pulse was applied, followed by a 30 s period of 0V, then a period of 0.6±0.3 V_{RMS}. Figure 2.23 shows OS degradation fits for 10, 40, and 80 ms transients, normalised to the final OS value.

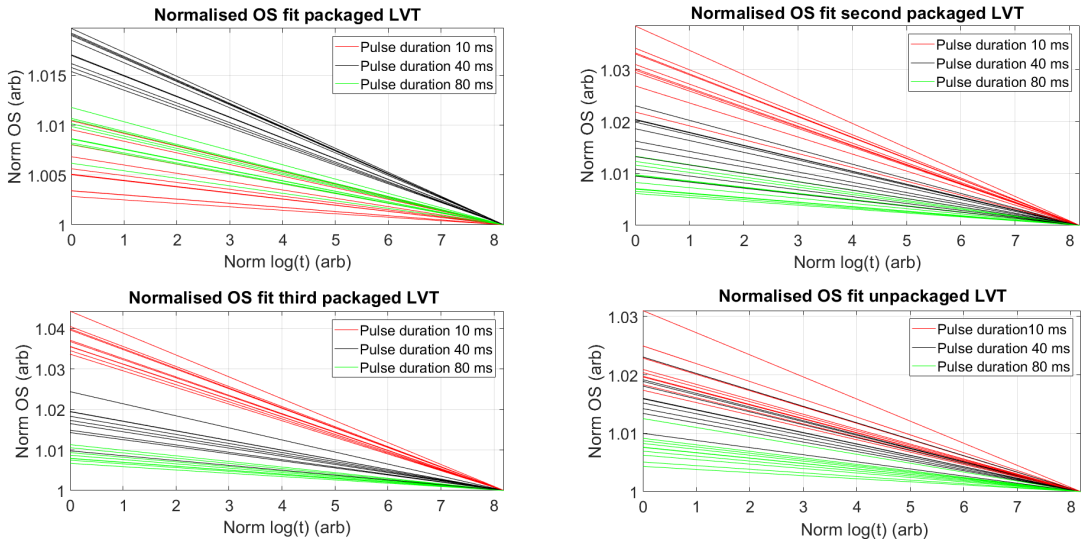

Figure 2.23: Average normalised OS degradation curves for 10, 40, 80 and 15000 ms transients for a packaged LVT

Note that the experiment was conducted such that on each run, bar the first, the PS had the same history over the previous two hr. The results may differ given varying immediate PS history. In Fig 2.23 a clear trend is apparent in each subplot, with two packaged LVTs and one unpackaged LVT showing an increasing B parameter due to a longer pulse duration. It is unclear why the other packaged LVT bucks the trend.

Assuming that OS degradation is due to piezoelectric ageing, a longer pulse duration would result in more deageing of the PS, and the B parameter would be expected to increase.

During operation, if the AC voltage across the stack is reduced, the OS falls to a level determined by the phase and magnitude of the voltage at the time of the voltage drop. The phase dependency occurs because the stacks remnant polarisation is higher when the voltage is reduced following a half period, compared to that when the voltage is reduced after a full period. The magnitude dependency is simply due to the fact that below the saturation polarisation, an increased voltage magnitude results in an increased remnant polarisation.

2.13 Change in LVT sensitivity dependent on magnitude and phase of voltage transient

The dependence of the ageing curve on the magnitude and phase of an applied voltage waveform was investigated for the LVTs. It was found that during piezoelectric ageing in the presence of fatigue, the LVTs change in OS, ΔOS, is directly proportional to the change in mean reflected Bragg wavelength, $\Delta\lambda_{\mathrm{Bav}}$, which is calculated using a moving window in the LabVIEW software.

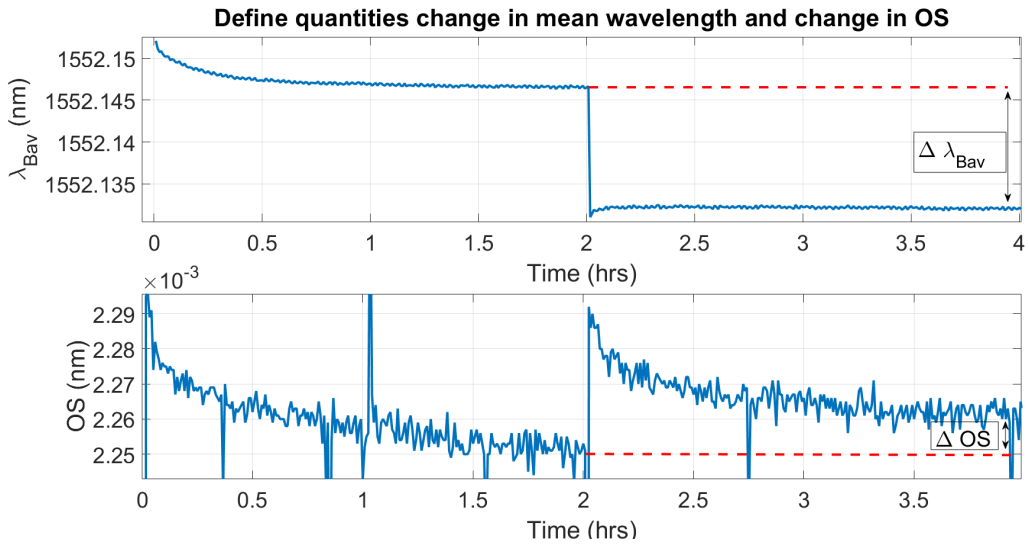

Figure 2.24: Quantities defined; $\Delta\lambda_{\text{Bav}}$ (top) and ΔOS (bottom). The run schedule is as follows; 28.8±0.4 V_{pk} for 10 ms, 0 V for 30 s, 0.6±0.3 V_{RMS} for 2 hr, 20.4±0.3 V_{RMS} for 20 ms, 0 V for 30 s, 0.6±0.3 V_{RMS} for 2 hr.

Fig 2.24 defines the quantities described and Fig 2.25 shows the percentage ΔOS versus $\Delta\lambda_{\text{Bav}}$ for four LVTs with linear fits to the data. This prompted Synaptec to propose a compensation algorithm using real time monitoring. In the proposed compensation scheme, the aforementioned relationship is accurately determined for the LVT under test. Upon the LVT being exposed to a voltage transient in the form of a grid fault, the reflected Bragg peak $\Delta\lambda_{\text{Bav}}$ is monitored and the OS compensated via the known linear relationship between $\Delta\lambda_{\text{Bav}}$ and ΔOS. This compensation method seems preferable to the one-size fits all method, if the signal processing time is sufficient.

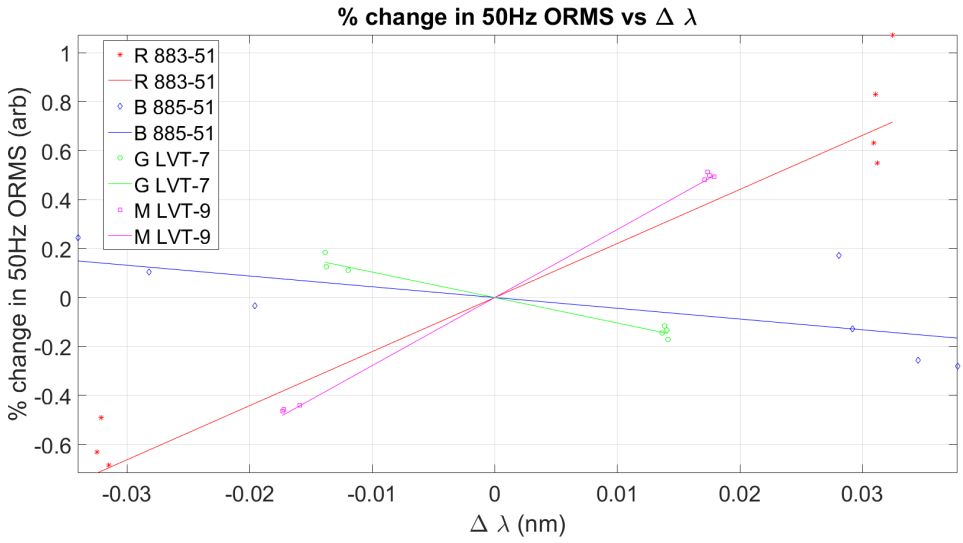

Figure 2.25: Linear relationship between percentage ΔOS and $\Delta\lambda_{\mathrm{Bav}}$ for four LVTs. Figure courtesy of Neil Gordon and Synaptec. The percentage change has been calculated as a percentage of the approximately settled OS after two hr following a 28.8±0.4 V_{pk} pulse.

In figs 2.24 and 2.25, the dominant contribution to $\Delta\lambda_{\mathrm{Bav}}$ is the step change, which occurs as the first 0.6±0.3 V_{RMS} period begins after a half cycle of 28.8±0.4 V_{pk}, whilst the second begins after a full cycle. The linear relationship is observed simply because the shape of the strain-electric field butterfly loop changes with change in remnant strain. This behaviour is seen in figure 2.25 for the LVTs labelled LVT-7 and LVT-9, and it is proposed that the relationship between the poling direction and electrode polarity of the LVTs labelled 883-51 and 885-51 is reversed relative to that of LVT-7 and LVT-9.

Also of interest, is the way in which the mean wavelength changes during the periods of $0.6 \pm 0.3 V_{RMS}$. The changes in λ_{Bav} and OS at constant AC voltage are denoted $\delta\lambda_{\mathrm{Bav}}$ and δOS to differentiate them from the quantities just described. The following hypothesis is proposed to explain the correlation between $\delta\lambda_{\mathrm{Bav}}$ and δOS. In this hypothesis δOS is again a direct consequence of the change in remnant polarisation of the PS. In the case of a DC step, the mean wavelength (in addition to the remnant polarisation and strain

of the PS) would subsequently increase logarithmically, and the effect would be termed creep. We now require that creep behaviour can occur in the presence of an AC signal, and that it is triggered upon a change in the magnitude of the PS polarisation above a threshold polarisation magnitude. Consider a voltage sequence comprising of a single cycle of 20 V_{RMS}, then a period of 1 V_{RMS}. The final quarter of the 20 V_{RMS} cycle consists of a step from -20 $\times\sqrt{2}V_{pk}$ to 0 V. This change initiates a creep behaviour which increases the mean wavelength throughout the period of 1 V_{RMS}.

Such behaviour was modelled and demonstrated to be in line with experimental evidence in donor doped PZT by Muliana [48]. A mean wavelength change corresponds to a PS remnant polarisation and strain change and this alters the shape of the strain-electric field butterfly loop. If the remnant strain of the PS is increased, then the OS is expected to decrease due a change in gradient of the strain-electric field butterfly loop, thus a logarithmically increasing mean wavelength should correspond to a decrease in OS proportional to the increase in mean wavelength. Fig 2.24 demonstrates this between two and four hr.

If this viscoelastic response behaves in the same way as that under DC conditions, its magnitude should be directly proportional to the initial displacement upon change in voltage as in 1.11. This would further benefit the accuracy of Synaptec's compensation procedure. Further work will test this hypothesis; note that the investigations into ageing dependency on magnitude of voltage step change detailed earlier in this chapter were performed on normalised ageing curves so would not reflect such a dependency.

It is unclear whether this change in remnant polarisation alone is of sufficient magnitude to describe the δOS seen, or whether ageing still has a part to play. Additionally, this model fails to satisfactorily explain the observed deageing so the ideas of ageing and deageing cannot yet be put aside. Further work could see the parameters in Muliana's model experimentally determined for the PIC 252 PZT used in the LVTs, and the behaviour of the model under conditions simulating those seen by the PS in the event of a fault on the electrical system under measurement, and under conditions in which deageing has been observed simulated. This would form the basis of a model for PS behaviour from

which a more comprehensive predictive tool incorporating DC creep, fatigue and deageing behaviour could be produced.

2.14 Investigation into sensor interference in parallel circuit

It was noticed that the sign of the constant of proportionality between $\Delta\lambda_{\mathrm{Bav}}$ and ΔOS of one unpackaged LVT changed on a run where the electrical polarity of two other sensors connected was reversed. This suggested that the LVTs may be interfering with one another in the present set-up.

Four LVTs were electrically connected in parallel with only one connected optically, and voltage sequences of 28.8±0.4 V_{pk} for 10 ms, 0 V for 30 s, 0.6±0.3 V_{RMS} for 2 hr, then 20.4±0.3 V_{RMS} for 20 ms, 0 V for 30 s, 0.6±0.3 V_{RMS} were run. The same relationship between ΔOS and $\Delta\lambda_{\mathrm{Bav}}$ was observed as that on a similar run conducted beforehand with the same four sensors connected optically and electrically. This suggests that the LVTs were not interfering optically.

Next, the polarities of all but the optically connected sensor were reversed. This again caused a change in sign of the gradient of $\Delta\lambda_{\mathrm{Bav}}$ with respect to ΔOS. Next, the same set-up and voltage sequence was used, with all but one sensor electrically disconnected. This produced no change in the $\Delta\lambda_{\mathrm{Bav}}$ - OS relation of the driven sensor, suggesting that optical interference was not the source of the problem.

All four sensors were optically and electrically reconnected and placed on separate foam pads of thickness 1 cm+ to isolate vibrations. Again, upon running voltage sequences of 28.8±0.4 V_{pk} for 10 ms, 0 V for 30 s, 0.6±0.3 V_{RMS} for 2 hr, then 20.4±0.3 V_{RMS} for 20 ms, 0 V for 30 s, 0.6±0.3 V_{RMS}, the sensors displayed no change in the $\Delta\lambda_{\mathrm{Bav}}$ - ΔOS relationship, indicating that mechanical interference was again not the source of the problem.

The interference then, is surely electrical in nature. To prevent the interference, the AST has obtained a circuit box containing six voltage follower buffer amplifiers in parallel,

to electrically isolate the LVTs from one another. Further work will remove the electrical interference effect and repeat the experiments performed in this report to ensure that results are free from such effects. If the effect is shown to remain, when the buffer amplifiers are in use, then the impact of history of applied voltage on it will require investigation.

2.15 Temperature characterisation of piezoelectric response

At present, the I-MON interrogator takes a temperature measurement once per run, then uses this reading to compensate data for the entire run. This means that the interrogator temperature must be well maintained, throughout the duration of any experiments. In addition to this, the temperature compensation of the piezoelectric hysteresis loops has been deemed insufficient at present. Comparison of LVT behaviour at different temperatures - such as temperature dependence of OS degradation curves - has been postponed until temperature compensation is improved.

2.16 Summary and further work

In this chapter, experimentally observed degradation of the OS in the LVTs was introduced. The degradation was initially thought of as ageing under fatigue conditions and as such the hypotheses predicting the results of the experiments are based on this assumption. An investigation into the possibility of an ageing - deageing transition was highlighted, but no such clear-cut transition has been found. The options regarding modification of ageing rate and compensation in software were presented and compensation was selected as the easiest choice with which to proceed. Experiments to determine the dependencies of parameters in Eqn 2.3 were highlighted and results discussed. In particular, the B parameter for the normalised decays was found to be independent of frequency of applied AC voltage, transient pulse duration and magnitude of voltage step decrease from a transient voltage. DC offset voltages were observed to produce piezoelectric creep, however the dependence of

the OS on DC offset voltages was observed to differ between LVTs in the same experiment, suggesting that an interference between sensors may be present.

The ageing decays repeatability was investigated for an unpackaged LVT, with the B parameter exhibiting an approximately Gaussian distribution. Finally, hypothetical LVT interference was investigated and proposed to be electrical in nature, and obstacles to accurate temperature characterisation were highlighted. The observed dependence of the sensitivity of the OS to the phase of a transient 5P30 fault waveform at the time of return to nominal voltage was highlighted and explained and the linear relationship between $\Delta\lambda_{\mathrm{Bav}}$ and ΔOS as seen in Fig 2.24 was discussed. Finally, the observed change in mean wavelength during change in OS at constant AC voltage does not appear to fit with the ageing explanation and appears to fit the viscoelastic creep-like behaviour seen in the model of Muliana [48], however this model appears to fall short of an explanation for the observed curves attributed to deageing.

Further work required to develop a better understanding of the LVT response to change in applied voltage may include:

1. An investigation into the effect of stack dimensions on ageing decay repeatability and reproducibility. The hypothesis presented in section 2.3.1 suggests that both may be improved with greater volume of piezoelectric material.

2. Testing of the electrical interference hypothesis through repeating the experiments in which interference was observed, after introduction of unity gain voltage amplifiers to the circuit.

3. If the introduction of voltage follower operational amplifiers to the test circuit does prove to remove the hypothetical interference effect, DC offset experiments can then be repeated to confirm or deny the presence of an interference effect producing poor reproducibility of LVT response in the results.

4. For ease of comparison between effects going forward, future work might involve

building a program to simulate the expected behaviour under a given run, informed by the model of Muliana, experimental results, and the effects of fatigue, creep, ageing and deageing.

5. The effect of temperature on LVT response to a change in applied voltage should be quantified in the range -5 to 40 °C corresponding to the temperature range within which accuracy limits are specified in the relevant technical standard.

6. Following a fault on the electrical system under a test, and subsequent energisation of a current transformer (CT), transformer inrush occurs, in which the magnetisation of the CT core saturates, causing a decaying current up to five times higher than rated current to be drawn for several minutes [87]. This has not been accounted for in the experiments described, however, it would result in a second period of high voltage following closing of circuit breakers. Further tests and compensation procedures should account for this.

7. Experiments in which frequency was the independent variable could be repeated whilst monitoring piezoelectric stack surface temperature to determine the magnitude of self heating of the stack, and thereby gain insight into whether this is a factor in the frequency dependence of the observed OS degradation.

Chapter 3

Accelerated fatigue testing of two unpackaged LVTs

Accelerated lifetime testing at 10 kHz for $\mathbf{35 \times 10^9}$ cycles was performed on two unpackaged low voltage transducers (LVTs) whose construction comprised piezoelectric transducers connected to FBGs. Two bonding methods were compared - in one LVT, the FBG was bonded directly to the PS (piezoelectric stack) whilst in the other, alumina end blocks were bonded to either end of the stack and the FBG bonded to these and suspended above the stack. Tests were run at constant temperature and reflected peak Bragg wavelength measurements taken during 50 Hz intervals.

3.1 Introduction

Accelerated life testing is the term used to describe experiments which increase the degradation rate of the device under test. The LVTs are expected to experience a reduction in OS over time due to piezoelectric and mechanical fatigue. The purpose of this experiment was to differentiate between two sensor builds, based on their mechanical epoxy fatigue life, to select a design to take forward.

Broughton et al [88] performed cyclic mechanical fatigue tests of epoxies up to 10^7 cycles using a sinusoidal loading waveform. Based on this work, catastrophic failure is expected to occur at the interface between epoxy and PS, if at all, and without crack growth prior to failure.

Sherrit et al [89] studied fatigue of piezoelectric actuators of the same material as is used in the present application (PIC252), but with different dimensions. They reported a 7% degradation in impedance amplitude after 10^9 voltage cycles, attributing 3-5% to variation in average temperature during the tests. It is an assumption of this experiment that both sensors should experience approximately identical piezoelectric fatigue, despite the difference in length and statistical variance. Sherrit et al [89] noted that the fatigue takes the form of Eqn 2.3.

In addition to piezoelectric fatigue, the piezoelectric sensitivity degradation mechanism described in the previous chapter is present. Whilst piezoelectric fatigue is attributed to micro-cracking of the electrodes, ageing is thought to be caused by diffusive domain wall pinning by defects.

3.1.1 Effect of bond length on reproducibility and strain transfer

Wan et al [90] investigated strain transfer between bare fibre to a substrate via epoxy. Assuming that their results are valid for the epoxy used in the present application, given a 9 mm PS (bond length), a strain transfer coefficient of ~10%, rising to ~20% is expected for an 18 mm stack, and ~50% for a 36 mm stack. The presently used package has width ~18 mm, therefore longer stacks would however, require larger and presumably more costly packages. Her and Tsai [91] also investigated strain transfer through directly-bonded fibre, coating, adhesive and far-field-strained host using finite element analysis. Their results suggest that increasing the bond length should lead to improved reproducibility of strain transfer if the FBG is imperfectly aligned. It can also be seen that the strain distribution across the FBG increases with decreasing bond length - this must act to narrow the reflected Bragg peak from the FBG and a shorter FBG would further narrow this.

3.2 LVT builds

A rudimentary jig for building sensors was assembled. An aluminium block with a tight-fit groove for holding the PS against the end-blocks during curing and very thin grooves for holding the fibre in place upon the stack was used to secure the sensor in place. The end-blocks were first epoxied to the PS with Epotek epoxy 301 and left to cure at room temperature for one day with the assembly sat in the jig. The next step was to bond the fibre to the end-blocks. Acrylate coated fibre was temporarily spliced to the polyimide coated FBG, as this was easier to clamp than the polyimide-coated fibre due to its having larger diameter. An aluminium platform provided elevation so that plenty of fibre could be spliced onto the FBG. Aluminium blocks with smooth curved edges to prevent fibre damage were used to suspend a weight from the fibre for pre-tensioning, and a clamp was used to hold the fibre in place at the other end. The set-up was placed in an oven with a grill, with the weight suspended below the grill. Fig 3.1 (left) shows a schematic of the set-up, and (right) shows a photograph of the aluminium fibre guide, platform, sensor holder and weight attached to nut and bolt.

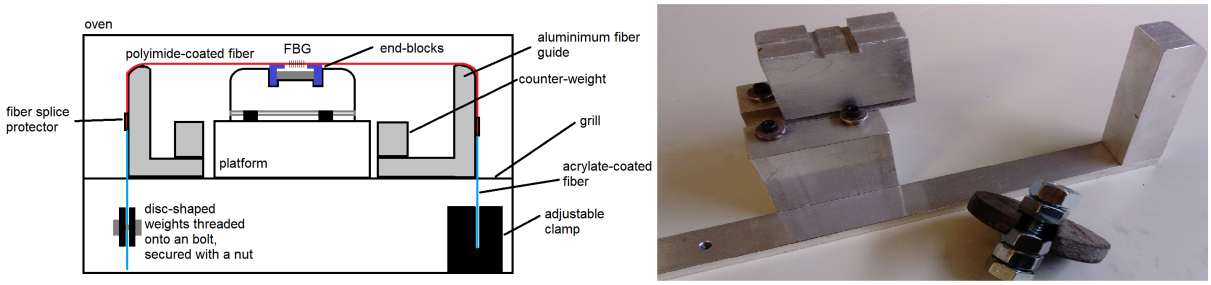

Figure 3.1: Left: schematic of fibre-tensioning set-up. Right: aluminium fibre guide, platform, sensor holder and weight attached to nut and bolt.

The bolt was tightened such that the fibre was squeezed against the weight, securing it in place. On completion of the curing process, the clamped fibre ends were cut off at the polyimide side of the splices and the fibre was connectorised with acrylate-coated pigtails

having angle polished fiber connectors.

The following lessons were learned in building sensors:

- When bonding an FBG directly to a PS with Epotek Epoxy 301, the ink used to mark the FBG position on the fibre is soluble in the un-cured epoxy.
- A screw mechanism for holding the PS in place during stack - end block curing should be used as the tight fitting solid block made it difficult to extract the sensor post - cure.

Two sensors were assembled, one consisting of an FBG directly epoxied along the full length of a brand new PICMA p883-51 PS ($3 \times 3 \times 18$ mm) and another with the fibre epoxied to $3 \times 4 \times 4$ mm alumina end blocks with grooves suspended above a shorter brand new PICMA p883-11 PS ($3 \times 3 \times 9$ mm). Epotek Epoxy 353ND cured at 100 ° C for one hour was used for the sensor possessing end blocks whilst Epotek Epoxy 301 cured at room temperature for 24 hr was used for the directly-bonded sensor. No fibre pretension was applied to the directly-bonded sensor whilst a 250 g weight was used to pretension the sensor with end blocks. In both cases a 7 mm FBG coated with 140 µm HD Microsystems PI 2525 polyimide was used. Henceforth, the directly-bonded sensor will be referred to as sensor A and the sensor with end blocks as sensor B.

Bonding surfaces were cleaned with isopropanol, which was allowed time to evaporate, before application of epoxy. Additionally, reasonable care was taken to ensure that the width of the epoxy applied orthogonal to the fibre axis and the epoxy thickness between the bonded substrates were minimised and equal on both sensors. This was done by inspection only, by slowly incrementally adding the mixed epoxy to the substrate by hand using a narrow-headed firm cotton swab.

3.3 Method

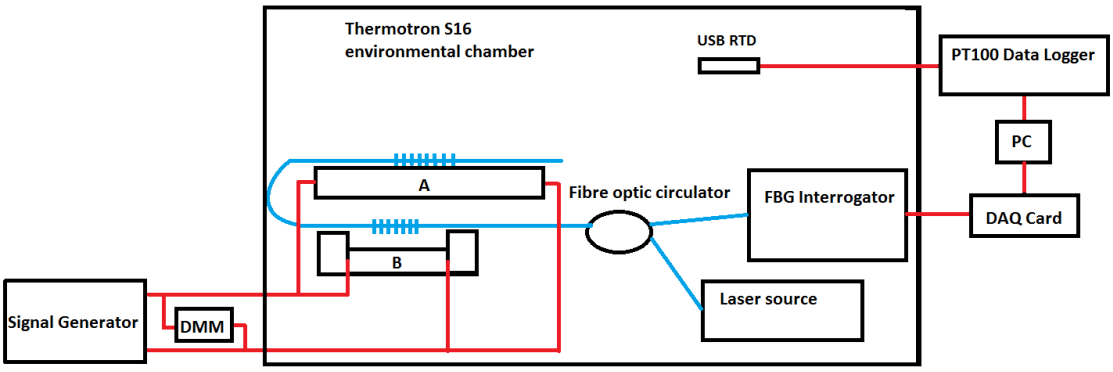

Figure 3.2: Experimental set-up.

The sensors were electrically connected in parallel and supplied a 2 V_{pkpk} voltage at 10 kHz by a signal generator. This frequency is well below the resonant frequency of both stacks which are quoted by the manufacturer [47] as 70 kHz and 135 kHz for the PICMA p883-51 and PICMA p883-11 PS respectively. Also connected in parallel to the signal generator was a Keysight 34410A multimeter from which the voltage across the stacks was read. A broadband light source was connected to a circulator with single mode fibre (SMF) which was in turn connected with SMF to the two sensors in series and an IMON-256 FBG interrogator. At intervals, the frequency was switched to 50 Hz and measurements manually initiated to accommodate the 2 kHz interrogator sampling rate, and at intervals of 30 s measurements were taken of the 50 Hz component of the reflected Bragg wavelength peak λ_B obtained by FFT, and λ_{Bav} . Peak detection was performed using a centroid algorithm. The sensors, optical source and interrogator were sealed inside a Thermotron S-16 environmental chamber at approximately the same height from the chamber floor to maintain constant temperature and relative humidity. The chamber temperature was monitored using a PT100 USB RTD (resistance temperature detector) and Omega PT-04A data acquisition module with $\pm 0.01°$ accuracy connected to the interrogator with

thermal grease to maximise thermal conductivity at the interrogator - RTD interface. The experiment was run for 35×10^9 cycles or 22 equivalent years (EY) at 50 Hz. Fig 3.2 shows the experimental set-up.

3.4 Results

Fig 3.3 shows the normalised temperature compensated λ_{Bav} average over 20-25 minute values versus EY 50 Hz for sensors A and B respectively. Each point is an average of the value between 20 and 25 minutes to average out fluctuations in signal generator output.

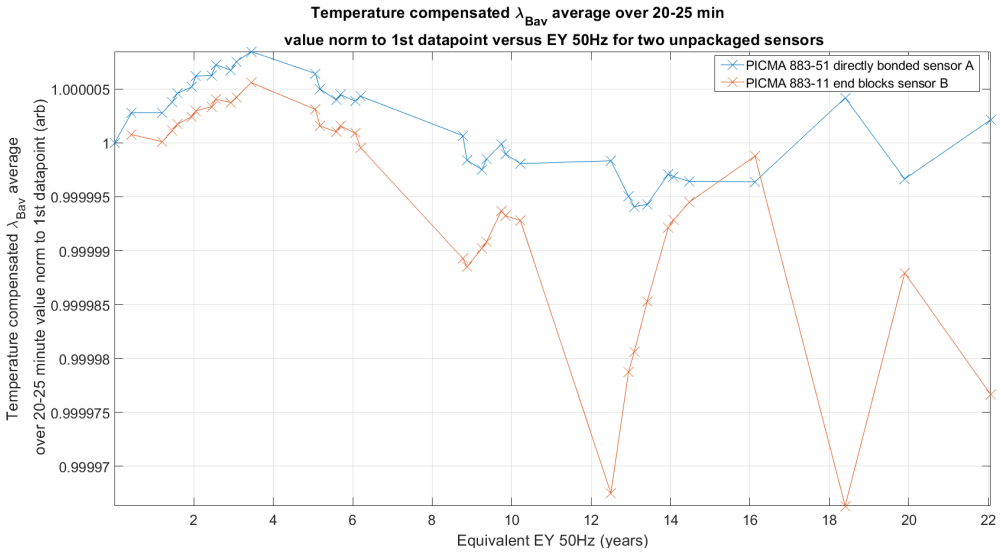

Figure 3.3: Normalised temperature compensated mean wavelength average over 20-25 minute values versus EY 50 Hz for both sensors.

Fig 3.4 shows mean chamber temperature between 20 and 25 mins of 50 Hz periods versus EY 50 Hz. In order to compare fatigue behaviour between sensors, the ratio of the two signals is plotted against EY 50 Hz is also plotted in Fig 3.4. This should normalise out effects affecting both sensors equally, such as the thermal sensitivity component related to the fibres thermo-optic coefficient, if it is assumed that this is constant. This signal still

contains a component due to the variation in the effective coefficient of thermal expansion between the two sensors.

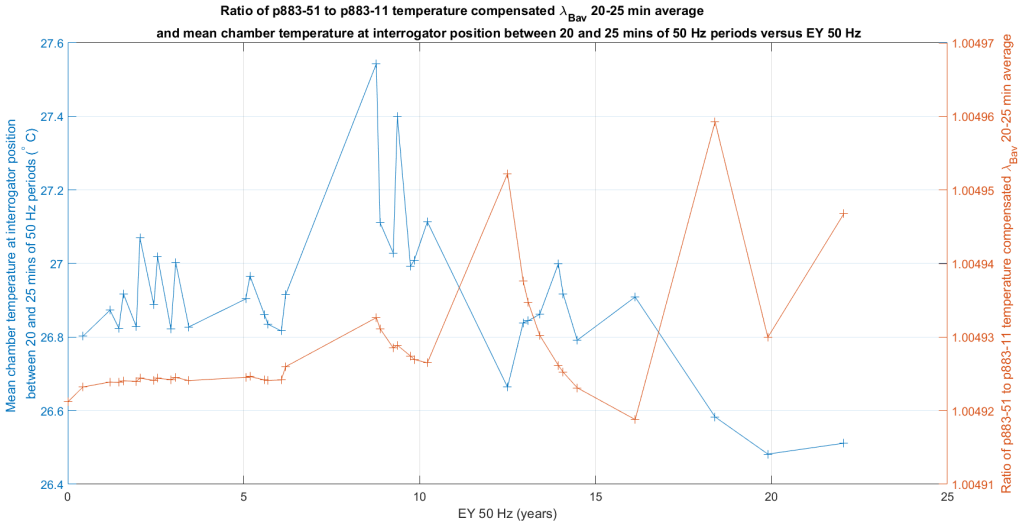

Figure 3.4: Mean chamber temperature at interrogator position between 20 and 25 mins of 50 Hz sections and ratio of mean wavelength of sensor B to sensor A between 20 and 25 minutes versus EY 50Hz.

Both sensors appear to show a burn-in period in which the OS increases over approximately three EY 50 Hz followed by a decay taking the form of Eqn 2.3.

Temperature induced Bragg wavelength shift, OS reduction due to piezoelectric degradation of Chapter 2 and signal generator voltage drift were crudely compensated for in the normalised plots of each sensor. Temperature induced Bragg wavelength shift was removed using Eqn 3.1, determined by Niewczas et al [12] for a 1550 nm FBG in the temperature range 25-40 ° C.

$$\lambda_{Bav} = 0.0106T + 1545.3 \tag{3.1}$$

OS reduction due to the piezoelectric degradation of Chapter 2 was removed using a one-size-fits-all compensation code, which produced a fit of OS to Eqn 2.3, normalised

the fit to its value after two hr, then normalised the original OS by the resultant curve. Voltage drift was compensated for through normalisation of OS by the voltage measured on the multimeter. As the voltage was saving incorrectly prior to 6.19 EY 50 Hz, three curves have been plotted in figures 3.5 and 3.6. One curve corresponds to the curve with optical signals recorded prior to 6.19 EY 50 Hz normalised by the mean voltage across later measurement periods, another normalised by the maximum voltage recorded during these periods and another normalised by the minimum voltage recorded during these periods.

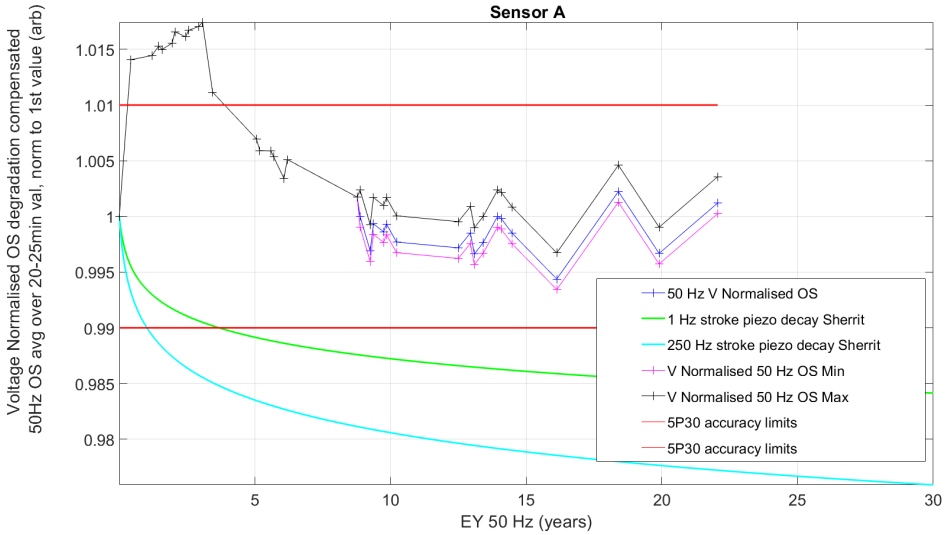

Figure 3.5: Directly-bonded stack, voltage normalised, ageing compensated OS mean over 20-25 minutes, normalised to first value, with 5P30 accuracy requirements and piezoelectric fatigue data from [89] overlayed.

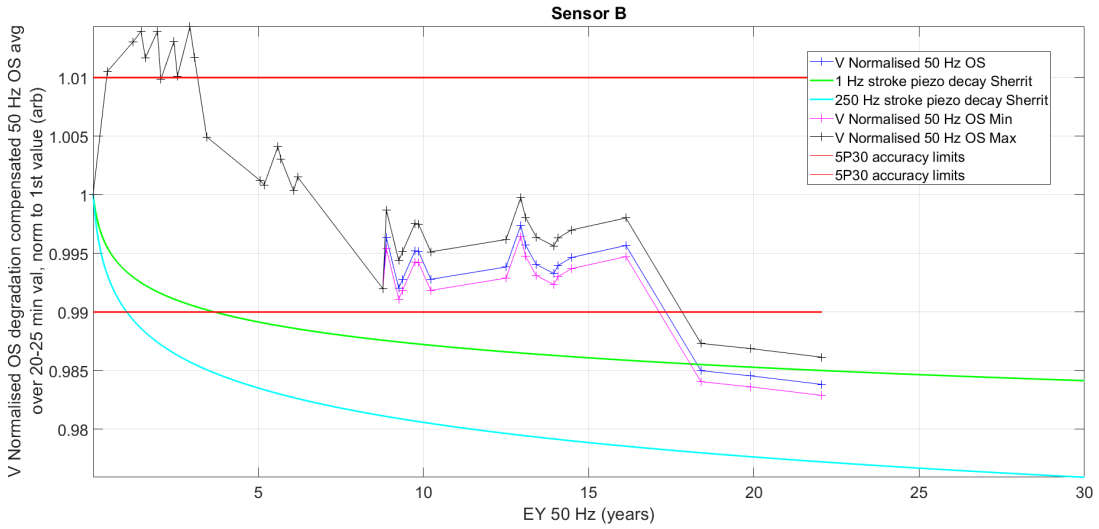

Figure 3.6: Directly-bonded stack, voltage normalised, ageing compensated OS mean over 20-25 minutes, normalised to first value, with 5P30 accuracy requirements and piezoelectric fatigue data from [89] overlayed.

Fig 3.7 displays the ratio of sensor A to sensor B OS 20-25 min mean versus EY 50 Hz.

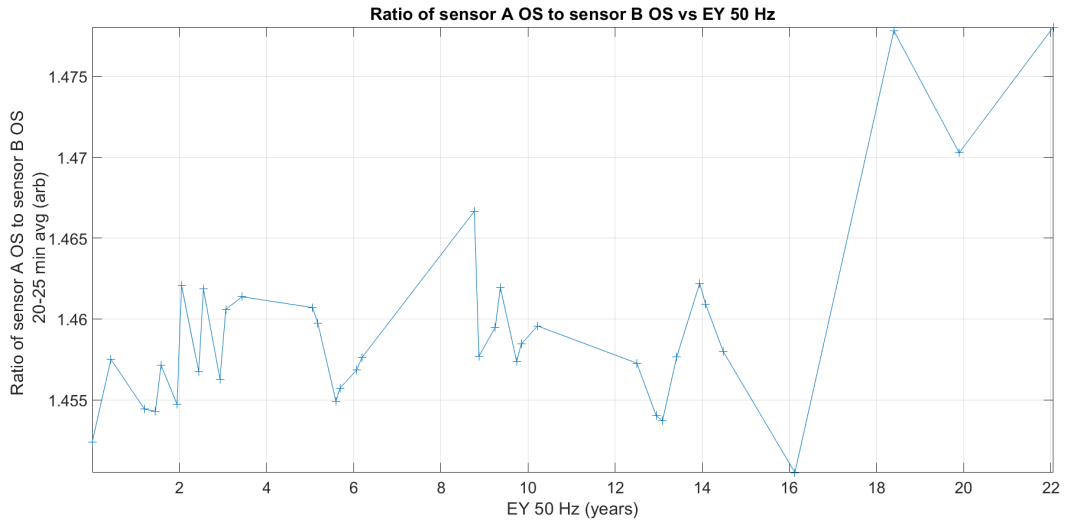

Figure 3.7: Ratio of sensor A OS to sensor B OS 20-25 min mean versus EY 50 Hz.

Fig 3.8 shows normalised decay curves with A values in legend from Eqn 2.3:

- Sensor A voltage normalised curve with min voltage normalisation up to 6.19 years.
- Sensor B normalised curve with min voltage normalisation up to 6.19 years.
- Sensor A voltage normalised curve with max voltage normalisation up to 6.19 years.
- Sensor B normalised curve with max voltage normalisation up to 6.19 years.
- Sensor A normalised curve with mean voltage normalisation up to 6.19 years.
- Sensor B normalised curve with mean voltage normalisation up to 6.19 years.
- Piezoelectric decay curves from [89] (NASA 250 Hz and 1 Hz)
- Average of fits to 16 OS degradation curves.
- 5P20 accuracy limits for protection class CTs.

The ageing decay fit was produced using 16 ageing decays curves on an unpackaged sensor of the same build as sensor B. For each of the 16 runs OS data was recorded for 2 hr after ageing decay initiation by a step down from a 20.4 V_{RMS} pulse to 0.6 V_{RMS}. Each decay was fit using Eqn 2.3 and a mean curve taken from the 16 individual fits. This is ageing in the presence of fatigue as the sensor was undergoing cycling during the test.

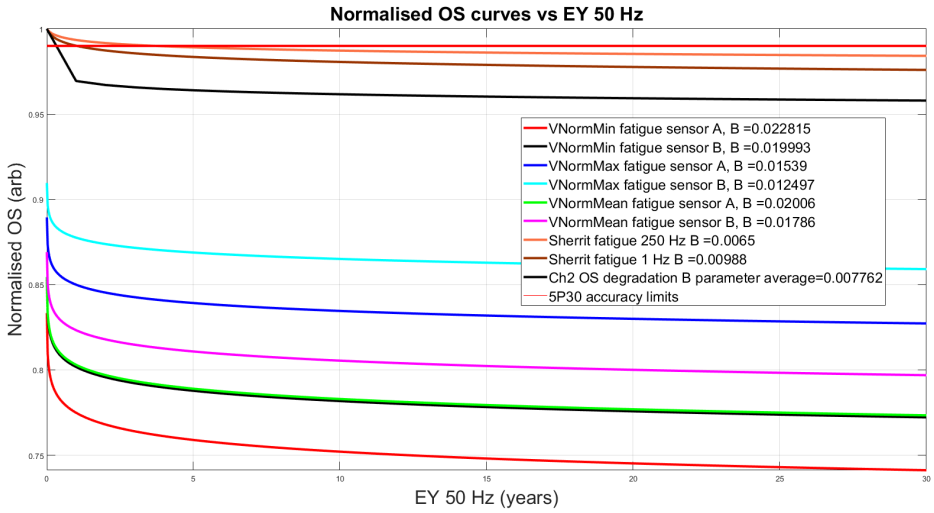

Figure 3.8: Normalised decay curves with B values in legend from Eqn 2.3.

3.5 Discussion

The apparent burn-in period could be due to an oxidation process on the electrodes (CuNi/Au/Ag) of the PS brought on by the increase in temperature through Joule heating. The oxygen for this process would have to diffuse through the hermetic encapsulant or could come from oxygen diffusion from the PZT itself. If this were the case, upon repoling the stacks, and subsequent continuation of the fatigue test, then the effect should not be seen again.

Alternatively, the burn-in period could be a period over which not-quite-cured epoxy cures and shrinks in the process. The most likely section of the epoxy to have not cured properly would be that between fibre and PS at the centre of the FBG. In sensor A, the shrinkage accompanying curing might increase the tension on the FBG as the epoxy connected to the FBG is pulled towards the centre of the FBG. Meanwhile, in sensor B, any late epoxy curing would produce increased tension in the fibre between the end blocks and the stiffening of the epoxy would afford better strain transfer, again increasing both OS and λ_{Bav}. This hypothesis would explain the difference between the two sensors mean wavelength behaviour, as the longer stack would see greater shrinkage, due to the longer length of late-curing epoxy and due the better strain transfer presumably afforded by directly bonding. It seems unlikely that both epoxies would be not fully cured, and require roughly the same amount of time to cure.

Most likely, the burn in period was not a burn in period at all and was due to deageing of the PS. Upon changing from 10 kHz to 50 Hz, the signal generator voltage output would increase and require re-adjustment to the correct level. Thus, the ageing process was altered at the onset of some 50 Hz periods due to on some measurements, changing frequency before voltage and on others changing voltage before frequency. This could have been avoided, however, during the experiment it was thought unimportant as the effect of ageing could be compensated in post-processing, but this has not worked as planned. Each 50 Hz section up to and including 2.93 years and then one 50 Hz section at 18.40 years exhibits OS degradation upon a voltage transient due to the frequency being changed before the voltage, whilst all other sections should have experienced a voltage dip due to the frequency being changed after the voltage. Upon returning to 10 kHz the frequency was always changed before the voltage correction.

In order to rule out both late epoxy curing and electrode oxidation as the process responsible for the 'burn-in' period, the fatigue test could be continued after sample repoling as in [89]. If in the absence of ageing i.e if voltage was reduced prior to frequency reduction, the burn-in period is not seen, and if after further repoling, in the presence of ageing, the

burn in period was seen, then it could be confirmed that the burn in period was in fact due to ageing.

Between 2.93 and 3.07 EY 50 Hz the signal generator was switched off for an unknown period of time up to six hr introducing an uncertainty of 50 equivalent days 50 Hz to the presented EY 50 Hz data. This should have triggered an OS degradation curve at 0V, then a deageing process upon returning to 50 Hz, though this deageing process is not apparent in the data. The chamber was switched off for 5 minutes 50 Hz at 5.18 EY 50 Hz and for 14 minutes 50 Hz at 6.07 EY 50 Hz - this might have resulted in a small change of temperature set point.

Each sensors change in OS and change in λ_{Bav} with respect to temperature over a temperature range of 20-30 ° C could have been characterised in the environmental chamber to more accurately compensate the effect of temperature on the ratio of the two sensors mean wavelengths. Note that on the final measurement, the OS increases for sensor A, whilst it decreases for sensor B. Finally, the two sensors should have had the same fibre pretension, epoxy material and stack length, such that the effects of the FBG attachment method could be singled out.

3.6 Further work

A refined accelerated life-time test should use an interferometer to measure piezoelectric displacement so that it can be separated from fatigue of other components, should include a statistically valid number of sensors under test with a control, and the sensors should be kept at constant temperature throughout. The sensors used should be built using the same batch of epoxy to minimise unintended variability in the tests. To minimise disruption due to power outages, a backup generator could be used, given the prolonged duration of the tests.

The change in voltage with frequency is thought to have been due to a combination of a capacitor at the output stage of the signal generator to prevent the passing of DC

signals and the capacitance of the piezoelectric stacks. The output impedance of the signal generator could be read from the data-sheet, or determined through measuring the voltage across a resistor connected across the signal generator output terminals at various frequencies. An intermediate circuit between signal generator and piezoelectric stacks could then be used to match impedances, such that the total impedance becomes purely resistive and the applied voltage becomes frequency independent.

Concrete is strong under compression but relatively weak under tension. It is therefore often reinforced through the insertion of steel rebars to which the tensile stresses are transferred. Analogously, the piezoelectric material is weak to the accelerations experienced by charge within it when a voltage is applied across it. Such accelerations are liable to damage the piezoelectric structure if not properly counteracted [92]. For this reason 'pre-loading' can be used to achieve the same effect as the re-bars in reinforced concrete, in which a counter-stress is applied to the stack to compensate such accelerations. Future accelerated lifetime tests should more carefully consider whether a pre-loading device would help to produce results more representative of conditions in the field.

Temperature compensation of OS is difficult due to thermal hysteresis of the piezoelectric constant. Instead of improving compensation, therefore, the temperature stability should be improved. In a repeat test, the sensors should be held in a smaller temperature chamber, to improve thermal stability, and additionally housed within an insulating structure, made of polystyrene, for example, to further improve temperature stability. Chamber temperature is known to correlate with room temperature, so the chamber should further be housed within a room in which temperature is stable 24 hours per day. To remove the influence of humidity, all sensors under test should be hermetically sealed in thermally insensitive packages in an inert atmosphere.

The FBG interrogator and light source should further be characterised. This should include quantifying light source optical power output stability with time, and degree of polarisation. The repeatability of image sensor response for a given optical power input should also be quantified, as should the image sensors sensitivity to the polarisation of

incoming light. Further, the stability of optical cavities depths within the interrogator optics, in the face of changing environmental conditions, could lead to changing interference patterns at the image sensor, and hence changing image sensor response. This could be experimentally quantified. Pixel response non-uniformity of individual pixels in the image sensor could also be characterised, as should the sensitivity of the centroid algorithm to the wavelength of incoming light. Knowledge and minimisation through informed choice of measurement apparatus of all these factors would improve- or at least improve the estimate of- measurement accuracy.

3.7 Conclusion

To conclude, both sensor builds survived the full 20 EY 50 Hz duration of the fatigue test without catastrophic failure. Sensor B showed the greatest reduction in sensor accuracy from the start of the test, but this is inconclusive as test parameters should have been better controlled, or characterised. It is suggested to characterise the measurement sensitivity to various accuracy influencing effects, hermetically seal the LVTs, improve thermal stability, and redesign the electrical circuit to achieve voltage stability. The experiment could have been better designed such that the two sensors had fewer factors variable between them. It is suggested that in a repeat test, the two sensors should have the same fibre pretension, epoxy material and stack length, such that the effects of the FBG attachment method could be singled out.

Chapter 4

Design review of prototype LVT protection circuit

4.1 Introduction

This work was carried out in collaboration with Synaptec. It investigates the options regarding transient voltage suppression, and delivers a refined design of the low voltage transducer (LVT) protection circuitry, taking into account critical constraints including; the LVT maximum voltage withstand, TVS (transient voltage suppression) diode characteristics, accuracy standards pertaining to phase and amplitude errors, and resistor current and power ratings. It examines the errors due to the inherent RC filter in the LVT device formed by the capacitive PS and current limiting resistor (CLR) combination, and recommends a more optimal circuit design.

4.2 Transient voltage suppression device selection

4.2.1 Introduction and motivation

Fig 4.1 shows the present LVT protection circuit. There are two protection devices up for consideration; the TVS diode and the TRIAC. Section 4.3 introduces these devices and

their relevant parameters.

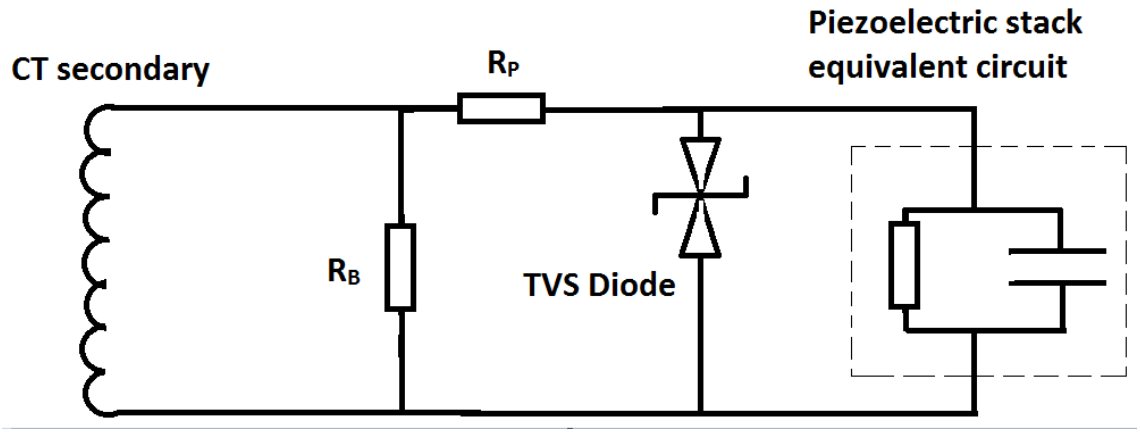

Figure 4.1: Present LVT protection circuit comprising burden resistor R_{B}, current limiting (protection) resistor R_{P}, a bidirectional TVS diode, and the PS (piezoelectric stack).

Transil P6KE22CA, P6KE24CA, P6KE27CA and P6KE30CA and Littelfuse SMCJ24CA bidirectional transient TVS diodes were tested for suitability when placed in parallel with piezoelectric LVTs. A single ON Semiconductor BTA30-800CW3G TRIAC was tested for comparison with the TVS data. Reproducibility was investigated for Transil diodes P6KE24CA, P6KE27CA and P6KE30CA.

Current was determined via Ohm's law across a 10 Ω Vishay LTO 30 CLR in series with the TVS diode, whilst voltage was measured directly across the TVS diode terminals. V_{IN} was measured using a Chroma 61512 programmable AC source with Chroma Soft Panel software. V_{IN} and the voltage across the diode V_{TVS} were measured using a GW INSTEK GDS-1042 oscilloscope with 10X probes. For the Littelfuse diodes, a Lecroy Waverunner oscilloscope with 10X probes was used instead, in an effort to reduce the voltage measurement uncertainty. The CLR resistance was measured prior to each experiment using a Keysight DMM 34410A 6 $\frac{1}{2}$ digit and recorded at regular intervals to check for divergence.

Intervals of 2 $\mathrm{V_{pkpk}}$ for 200 s were interleaved between waveform applications inducing breakdown to allow the resistor and TVS diode to cool. Room temperature was monitored

via USB thermocouple and noted subsequent to each measurement during testing.

Fig 4.2 shows circuit diagrams of the circuits used for testing. The 10 Ω CLR was chosen to replicate that intended to be used in the LVT protection circuit. Room temperature was again monitored and remained at 19 $\pm 1°C$ throughout testing.

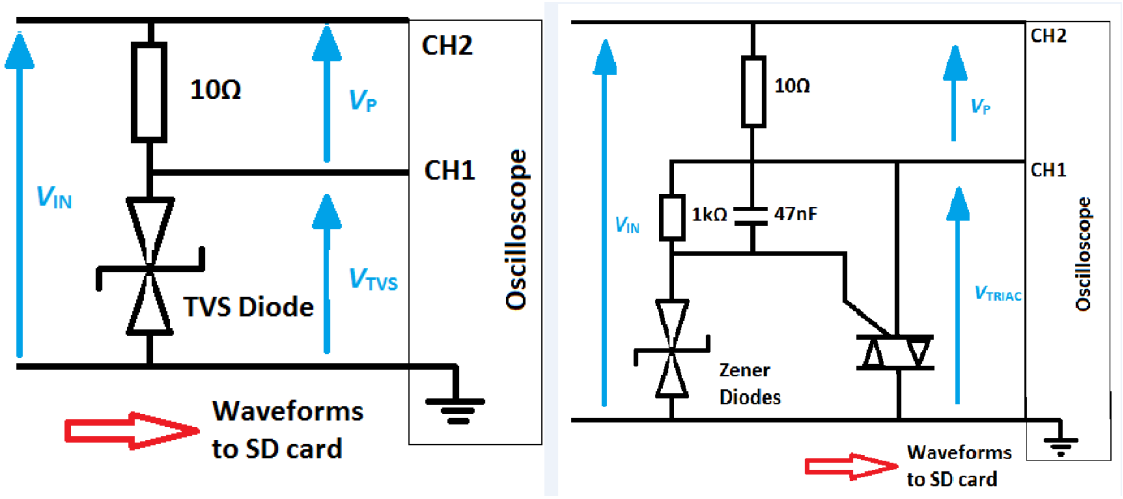

Figure 4.2: TVS (left) and TRIAC (right) test circuit diagrams.

The burden resistor resistance was originally selected as 1 Ω to fully utilise the LVT's dynamic range, taking into account the 1 A_{RMS} secondary nominal current, producing 1 V_{RMS} and 20 V_{RMS} across the burden resistor for the 5P20 rating. The manufacturers define the breakdown and clamping voltage of the TVS diodes as those that occur upon imposition of a 'double exponential' unipolar waveform, which differs from the waveforms anticipated in this application. Therefore, the devices require testing to understand their behaviour when subjected to waveforms similar to those anticipated in the field upon the occurrence of a grid fault. In the event of such a fault, the current can be modelled using a short circuited series RL circuit, assuming that the synchronous generators on the line behave as sinusoidal AC voltage sources. Kirchhoff's voltage law gives a differential equation whose solution is a sinusoid with an exponentially decaying DC offset [93]. Thus, the fault waveforms expected in the field take the form of 50 Hz exponentially decaying

sine waveforms with varying DC offsets. These faults can be phase to phase, or phase to ground and are expected to last up to a second in duration.

The maximum voltage across the burden resistor under fault conditions is an important unknown parameter. This parameter is limited by the instrument transformers knee point [94]. Strathclyde has obtained data from a recent fault on 275 kV high voltage lines at Wishaw, UK in which initial peak fault currents are 31 times nominal, dropping to 17 times nominal after 100 ms [95]. Based on this information and the definition of the knee point, the implication is that if the primary current increases by 50%, the secondary will only rise by 10%. Assuming that the knee point is specified correctly and is just above 20 times the nominal current level (a 5P20 standard transformer will be installed at Wishaw) then even if the primary current increases to 31 times the nominal (~50% rise), the expected secondary rise would at most be 10% extra, i.e. 22 times the nominal level. So, from this, the worst case scenario of voltage at the burden resistor can be estimated as 22 $\times\sqrt{2}$=44 V_{pk}. To account for a margin, both in the obtained fault levels and the knee point assumptions, a conservative design voltage for the selection of the burden resistor has been chosen as 60 V_{pk}. For the desired 5P class the standard specifies no limits on the current measurement error above the rated accuracy limit.

4.3 Transient voltage suppression devices

TVS devices can be classed as either clamping devices, in which an applied waveform 'cuts off' above a threshold voltage, or crowbar devices, in which the voltage across the device switches to a low voltage in the device on state. Two clamping devices in common use are metal oxide varistors (MOVs) and TVS diodes. In the former, metal oxide - ceramic grain boundaries act as pn junctions, producing an *I-V* characteristic of the same form as that of a Zener diode. MOVs have clamping voltages too high for this specification, therefore TVS diodes are the clamping device of choice. A bidirectional TVS diode can be thought of as two Zener diodes connected in series, anode-anode or cathode-cathode. Despite the

similarity however, a TVS diode is preferable to a Zener diode as Zener diodes are designed and tested for voltage regulation applications whilst TVS diodes are specifically designed and tested for transient voltage suppression. Gas discharge tubes and TRIACs are both devices used in crowbar circuits. Gas discharge tubes however, have crowbar voltages too high for the present applications requirements.

4.3.1 TVS diode critical parameters

Fig 4.3 shows the double exponential waveform used by manufacturers to characterise the I-V behaviour of the TVS diodes.

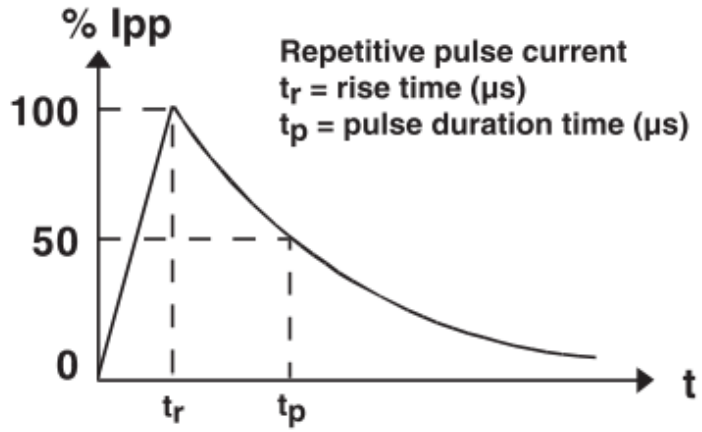

Figure 4.3: Double exponential waveform from ST P6KE datasheet [96]. Here I_{PP} signifies the peak pulse current.

There are three critical voltages on a TVS diode I-V plot; the clamping V_{CL}, breakdown V_{BR} and reverse stand-off V_{RM}, voltages. The clamping voltage is the voltage across the device in the 'on' state, i.e. the maximum voltage across the diode before it restricts a further voltage increase across it. Manufacturers specify this voltage for a given peak pulse current I_{PP}. The breakdown voltage is the voltage at which the device undergoes dielectric breakdown. Finally, the reverse stand-off voltage is the voltage below which no significant conduction occurs; manufacturers define the limiting current here as I_{RM}. Fig 4.4 displays

the I-V characteristic of a bidirectional TVS diode, with key parameters annotated.

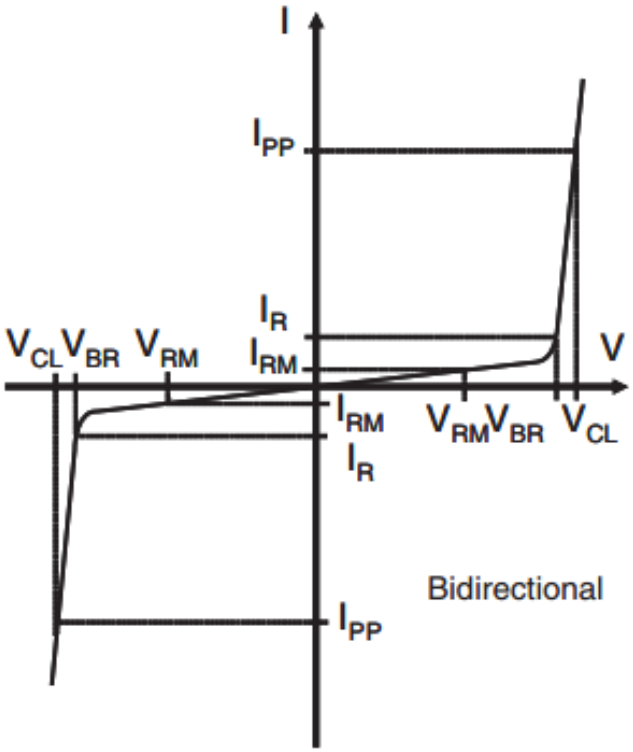

Figure 4.4: I-V curve with parameter annotations for a bidirectional TVS diode from ST P6KE datasheet [96]. The annotation abbreviations are as follows; V_{RM} stand-off voltage, V_{BR} breakdown voltage, V_{CL} clamping voltage, I_{RM} leakage current at V_{RM}, I_{PP} peak pulse current.

4.3.2 TRIAC critical parameters

A TRIAC is a bidirectional silicon controlled rectifier (thyristor). It has a different operating principle for each quadrant of the I-V plot, and those relevant to the present specification are quadrants one and three (see Fig 4.5), depending on the voltage polarity of the anode one, anode two and gate terminals.

Key parameters in Fig 4.5 are the peak repetitive forward off state voltage V_{DRM}, the peak repetitive forward blocking current I_{DRM}, the maximum on state voltage V_{TM} and

the holding current I_{H}. V_{DRM} is the maximum manufacturer rated voltage for continuous AC operation in the 'off' state. V_{TM} is analogous to the clamping voltage of a TVS diode for a TRIAC. Upon reaching dielectric breakdown, the device remains in the 'on' state until the current drops below the holding current or the voltage is removed.

Symbol	Parameter
V_{DRM}	Peak Repetitive Forward Off State Voltage
I_{DRM}	Peak Forward Blocking Current
V_{RRM}	Peak Repetitive Reverse Off State Voltage
I_{RRM}	Peak Reverse Blocking Current
V_{TM}	Maximum On State Voltage
I_H	Holding Current

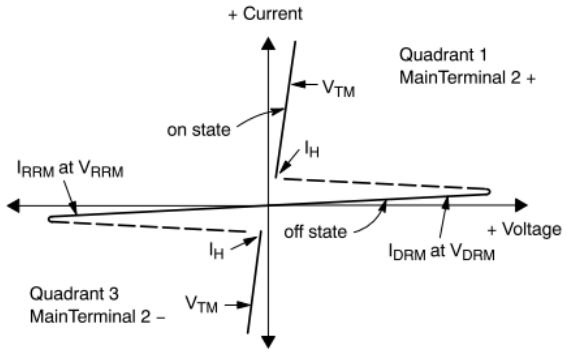

Figure 4.5: *I-V* curve with symbol parameter annotations for a TRIAC from ON Semiconductor BTA30-600CW3G datasheet [97].

4.3.3 Critical steps involved in selecting a TVS diode

1. Define limits of operation - the minimum breakdown voltage and the maximum clamping voltage.

   (a) The voltage across the LVT should not exceed 30 V_{pk}, which is a recommendation given by the manufacturer. However, it should be noted that preliminary tests carried out by Synaptec indicate that this voltage can indeed be exceeded without adverse effects on the device. Further investigations will be desirable to understand fully how exceeding this value affects the device performance or longevity. Notwithstanding this discovery, it is still assumed, for the purpose of this thesis, that the 30 V value should not be exceeded. Select the burden resistor to maximise the dynamic range for the given secondary nominal rating (1 or 5 A) and the rated accuracy limit primary current. The resistor should

be selected such that at the rated accuracy limit primary current, the voltage across the burden is just below 30 V. A 1 Ω resistor meets this requirement for the 1 A secondary rating and a 5P20 protection class CT - as installed at Wishaw. At the accuracy limit, the voltage across the 1 Ω burden will reach $20 \times \sqrt{2} = 28.3\ V_{pk}$.

(b) Simulations indicate that for a 4 kHz or 4.8 kHz sampling rate (as required by BS EN 60044-8 [1] and BS EN 61869-9 [98] respectively), sampling a 51 Hz signal, the BS EN 60044 5P20 5% composite error accuracy limit is breached when the diode clamps below 25.7 V_{pk}. This simulation uses the RC filter correction factors from Eqn 4.2 and Eqn 4.4, and a 10 Ω CL resistance, to obtain the magnitude and phase values. The Ohmite 850F1ROE burden resistors resistance at the lowest temperature required -5 °C was also factored into the simulation. This minimum breakdown voltage is however, larger than this value as RMS current error must be shared with other error inducing factors:

i. Transformer error due the core's magnetic hysteresis.

ii. Error due to the effective RC filter of the PS - CLR combination.

iii. Errors due to inaccuracy in piezoelectric hysteresis, temperature and ageing error compensation.

2. Define maximum transient current I_{PP} (Fig 4.4).

   The CLR resistance, the voltage across the TVS diode and the maximum voltage across the burden resistor in the event of a fault, determine this.

3. Select minimum TVS power rating.

   The minimum power rating must be greater than the maximum power that the diode will have to dissipate. The maximum voltage across the CLR upon fault initiation, and its resistance value, determine the peak pulse current I_{PP}, which, together with the current fault waveform and duration, determines the maximum power. The

maximum power for both the Littelfuse and Transil P6KE series [96] [99] is 600 W for a 10/1000 µs double exponential waveform with duty cycle of 0.01%, and 1.5 kW for the Littelfuse SMCJ series [100].

4. The CLR resistance should be high enough such that the diodes clamping voltage range remains below the PS voltage limit, but otherwise minimised to minimise the amplitude and phase error associated with the inherent RC filter.

5. *I-V* curve characterisation is required to test the TVS diodes behaviour when subjected to DC and AC waveforms, as the manufacturers typically specify parameters for double exponential faults.

6. In the event that the requirements of step one cannot be met due to the breakdown voltage being too low for the available TVS diodes, standard silicone diodes could be placed in series with the TVS diode, to shift the breakdown voltage into the required limits. A pre-selection process can also be applied to achieve the correct value. Furthermore, in light of the test results confirming that exceeding the 30 V level has no adverse effects on the LVT, a small excess of up to 20% (6 V) will likely be acceptable.

7. Define operating temperature range. Both the Transil P6KE and Littelfuse SMCJ datasheets specify a change in breakdown voltage with temperature given by Eqn 4.1.

$$\Delta V_{BR} = \alpha \cdot (T - 25) \cdot V_{BR}(25°C) \tag{4.1}$$

Here, α is a constant of order $10^{-3\circ}$ C^{-1} and T is the ambient temperature. The manufacturers give no information on the effect of thermal or mechanical shocks or vibration on the diodes accuracy.

Table 4.1 gives the minimum and maximum V_{BR} for a selection of diodes taking into account the tolerance and temperature variation in V_{BR}.

Table 4.1: Comparison of minimum and maximum breakdown voltages expected from Transil P6KE and Littelfuse SMCJ TVS diodes.

TVS Diode	α (10^{-4}/°C)	V_{BR} Tolerance (V)	MIN → MAX V_{BR} in T range -5 to 75 °C (V)
Transil P6KE22CA	9.2	20.9 → 23.1	20.3 → 24.2
Transil P6KE24CA	9.4	22.8 → 25.2	22.2 → 26.4
Transil P6KE27CA	9.6	25.7 → 28.4	25.0 → 29.8
Transil P6KE30CA	9.7	28.5 → 31.5	27.7 → 33.0
Littelfuse SMCJ26CA	10	28.9 → 31.9	28.0 → 33.5
Littelfuse SMCJ28CA	10	31.1 → 34.4	30.2 → 36.1
Transil P6KE33CA	9.8	31.4 → 34.7	30.5 → 36.4
Littelfuse SMCJ30CA	10	33.3 → 36.8	32.3 → 38.6
Littelfuse SMCJ33CA	10	36.7 → 40.6	35.6 → 42.0

Given the V_{BR} ranges shown in Table 4.1, the requirements of step two are impossible to attain. Littelfuse SMCJ28CA, (highlighted in green in Table 4.1), is the first diode to go into breakdown above the 5P20 accuracy limit (20 $\mathrm{V_{RMS}}$ or 28.3 $\mathrm{V_{pk}}$) in Table 4.1, within the temperature range considered. Thus, if the PS can indeed cope with voltages in excess of ± 36.1 $\mathrm{V_{pk}}$ then this thesis recommends use of diode SMCJ28CA to avoid breakdown occurring in the 5P20 accuracy regime due to temperature fluctuations. Transil P6KE30CA and Littelfuse SMCJ26CA (highlighted in amber) are also viable options, but these would introduce an undesirable, but acceptable (below 5%) contribution to the sensors composite error below the 5P20 accuracy limit. For this reason they are not recommended.

4.3.4 Observations regarding TVS diode performance

Appendix A contains the TVS diode *I-V* plots. One new TVS P6KE24CA diode failed (open circuit) following exposure to a 1 s, 48.8 V_{pkpk} sinusoidal waveform (V_{IN} was 71.2 V_{pkpk}). This suggests that a pre-selection process or stress screening, to eliminate poorly performing diodes may be useful. Furthermore, for the diodes that performed correctly, often, breakdown occurs for one direction before the other, producing an asymmetric waveform - this effect could potentially be compensated for in software, if measurement of fault waveforms were desired.

For the waveforms of 1 s in duration, the clamping voltage for both voltage polarities was observed to gradually increase with time. For example, on one run, the V_{pkpk} between positive and negative clamping of a TVS P6KE27CA diode on a 1 s, $V_{IN} = 113.0 \pm 5.4$ V_{pkpk} trace, exhibited an increase of 9.6 V_{pkpk}, and on TVS P6KE24CA diode exhibited an increase of 4.8 V_{pkpk} during a 1 s fault at $V_{IN} = 112.0 \pm 5.4$ V_{pkpk}. In the former case, assuming the maximum V_{BR} within the tolerance range of this diode; 28.4 V_{pk}, this ΔV_{BR} could be attributed to a temperature increase of 201 ° C from 25 ° C using Eqn 4.1. This temperature increase seems high and the increase in clamping voltage with time requires further investigation if the circuit does indeed require a TVS diode.

- Does the increase in clamping voltage occur during clamping operation on a given half cycle or does the increase occur over successive clamp activations?
- Does this behaviour occur for V_{IN} less than 113 V_{pkpk} applied for less than 1 s?

TVS P6KE30CA and P6KE24CA diodes were tested up to $V_{IN} = 120.0 \pm 5.6$ and 119.0 ± 5.6 V_{pkpk} AC respectively for 1 s durations with no adverse effects other than those stated above. One TVS P6KE27CA diode, however, displayed an unstable clamping voltage for one voltage polarity, shortly, but not immediately after having been exposed to AC $V_{IN} = 126.0 \pm 5.8$ V_{pkpk} for $1s$. This may be due to the fact that the 10 Ω resistor failed at this voltage.

The range of the breakdown voltage (voltage at which waveform distortion was observed to occur) for different diodes of the same class was 2.6, 0.6 and 2.8 for TVS P6KE24CA, P6KE27CA, and P6KE30CA, respectively. This lies within the ± 3 V maximum voltage measurement uncertainty due to the oscilloscope.

4.3.5 Determination of required TVS diode power rating

During a worst case scenario, a DC fault in which the TVS diode is subjected to 60 VDC for 1 s, around 90 W would be deposited in the diode (minimum breakdown voltage of TVS diode SMCJ28CA times current through CLR in this scenario).

The SMCJ diodes power rating is 1.5 kW for a 10/1000 µs pulse with a duty cycle of 0.01%; therefore, switching from the 600 W P6KE diodes shouldn't pose a problem if the P6KE power rating is indeed suitable. This pulse power and duration gives a maximum energy to be dissipated of <1.5 J for the SMCJ diodes. Assuming that the peak pulse power versus pulse duration fit for the 1.5 kW diode in the SMCJ datasheet [100] holds for pulse widths up to 1 s, extrapolating gives approximately 67 W at 1 s. For a square wave, the maximum power should be reduced to 66% of the double exponential value [101], giving 44 W. Assuming a 30.2 V clamping voltage, this gives a maximum current through the diode of 44 W / 30.2 V = 1.46 A, corresponding to a voltage across the CLR of 1.46 A × 10 Ω = 14.6 V. Therefore the maximum 1 s DC withstand of the device corresponds to a voltage across the burden resistor of 30.4 V + 14.6 V = 45 V.

The datasheet states that the diode can withstand 500 W for a pulse duration of 10 ms [100]. For a half sinusoidal fault, 75% of the rated double exponential power must be used [101], giving 375 W. Although this is four times the peak power of the present application, the values quotes by the manufacturer are assumed to apply for either a single pulse or a duty cycle of 0.01% and in this application the duty cycle is much greater.

Simulations show that for a 50 Hz sine wave, of amplitude 60 V_{pk} across the burden resistor, with a clamping voltage of 30.2 V across the CLR, an RMS current of 1.74 A flows through a 10 Ω CLR. Multiplying the RMS current by the clamping voltage gives

an average power of 53 W. Given that the manufacturer characterisation uses double exponential pulses, whilst the CTs fault waveforms are sinusoidal, it is difficult to make a power comparison and therefore the diodes were experimentally tested. As discussed previously, Transil P6KE diodes were tested with 120 V_{pkpk} AC waveforms for up to 1 s and displayed no adverse effects so either diodes power rating should be suitable.

4.3.6 Observations regarding TRIAC performance

Appendix A contains the results of TRIAC *I-V* characterisation and shows asymmetrical operation - this could again be compensated in software through tailoring the gate current such that the TRIAC becomes bi-directionally operational at 30 V_{pk}.

4.4 Current limiting resistor selection

4.4.1 Resistor choice for a 5P20 class OCS

The sensor capacitance and the CLR resistance in the LVT produce an effective low pass RC filter. With transmission networks increasingly interested in measurement of higher order harmonics up to the 100th harmonic [102], this is an aspect of the LVT's external circuitry design that needs to be managed carefully. It is assumed that there is no temperature and voltage dependence of the TVS diode capacitance and no frequency dependence of both TVS diode and piezoelectric capacitance. The former is justifiable due to the fact that the TVS capacitance is negligible in comparison with that of the PS, whilst the latter is justifiable as accurate measurements above the 5th harmonic are surplus to requirements.

In the Bode plot shown in Fig 4.6, to ascertain the worst possible scenario, a tolerance (TOL) of 10% and a temperature coefficient of resistance (TCR) of 900 ppm°C^{-1} has been attributed to the CLR and a temperature change from 25° C, ΔT, of 50 ° C assumed. In addition to this, the manufacturer specified load life (LL1+LL2) as per BS EN 60115-1 for 1000 h at 25 ° C; 1%+0.005 Ω was added to the CLR resistance [103]. Eqn 4.2 gives the resulting expression for maximum resistance R_{TOTALMAX} and Eqn 4.3 shows the values

used. It is assumed that this value is temperature independent for simplicity here. The maximum resistance achievable with these values was then used as the resistance value for the plots. The Vishay LTO 100 series resistors are available with TOL 1, 2, 5 and 10% and TCR 200, 350 and 900 ppm° C^{-1} .

$$R_{TOTALMAX} = ((R \cdot (1 + TOL) \cdot (1 + LL1)) + LL2) \cdot (1 + (\Delta T \cdot TCR)) \tag{4.2}$$

$$R_{TOTALMAX} = ((10 \cdot 1.1 \cdot 1.01) + 0.005) \cdot (1 + (50 \cdot 350 \cdot 10^{-6})) \tag{4.3}$$

The PS used (5 × 5 × 18 mm) has a capacitance, C_{STACK}, of 1.5 µF measured at 1 V, 1 kHz, 20 ° C [47] and to this value has been added the manufacturer quoted tolerance (TOL) of 20%, plus a temperature correction, TC, of 20% to account for a temperature of up to 75 ° C and voltage of 3 V_{pkpk}. In order to obtain this estimate, a linear fit was extrapolated backwards from the first two points at 75 ° C from the aforementioned relative capacitance versus voltage plot on the PI web page [47] . Finally the parallel TVS capacitance C_{TVS} of 1200 pF [100] (corresponding to TVS SMCJ28CA at 0 V) was added. Eqn 4.4 gives the resulting expression for the total capacitance, C_{TOTALMAX}, and Eqn 4.5 demonstrates the values used.

$$C_{TOTALMAX} = C_{STACK} \cdot (1 + TOL) \cdot (1 + TC) + C_{TVS} \tag{4.4}$$

$$C_{TOTALMAX} = 1.5e^{-6} \cdot 1.2 \cdot 1.35 + 1200 \times 10^{-12} \tag{4.5}$$

Fig 4.6 displays the relevant current and phase error limitations set by BS EN 60044-8:2002 Instrument transformers - Part 8: Electronic current transformer [1]. The UNR 4-3425 Vishay precision burden resistor was found to be unsuitable for the application, (detailed in section 4.6), and as such an Ohmite 850F1ROE resistor has been assumed as

the burden resistor. The UNR 4-3425 Vishay precision burden resistor has a maximum temperature coefficient of 50 ppm$°C^{-1}$, a tolerance of ± 0.01% and a 1000 h load stability of 0.01% is assumed in the absence of a specific value based on that of the UNR 4-3425 [104]. These factors have been accounted for and removed from the permissible voltage error lines in Fig 4.6.

Eqn 4.6 gives the expression for the maximum error scenario (rounded down) value used as the permissible fundamental voltage error line, for the calculations in which R_{TOTAL} and C_{TOTAL} were maximised. The first term is -1% in (voltage) decibels whilst the second takes into account the resistance change of the burden resistor due to temperature in going from 25 to 75° C as 50 × 50 ppm, plus the burden resistor tolerance of 1% and assume no load life; in the maximum error scenario, the voltage across the burden resistor is minimised for a given temperature therefore burden resistance should be maximised in this equation.

$$20 \cdot (log_{10}(0.99) + log_{10}(1 + 10^{-2}) \cdot (1 + 50 \cdot 50 \cdot 10^{-6}))) = -0.02 \tag{4.6}$$

Eqn 4.7 gives the expression for the minimum error scenario (rounded down) value used as the permissible fundamental voltage error line. Again the first term is -1% in (voltage) decibels and the second accounts for the resistance change of the burden resistor due to temperature in going from 25 to -5° C as 30×50 ppm, minus tolerance 0.01% and 0.01% load life; in the minimum error scenario voltage across burden is a maximum for given temperature therefore burden resistance should be minimised in this equation.

$$20 \cdot (log_{10}(0.99) + log_{10}((1 - 10^{-2}) \cdot (1 - 10^{-2}) \cdot (1 - 30 \cdot 50 \cdot 10^{-6})) = -0.18 \tag{4.7}$$

The same expressions were used to modify the permissible 5th harmonic voltage error lines for the maximum and minimum error scenarios respectively, with 0.9 substituted for 0.99 in the first term of the expression.

As the device utilises a precision 1 Ω burden resistor the error specifications for current

measurement are essentially the same as the error specifications for voltage measurement. The requirements of interest here for the 5P20 class device are:

- <1% current error at rated primary current (1 A_{RMS})
- <1°phase error at rated primary current in the range 48 - 51 Hz
- <5% composite error at rated accuracy limit (20 × 1 A_{RMS})
- <10% current error at 1/3, 2, 3, 4, 5th harmonic
- <10°phase error at 1/3, 2, 3, 4, 5th harmonic

The test described in the standard to qualify the device to the harmonic requirements for the 2nd, 3rd, 4th and 5th harmonic specifies that the amplitudes of each harmonic should be equal to 10 % of rated current. It is assumed, though not explicitly stated, that these requirements must be met under normal service conditions as described in the standard. The minimum and maximum temperatures under the bracket of normal service conditions are stated as -5 and 40° C.

Fig 4.6 was produced using an 22 Ω resistance for the CLR in the circuit. This is the maximum acceptable integer value above which the 1°phase error criterion of the relevant standard for PX class CTs is not met. Simulations show that the composite error when using 22 Ω and 51 Hz is 1.71%.

When using a 10 Ω CLR, there is a margin of -0.55°between the permissible phase error at fundamental frequency and phase error introduced at 51 Hz. The magnitude is reduced by ~5.7×10^{-4} dB (0.0065%) at this frequency. To obtain this value, the correction factors from Eqns 4.2 and 4.4 were used. This sets a limit for the accuracy of the piezoelectric and CT hysteresis compensation procedures, however this phase error may also be compensated in software. The magnitude and phase errors drop below -10% and -10°between the 58th and 59th and the 22nd and 23rd harmonics respectively. The RC filters contribution to the composite error using this 10 Ω and 51 Hz has been simulated and found to be 0.56%.

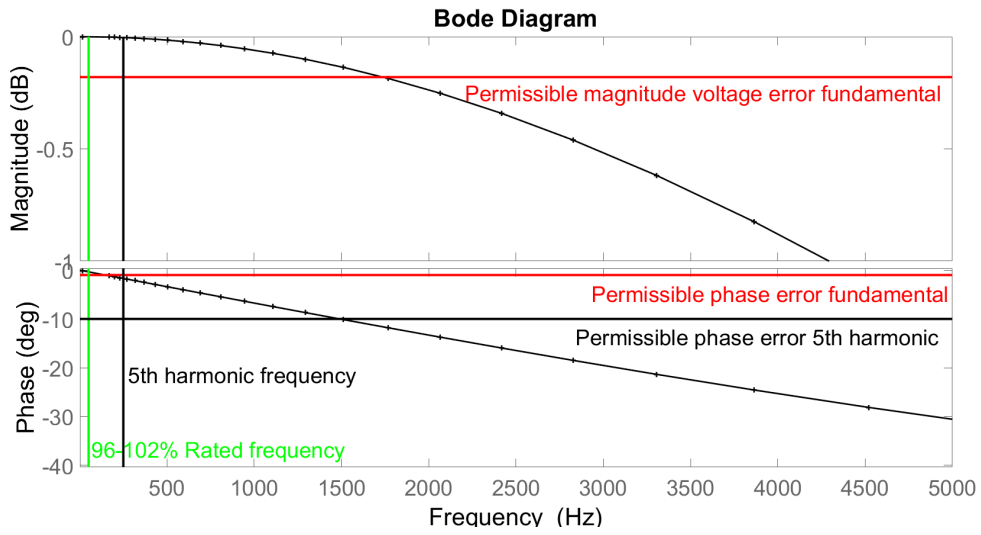

Figure 4.6: Bode plot of first order RC low pass filter produced by the combination of the PS capacitance and the CLR. The CLR has been chosen at 22 Ω for this plot. Above this value the 1°phase error criterion of the relevant standard is not met.

The Bode diagrams of the first order RC low pass filter in the case that resistances and capacitances are at the lowest extreme values have been plotted. In Eqn 4.8, it is assumed that no error associated with load life is present, and the lowest resistance achievable within the tolerance range and a temperature of -5 ° C has been used.

$$C_{TOTALMIN} = R \cdot 0.9 \cdot (1 - (30 \cdot 350 \cdot 10^{-6})) \tag{4.8}$$

For the capacitance in Eqn 4.9, the lowest PS capacitance achievable within the tolerance range is assumed, and 20% removed for temperature variation. The temperature variation has been obtained by extrapolating a linear fit of relative PS capacitance versus temperature from the PI website [47] back towards -5 ° C.

$$C_{TOTALMIN} = C_{STACK} \cdot 0.8 \cdot 0.8 + C_{TVS} \tag{4.9}$$

Using Eqn 4.8 and Eqn 4.9 and a 10 Ω CLR at 51 Hz, a margin of -0.84°between the permissible phase error at fundamental frequency and phase error introduced has been determined, and the magnitude is reduced by $9.5 \times 10{-}5$ dB (0.01%). This leads to a composite error of 0.20%.

The difference in maximum and minimum error values can be used as the uncertainty in error over time and devices due to the RC filter. There will be a fluctuation of up to 0.007% in current error, 0.47° in phase error and 0.007% in composite error, across devices and time owing to load life, temperature, and tolerances. These values have been determined at 51 Hz using the max and min expressions for R and C for a 10 Ω CLR. These errors can be compensated in software but compensation of the variation across devices and due to environmental factors would require an added layer of complexity. Note that due to the tolerance on the burden resistor exceeding the accuracy requirement in the rated frequency range, in the worst case scenario, the 0,2 metering class accuracy requirements cannot be met for any value of resistance without compensation.

4.4.2 Determination of power rating of CLR

Assuming a 10 Ω CLR with the tolerances added as in the minimum resistance of Eqn 4.8, taking the resistance to 8.9 Ω, a TVS clamping voltage of 30.2 V_{pk}, corresponding to the minimum breakdown voltage of TVS diode SMCJ28CA, a maximum fault duration of 1 s and a maximum voltage across the burden resistor of 60 VDC, a maximum power of 99.8 W is calculated for a 1 s overload. A safety factor should be considered in determining the power rating as power dissipation depends upon temperature and relative humidity.

In free air, the maximum power rating of the LTO 100 and LTO 30 resistors are given as 3.5 W and at 2.25 W at 25 ° C respectively. The LTO 100 datasheet [105] shows the maximum power versus short period overload duration quoted for both of these resistors. This applies to resistors in air or mounted onto a heatsink. LTO 100 is rated for 100 W with heat sink attachment at 25 ° C. Extrapolating the plot from the datasheet it is seen that the maximum power for a duration of 1 s is approximately 65 W. Thus, the power rating

of LTO 30 is insufficient for a 60VDC fault without a heat sink, by both the continuous power rating and the method just described. Despite LTO 30 surviving the experimental testing, this thesis strongly recommends to either use the LTO 100 in future builds (which will require a PCB redesign due to larger separation between pins), or perform testing of LTO 30 at temperatures up to 40 ° C. In the event of utilisation of a heat sink for the burden resistor, as an extra precaution the LTO 100 could be mounted onto the heat sink too. This may also marginally improve sensor accuracy in the immediate aftermath of a fault due to faster cooling. However, it should be noted that the failure of a CLR is not catastrophic as is the case of the burden resistor.

Eqn 4.10 gives the required heat sink thermal resistance R_{SA} to dissipate power P (99.8 W), in terms of the maximum device temperature T_{max}, and the maximum ambient temperature under which the device must operate, $T_{\mathrm{A}} = 40°$ C, interface thermal resistance R_{CI}, and the resistor thermal resistance $R_{\mathrm{JC}} = 1.5$ °C W^{-1}. The manufacturer specifies that the resistor should not exceed $T_{\mathrm{max}} = 175$ ° C.

$$R_{SA} + R_{CI} = (T_{max} - T_A)/P - R_{JC}[105] \tag{4.10}$$

Upon plugging these values into Eqn 4.10, it is seen that this conservative specification cannot be met. instead, considering a maximum voltage across the burden resistor of 60 $\mathrm{V_{pk}}$. The average power dissipated in the CLR during one 50 Hz period at this voltage has been approximated as 34.4 W to one decimal place via the following method. A single period 50 Hz sine wave of amplitude 60 $\mathrm{V_{pk}}$ with clamping at 30.2 $\mathrm{V_{pk}}$, corresponding to the minimum breakdown voltage of TVS diode SMCJ28CA, was subtracted from an otherwise identical unclamped sine wave. This waveform was taken as the voltage waveform across the resistor and the current waveform was determined via Ohm's law. In doing so, the minimum CL resistance expressed in Eqn 4.8 was used to maximise the average power. These waveforms were multiplied together to obtain a waveform for the instantaneous power. Finally, the instantaneous power waveform was integrated using Simpson's rule

and divided by a single 50 Hz period to obtain an average power of 34.4 W. This is well within the 100 W quoted for the LTO100 resistor with heat sink, and the 65 W obtained from extrapolating the plot from the datasheet.

In addition to this, assuming an 8.9 Ω CLR, a TVS clamping voltage of 30.2 V_{pk}, corresponding to the minimum breakdown voltage of TVS diode SMCJ28CA, a maximum fault duration of 1 s and a maximum voltage across the burden resistor of a less conservative 45 VDC, a maximum power of 24.6 W for a 1 s overload is calculated.

To achieve improved thermal conductivity between heat sink and resistor case (to prevent insulating air pockets from arising between the two components), a thermal grease or pad should be used. A pad is preferable for electrical insulation in case electrical contact is accidentally made to the heat sink. For example for a Fischer Elektronik WLFT 404 pad of thermal conductivity k = 0.37 Wm^{-1} $°C^{-1}$ [106] on an LTO 100 resistor of area A = (15.76 mm × 20.7 mm) and thickness L = 0.127 mm, the thermal resistance can be calculated as 1 $°CW^{-1}$ via Eqn 4.11.

$$R_T = \frac{L}{KA} \tag{4.11}$$

Using 34.4 W from the AC 60 V_{pk} scenario above, via Eqn 4.10, it is found that a heat sink and interface material with a thermal resistance of 2.42 $°CW^{-1}$ is required. Fischer Elektronic supply heat sinks of thermal resistance below the required 1.42 $°CW^{-1}$ rating. Alternatively, this value may be deemed too conservative, and a heat sink of thermal resistance 2.98 $°CW^{-1}$ could, instead be chosen to dissipate the 24.6 W from the 45 VDC scenario.

4.5 Piezoelectric stack maximum voltage investigations

Synaptec recently tested the LVTs above the 30 V_{pk} limit specified by PI Ceramic. Testing continues but early results indicate that the limit may not be a concern. The peak-peak wavelength of an LVT was monitored whilst it was subjected to 20 V_{pkpk} voltage

steps, with a 5 second settle period after each [107]. The sensor displayed no unusual behaviour until 180 V_{pkpk} was reached and the solder connections to the leads melted due to excessive heating, causing one lead to disconnect. The effect of voltage transients exceeding the recommended voltage withstand of the PS on device OS should be investigated more thoroughly, making use of longer settle periods. Furthermore, an investigation of PS behaviour under DC offset conditions, such as can occur during a fault, should also be conducted.

Initially, it was thought that beyond the 60 V_{pkpk} limit, the sensor would either undergo a net piezoelectric domain polarisation reversal, producing a distorted effective clamp on the waveform under one voltage polarity, or the sensor would reach the saturation polarisation, again producing an effective clamp on the waveform. Fig 4.7 demonstrates that polarisation reversal actually occurs within the range 160-180 V_{pkpk}. Upon stepping to 180 V_{pkpk}, the waveform becomes increasingly distorted with time. Heating of the stack may cause this, however, stack temperature was not monitored.

In light of this new information, the voltage limits between which the TVS diode must operate may be significantly relaxed, and if further testing validates that the PS can maintain nominal operation if subjected to faults in excess of ±40 VDC, then this thesis recommends to use TVS SMJ33CA diodes to avoid to the possibility of breakdown occurring within the 5P20 operating range. Ultimately, however, if it is proven that the PS can reliably withstand 60 VDC and 120 V_{pkpk} AC in both directions for a duration of 1 s, then the TVS diode could be removed from the circuit altogether.

4.6 UNR 4-3425 burden resistor testing

4.6.1 Introduction

The 1 Ω burden resistor specified in Section 4.2.1 is made up using two 2 Ω UNR 4-325 resistors in parallel to reduce the power output on each. Each resistor is rated at 15 A and 50 W with heat sink attached. It is unclear whether the current rating is peak or RMS,

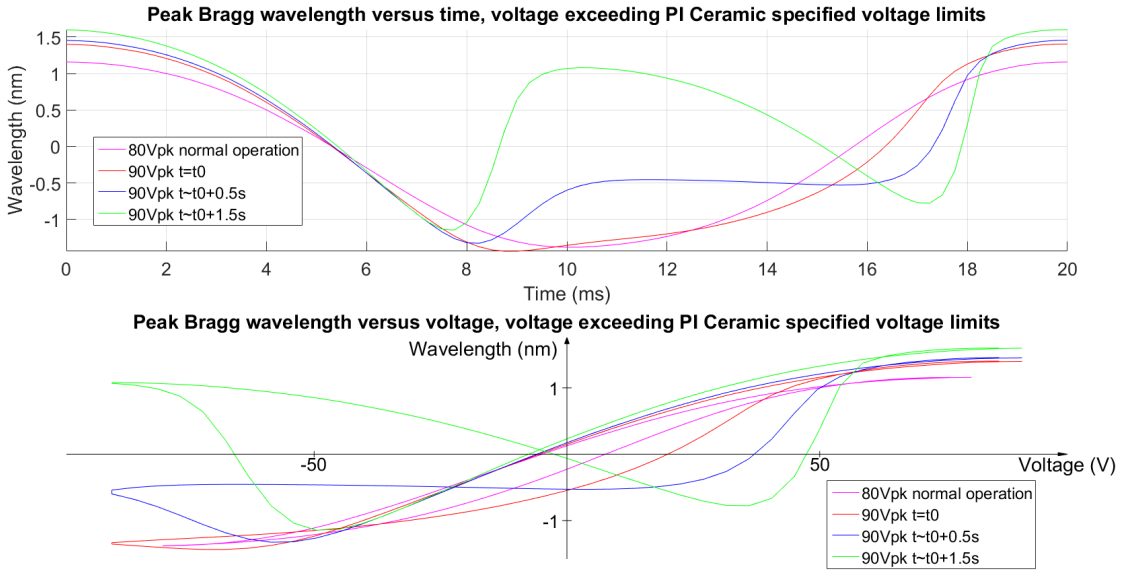

Figure 4.7: Peak Bragg wavelength versus time (top) and versus voltage (bottom), for voltages in excess of manufacturer specified voltage limits. Data courtesy of Synaptec.

DC or AC. The manufacturer states that the current rating is for onset of resistor *I-V* characteristic non-linearity; not the maximum current before failure [108]. The heat sink keeps the temperature of the resistive component below a maximum temperature of 155 ° C [104]. A standard extruded SK 58 Fischer Elektronik heat sink with thermal resistance 1.4 °W^{-1} was selected previously by the AST (Advanced Sensors Team) and has been fitted with three burden resistors to two heat sinks, with the resistors connected via thermal pads of thermal resistance 1 °W^{-1} to ensure good thermal contact with, and electrical isolation from the sink.

A short time power overload is not given in the datasheet, however the manufacturer specifies that as a general rule the maximum pulse power for pulses from 1-25 s in duration is 25 times the rated pulse power divided by the pulse duration in seconds [108].This comes to 1.25 kW for a pulse duration of 1 s, which gives a maximum voltage and current across each resistor of DC 50 V and 25 A respectively. This is short of the conservative 60 V value

used previously in this document but 50 VDC is still above the anticipated maximum fault voltage described in the introduction. As this would entail currents of 25 A_{pk} through each resistor, it is desirable to test the resistors to ensure that they live up to their power rating and remain linear up to 10 A_{RMS} to satisfy 5P20 accuracy requirements.

The manufacturer specifies that for pulse duration of 100 ms or less, the peak pulse power should be calculated through consideration of the change in internal energy of the internal wire element during heating only [108]. Eqn 4.12 gives the peak pulse power.

$$P = \frac{mc\Delta T}{t} \tag{4.12}$$

Here P in the peak pulse power in W, m is the wire elements mass in kg, c is the wires specific heat in Jkg^{-1}, ΔT is the change in temperature of the junction from ambient and t is the pulse duration in s. Thus for a maximum temperature of 155 ° C, ambient temperature of 25 ° C, pulse duration of 100 ms, resistive element of mass 0.01 g, and a specific heat of 450 $Jkg^{-1}°C^{-1}$ (NiCr), the peak pulse power is 6 W. Given that the resistor is rated for 50 W continuously with heat sink attached, this value cannot be correct.

4.6.2 *I-V* characterisation

Fig 4.8 shows the experimental set-up for *I-V* characterisation of the burden resistor. A four terminal 0.1 Ω oil standard resistor rated for 22 A was connected in series with the four terminal burden resistor, and the Chroma 61512 programmable AC source configured for voltage output. The resistances of both resistors were measured prior to testing at 27±1° C using a Keysight DMM 34410A 6 1/2 digit. A National Instruments USBTC01 data logger and thermocouple J were used to monitor the burden resistor case temperature throughout the experiment. This thermocouple has an accuracy of ±1°C and a resolution of 0.07 ° C. A 3M thermal grease was applied between the case - thermocouple head interface to ensure good thermal contact. 100 ms pulses of DC voltage were applied using the Chroma 61512, with intervals of 0 V of minimum duration of 60 s interleaved between, allowing

the resistive element to cool. 100 ms was chosen as the pulse duration in this instance as modern circuit breakers are designed to activate within this time period, despite this not being the case at Wishaw in section 4.2.1 [109]. The voltage drop across each resistor was monitored using a GW Instek GDS-1042 oscilloscope with 10X probes. Current was calculated using Ohm's law using the measured initial resistance value of the 0.1 Ω resistor and the measured voltage across the same.

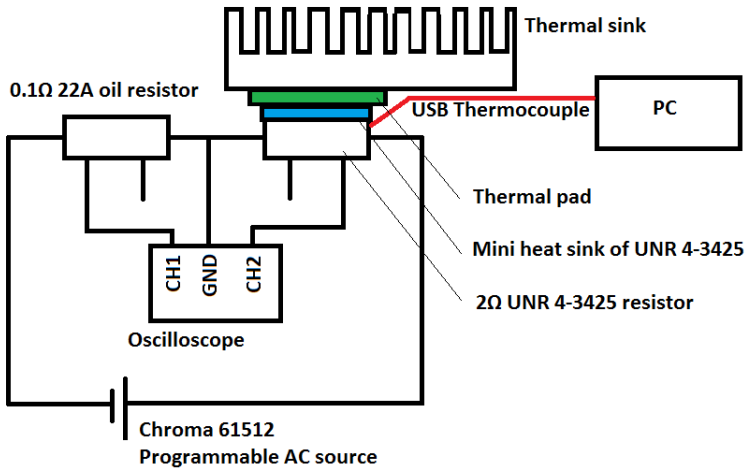

Figure 4.8: Experimental set-up for I-V characterisation of Vishay UNR-4325 2 Ω precision burden resistor.

Fig 4.9 shows the experimentally determined burden resistor I-V curve, whilst Fig 4.10 shows the resistor case temperature versus time during testing. The Chroma source output seemed temperamental, and jumped from 32.3 ± 2.0 V to 37.5 ± 2.1 V when it was programmed for only a 0.5 V increase. This resulted in 36.0 ± 2.1 V across the 2 Ω resistor, producing a current of 15.4 ± 3.3 A, causing it to fail open circuit. This corresponds to a power of 554.4 ± 123.1 W, which is less than half that expected due to a 50 VDC fault. The resistor also therefore did not survive up to the 5P20 accuracy requirement limit for current.

The resistor case temperature data is of limited use as although the resistive element temperature likely exceeded the maximum temperature specified by the manufacturer,

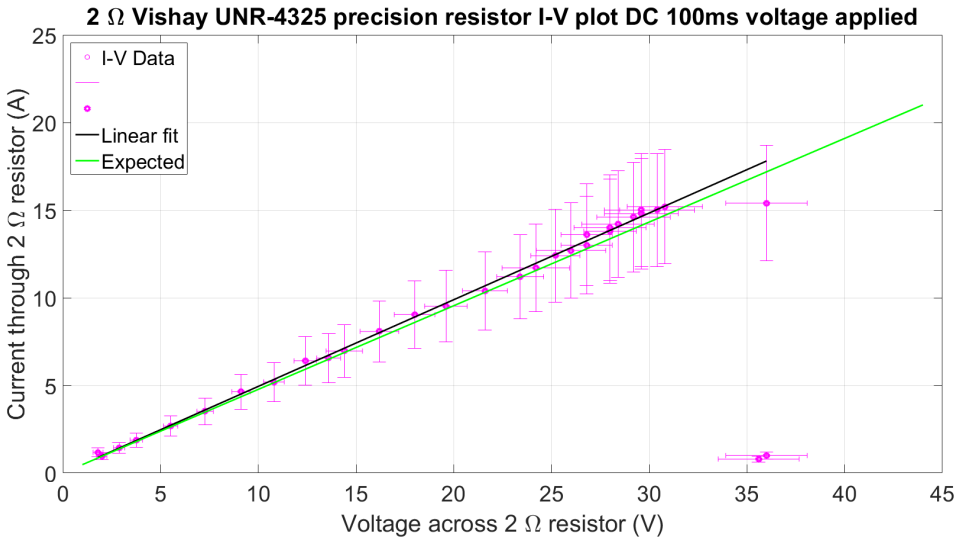

Figure 4.9: Vishay UNR-4325 2 Ω precision burden resistor I-V curve with linear fit.

the pulse was of such short duration that the case didn't reach the same temperature, assuming that thermal contact was good. This means that the heat sink is not important for dissipating the heat generated by such short pulses, as stated in [20]. The first and last ten minutes of the temperature versus time plot are stable, therefore the increase in baseline temperature over time can be attributed to an increase in room temperature rather than an insufficient cooling period between pulses. In summary, the resistor did not perform as expected, and the design must be revised. This may involve selecting a higher powered resistor or using up to four higher resistance UNR 4-325 resistors to achieve the desired resistance and power rating. Although desirable, it may prove difficult to find a higher power resistor with a thermal resistance coefficient suitable for the application, and if more resistors are required, the rack mount box design will have to be suitably lengthened. Furthermore, the manufacturer should be contacted again to clarify the maximum power rating of the resistors.

The broken resistor was opened up to investigate the failure mode and so that the foil could be weighed to feed into the maximum power calculation in the introduction. Fig

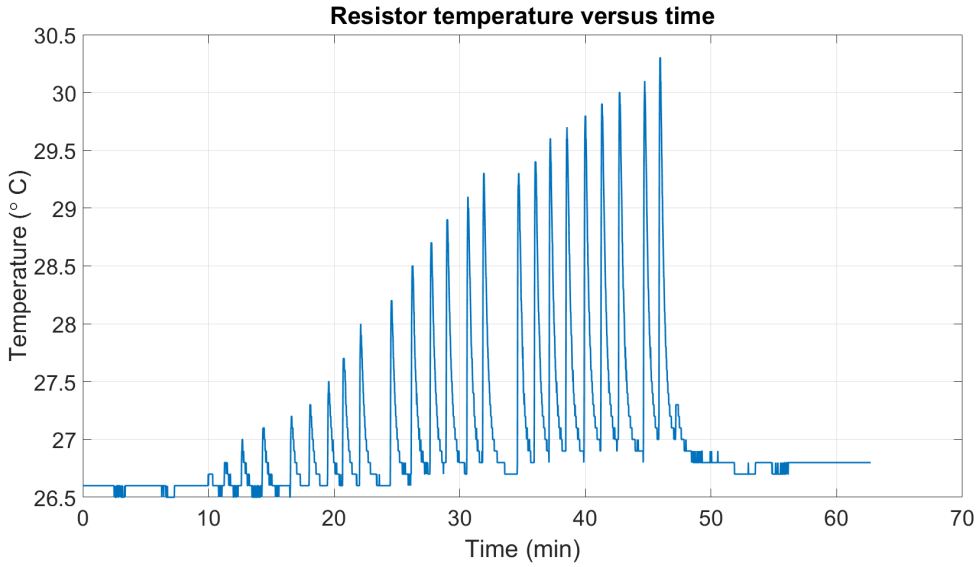

Figure 4.10: Resistor case temperature versus time for duration of test.

4.11 shows the resistor foil damage due to heating. The foil was difficult to remove, but the removed section of foil weighed 0.00 ± 0.01 g, so the reason for such a low power estimate was not due to the fact that the mass assumption was too small, but for some unknown reason.

The present rack mount box holds two 150 mm long heat sinks. Through correspondence with the manufacturer, the AST has learned that to meet the 50 W specification, the resistor requires a heat sink with thermal resistance of 0.1 °CW^{-1}. This considerably narrows the choice of heat sink.

4.7 Alternative burden resistor testing

Two alternative resistors; Ohmite 850F1ROE and Arcol HS150 were selected with higher power ratings and substantially shorter lead times than the UNR 4-3425. This required a compromise in TCR as the resistors have TCRs of 50 and 100 ppm $°C^{-1}$ respectively. The resistors were characterised in the same way as is described in Section 4.6.2. Fig 4.12 and

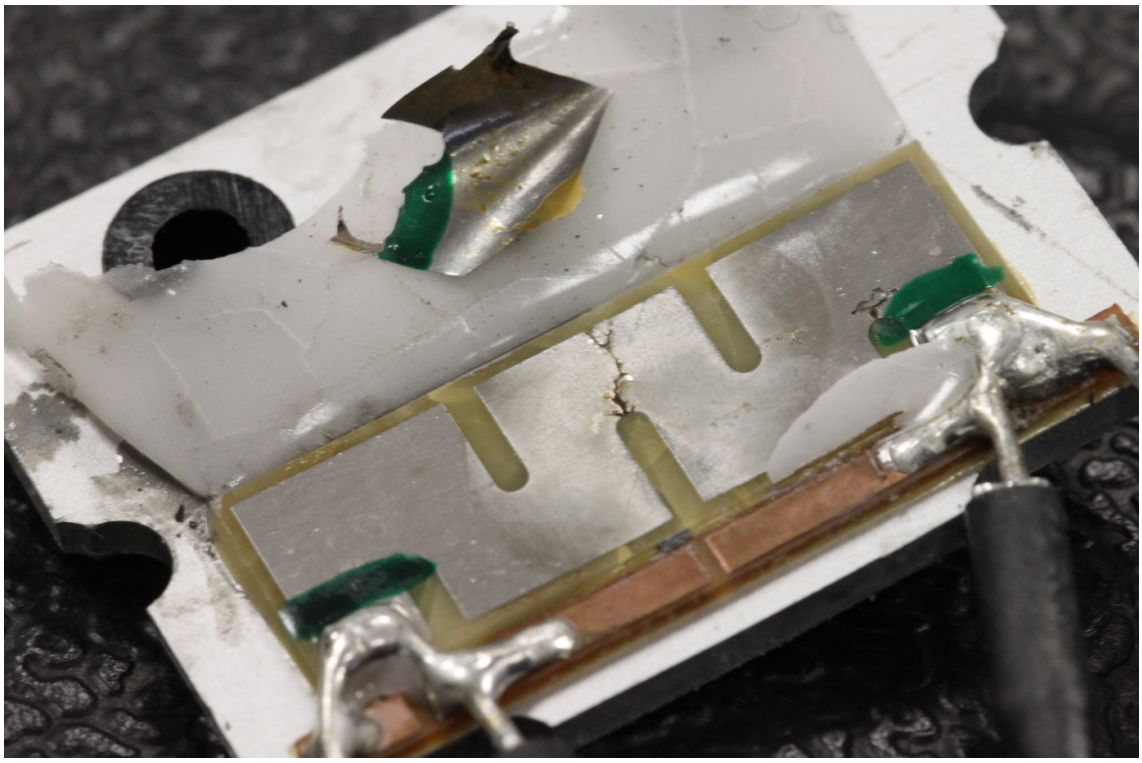

Figure 4.11: 2 Ω resistor foil damage due to heating. The resistor construction comprises a PPS / AlN / Al_2O_3 casing (removed), thermal pad (seen above foil), two Cu strips to which leads are soldered, NiCr foil, AlN / Al_2O_3 substrate (yellow), and Al heatsink.

Fig 4.13 display the results of I-V characterisation of the each of the resistors respectively, along with case temperature versus time, which was monitored via USB thermocouple, attached with 3M thermal grease. Both resistors survived the maximum applied current, which was limited by the 22 A oil resistor current rating, and as such the Ohmite resistor is recommended as an alternative to the UNR 4-34245 as this has the lower TCR. It can be seen in the figures below, that the current exceeds the 22 A rating of the oil resistor. This was due to a resistance measurement error on the DMM; another DMM was later used to correct this and the resistance values used in calculations adjusted accordingly. The data that exceeds 22 A cannot therefore be trusted as proof of linearity above this current value.

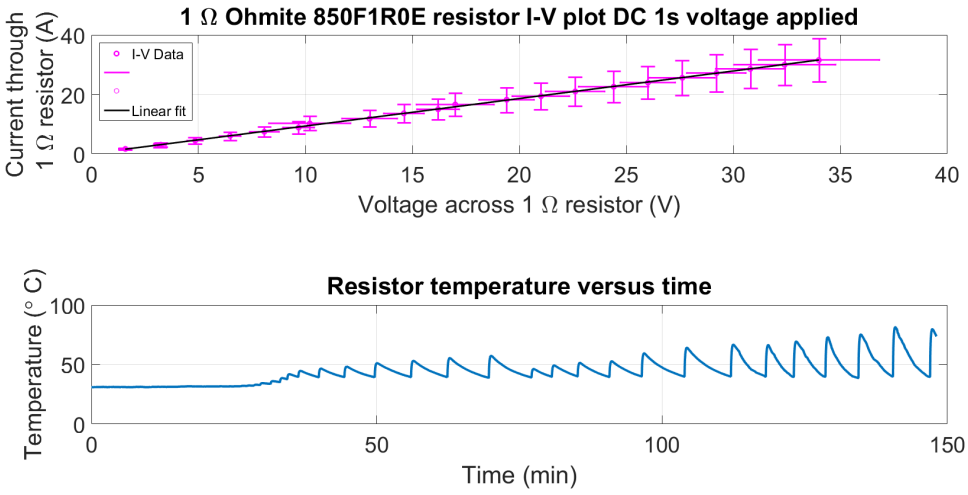

Figure 4.12: Top: Ohmite 850F1ROE 1Ω burden resistor I-V curve with linear fit. Bottom: Resistor case temperature versus time for duration of experiment. An error of corresponding to 10 °C × 50 ppm °C^{-1} has been assumed for the temperature dependence of the oil standard resistor in the absence of a calibrated value.

4.8 Summary

To summarise, TVS diodes and a TRIAC were tested for their suitability in protecting the LVTs. The notable benefit of the TRIAC is that once it is operational, change in operational voltage due to heating or variable fault voltage is expected to be much less, if at all present based on the manufacturer specified maximum on state voltage of 1.5 V. This could provide for more reproducible compensation when compared to the TVS diodes, although at the expense of having less data to extrapolate the fault waveform from the distorted waveform if fault waveform measurement were indeed desirable. On the assumption that the PS can withstand up to 40 V_{pk} across its terminals, TVS SMCJ28CA is the most suitable candidate. This is due to the risk of diodes with lower breakdown voltages, reaching breakdown prematurely at low temperatures.

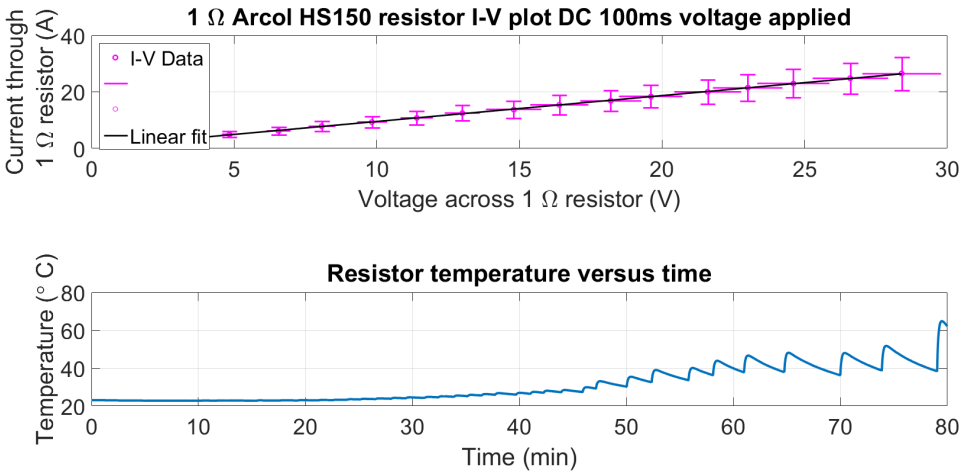

Figure 4.13: Top: Arcol 1Ω burden resistor I-V curve with linear fit. Bottom: Resistor case temperature versus time for duration of experiment. An error of corresponding to 10 °C × 50 ppm $°C^{-1}$ has been assumed for the temperature dependence of the oil standard resistor in the absence of a calibrated value.

The power rating of the CLR should be increased to 100 W to avoid shorting under worst case scenario faults, and its resistance should be no greater than 22 Ω - Vishay's 10 Ω LTO 100 resistor fits these criteria. A suitable heat sink and thermal pad for this resistor, meeting the criteria described in section 4.4.2 should be selected. As a contingency plan, in the case that it is found that the manufacturer recommended maximum PS voltage should not be exceeded, a modified TRIAC circuit is recommended. The phase and magnitude errors on transducer voltage measurement due to the RC filter inherent in the protection circuit design were examined, and a recommendation to commence further testing of the PS withstand voltage, specifically under DC offset, was made. Finally, a candidate with a higher power rating should replace the UNR 4-3425 burden resistor and should be tested with an appropriate heat sink. The Ohmite 850F1ROE resistor is suggested as an alternative.

Chapter 5

Conclusions and further work

In Chapter 1 fiber Bragg grating technology was introduced and applications highlighted. Conventional, alternative proposed and FBG-based voltage and current sensors were described and the sources of error in current measurement by this method discussed. The effects of ageing and deageing on the measurement accuracy of optical fibre and PS (piezoelectric stack) based low voltage transducers (LVTs) were experimentally investigated, and a fatigue test to select an optimal FBG bonding method reported on. Finally, the proposed protection circuitry for the prototype LVTs was revised, based on experimental and theoretical considerations.

In Chapter 2, the B parameter in the normalised OS degradation was found to be independent of pulse duration, voltage step decrease magnitude, voltage step increase magnitude frequency of applied AC voltage. DC offset voltages were observed to produce piezoelectric creep, however the dependence of the OS (optical sensitivity) on DC offset voltages was observed to differ between LVTs in the same experiment, suggesting that an interference between sensors may be present. An investigation into the possibility of an ageing - deageing transition was highlighted, but no such clear-cut transition has been found. This may be in part due to observed electrical interference between sensors electrically connected in parallel. The options regarding modification of ageing rate and compensation in software were presented and compensation selected as the easiest way to

proceed.

The ageing decays repeatability was investigated for an unpackaged LVT, with the B parameter exhibiting an approximately Gaussian distribution. Finally, hypothetical LVT interference was investigated and proposed to be electrical in nature, and obstacles to accurate temperature characterisation were highlighted. The observed dependence of the sensitivity of the OS to the phase of a transient fault waveform at the time of return to nominal voltage was highlighted and explained and the linear relationship between $\Delta\lambda_{\mathrm{Bav}}$ and ΔOS was discussed. Finally, the observed change in mean wavelength during change in OS at constant AC voltage does not appear to fit with the ageing explanation and instead shows the viscoelastic creep-like behaviour seen in the model of Muliana [48]. This model however, fall short of an explanation for the observed curves attributed to deageing.

Further work will include:

- An investigation into the effect of stack dimensions on ageing decay repeatability and reproducibility. The hypothesis presented in section 2.3.1 suggests that both may be improved with greater volume of piezoelectric material.
- Testing of the electrical interference hypothesis through repeating the experiments in which interference was observed, after introduction of unity gain voltage amplifiers to the circuit.
- If the introduction of voltage follower operational amplifiers to the test circuit does prove to remove the hypothetical interference effect, DC offset experiments can then be repeated to confirm or deny the presence of an interference effect producing poor reproducibility of LVT response in the results.
- Building a program to simulate the expected behaviour under a given run, informed by the model of Muliana, experimental results, and the effects of fatigue, creep, ageing and deageing.
- The effect of temperature on LVT response to a change in applied voltage should be

quantified in the range -5 to 40 °C corresponding to the temperature range within which accuracy limits are specified in the relevant technical standard.

- Inclusion of transformer inrush in tests and compensation procedures.
- Repeating test in which frequency was the independent variable, whilst monitoring piezoelectric stack surface temperature, to determine whether self-heating occurs and, therefore, gain insight into whether this is a factor in the observed OS degradation.

In the accelerated life testing of Chapter 3, both sensor builds survived the full 20 EY 50 Hz duration of the fatigue test without catastrophic failure. Beyond this, results were inconclusive due to unforeseen changes in output voltage upon changing frequency on the signal generator used, and too many variables including fibre pretension, epoxy material, and stack length.
Further work may:

- Investigate the effects of ageing of the viscous gel used in packaging on LVT through-life accuracy. Such an investigation may include vibration testing of the LVT.
- Investigate the effects of temperature in the range -5 to 40 °C on the LVTs fatigue response.
- Repeat the test with greater control of humidity, applied voltage and temperature, with fewer variables between transducers, a larger sample size, an independent reference for degradation in piezoelectric stack maximum displacement, and a better characterised FBG interrogator.

The protection circuit review of Chapter 4 presented the following conclusions. On the assumption that the PS can withstand up to 40 V_{pk} across its terminals, TVS SMCJ28CA was selected as the most suitable transient voltage suppression device for protection of the LVT. It was recommended that the current limiting resistor power rating should be increased to 100 W to avoid shorting under worst case scenario faults, and its resistance

should be no greater than 18 Ω - Vishay's 10 Ω LTO 100 resistor fits these criteria. A suitable heat sink and thermal pad for this resistor, meeting the criteria described in section 4.4.2 should be selected. As a contingency plan, in the case that it is found that the manufacturer recommended maximum PS voltage should not be exceeded, a modified TRIAC (triode for alternating current) circuit is recommended. Finally, a candidate with a higher power rating should replace the UNR 4-3425 burden resistor. The Ohmite 850F1ROE resistor is suggested as an alternative.

Further work should:

- Test an alternative burden resistor with a suitable heat sink.
- Perform statistically valid testing of PS withstand voltage, in particular under DC offset conditions.
- Perform testing of the piezoelectric stacks response again, whilst monitoring stack surface temperature, to test the hypothesis that the observed distortion in response was indeed due to increasing stack temperature due to self heating.

Bibliography

[1] BS EN 60044-8:2002 Instrument transformers - Part 8: Electronic current transformers. Technical report, BSI, 2002.

[2] C. B. Olausson, et al. Quantitative investigation of the refractive-index modulation within the core of a fiber Bragg grating. *Optics Express*, 18(16):16345, 2010.

[3] P. J. G. Orr. *Magnetophotonic Sensor Systems for Fibre-Optic Magnetic Diagnostics in Tokamak Fusion Reactors*. PhD thesis, 2011.

[4] G. Meltz, W. W. Morey, and W. H. Glenn. Formation of Bragg gratings in optical fibers by a transverse holographic method. 14(15):823–825, 1989.

[5] J. Canning. Fibre gratings and devices for sensors and laser. *Laser and Photonics Reviews*, 2(4):275–289, 2008.

[6] B. O. Guan, et al. Formation and applications of the secondary fiber bragg grating. *Sensors*, 17(2), 2017.

[7] Corning. Corning ® SMF- 28 ® Ultra Optical Fiber Datasheet. Technical Report November, 2014.

[8] Y.-J. Rao. In-fibre Bragg grating sensors. *Measurement Science and Technology*, 8:355–375, 1997.

[9] K. Haase. Strain sensors based on bragg gratings. *IMEKO 20th TC3, 3rd TC16 and 1st TC22 International Conference Cultivating metrological knowledge*, 2007.

[10] X. Feng, et al. Determination of the coefficient of thermal expansion with embedded long-gauge fiber optic sensors. *Measurement Science and Technology*, 21(6):065302, 2010.

[11] T. Wang, et al. Temperature and strain characterization of regenerated gratings. *Optics letters*, 38(3):247–9, 2013.

[12] P. Niewczas, et al. Temperature compensation for a piezoelectric fiber-optic voltage sensor. *2006 IEEE Instrumentation and Measurement Technology Conference Proceedings*, (April):1994–1998, 2006.

[13] G. M. H. Flockhart, et al. Quadratic behavior of fiber Bragg grating temperature coefficients. *Applied optics*, 43(13):2744–51, 2004.

[14] B. Zhang and M. Kahrizi. High-Temperature Resistance Fiber Bragg Grating. *IEEE Sensors Journal*, 7(4):586–591, 2007.

[15] H. Z. Yang, et al. In-fiber gratings for simultaneous monitoring temperature and strain in ultrahigh temperature. *IEEE Photonics Technology Letters*, 27(1):58–61, 2015.

[16] M. Perry, et al. High stress monitoring of prestressing tendons in nuclear concrete vessels using fibre-optic sensors. *Nuclear Engineering and Design*, 268:35–40, 2014.

[17] M. Jones. A sensitive issue. *Nature Photonics*, 40(6):470–1, 2005.

[18] R. C. Tennyson, et al. Structural health monitoring of innovative bridges in Canada with fiber optic sensors. *Smart Materials and Structures*, 10:560–573, 2001.

[19] W. Shen, et al. Application study on FBG sensor applied to hull structural health monitoring. *Optik - International Journal for Light and Electron Optics*, 126(17):1499–1504, 2015.

[20] G. Kister, et al. Methodology and integrity monitoring of foundation concrete piles using Bragg grating optical fibre sensors. *Engineering Structures*, 29:2048–2055, 2007.

[21] Y. Zhao, Y. Liao, and S. Lai. Simultaneous measurement of down-hole high pressure and temperature with a bulk modulus and FBG sensor. *IEEE Photonics Technology Letters*, 14(11):1584–1586, 2002.

[22] G. Fusiek, P. Niewczas, and J. McDonald. Design of a highly accurate optical sensor system for pressure and temperature monitoring in oil wells. *2009 IEEE Instrumentation and Measurement Technology Conference*, (May):5–7, 2009.

[23] Optical Strain Gage os3200. Technical report, Micron Optics.

[24] Fiberpro. MSS-1700 FBG strain sensor datasheet. Technical report, Fiberpro.

[25] I. Photonics. I-MON OEM interrogator datasheet. Technical report.

[26] J. Jung, Y. Wook Lee, and B. Lee. High-Resolution Interrogation Technique for Fiber Bragg Grating Sensor Using Long-Period Fiber Grating Pair and Erbium-Doped Fiber. *Journal of the Optical Society of Korea*, 6(1):5–12, 2002.

[27] N. Pilling, R. Holmes, and G. Jones. Optical fibre current measurement system using liquid crystals and chromatic modulation. *IEE Proceedings C Generation, Transmission and Distribution*, 140(5):351, 1993.

[28] D. Reilly, et al. A fiber-Bragg-grating-based sensor for simultaneous AC current and temperature measurement. *IEEE Sensors Journal*, 6(6):1539–1542, 2006.

[29] A. Zvedzdin and V. Kotov. *Modern magnetooptics and magnetooptical materials*. IOP Publishing, 1997.

[30] P. M. Mihailovic, S. J. Petricevic, and J. B. Radunovic. Compensation for Temperature-Dependence of the Faraday Effect by Optical Activity Temperature Shift. 13(2):832–837, 2013.

[31] K. Bohnert, et al. Optical fiber sensors for the electric power industry. *Optics and Lasers in Engineering*, 43(3-5):511–526, 2005.

[32] M. Takahashi, K. Sasaki, and N. Member. Optical Current Sensor for DC Measurement. pages 440–443, 2002.

[33] Alstom Grid technical brochure. Optical Current Transformer COSI-NXCT. pages 1–4, 2015.

[34] Arteche. SDO OCT. Technical report, 2018.

[35] Y. Ouyang, et al. A current sensor based on the giant magnetoresistance effect: design and potential smart grid applications. *Sensors (Basel, Switzerland)*, 12(11):15520–41, 2012.

[36] D. Yang, et al. Design and Realization of a Novel Compact Fluxgate Current Sensor. *IEEE Transactions on Magnetics*, 51(3):1100–1103, 2015.

[37] Y.-P. Tsai, K.-L. Chen, and N. Chen. Design of a Hall effect current microsensor for power networks. *IEEE Transactions on Smart Grid*, 2(3):421–427, 2011.

[38] F. Pan, et al. An optical AC voltage sensor based on the transverse Pockels effect. *Sensors (Basel, Switzerland)*, 11(7):6593–602, 2011.

[39] G. Fusiek, P. Orr, and P. Niewczas. Temperature-Independent High-Speed Distributed Voltage Measurement using Intensiometric FBG Interrogation. 1(1):2–7, 2013.

[40] Q. Zhou, et al. Study and Experiment on Non-Contact Voltage Sensor Suitable for Three-Phase Transmission Line. *Sensors*, 16(1):40, 2015.

[41] P. Niewczas, et al. Design and evaluation of a pre-prototype hybrid fiber-optic voltage sensor for a remotely interrogated condition monitoring system. *Conference Record*

- *IEEE Instrumentation and Measurement Technology Conference*, 3(4):2369–2374, 2004.

[42] G. Fusiek, P. Niewczas, and J. McDonald. Feasibility study of the application of optical voltage and current sensors and an arrayed waveguide grating for aero-electrical systems. *Sensors and Actuators A: Physical*, 147(1):177–182, 2008.

[43] J. Nelson. Optically Interrogated Current Sensor (internal report). Technical report, University of Strathclyde, 2015.

[44] P. Niewczas and J. Mcdonald. WO 2005/029005 A1.

[45] P. Orr, et al. An optically-interrogated rogowski coil for passive, multiplexable current measurement. *IEEE Sensors Journal*, 13(6):2053–2054, 2013.

[46] D. Damjanovic. Ferroelectric, dielectric and piezoelectric properties of ferroelectric thin films and ceramics. *Reports on Progress in Physics*, 61(9):1267, 1999.

[47] PI Ceramic. PI Web page.

[48] A. Muliana. Time dependent behavior of ferroelectric materials undergoing changes in their material properties with electric field and temperature. *International Journal of Solids and Structures*, 48(19):2718–2731, 2011.

[49] G. Fusiek, et al. Hysteresis compensation for a piezoelectric fiber optic voltage sensor. *Optical Engineering*, 44(11):1–6, 2005.

[50] R. Szewczyk. Computational Problems Connected with Jiles-Atherton Model of Magnetic Hysteresis Jiles-Atherton Model of Magnetic Hysteresis. In *Recent Advances in Automation, Robotics and Measuring Techniques 267*, pages 275–283, 2014.

[51] D. C. Jiles and D. L. Atherton. Theory of ferromagnetic hysteresis. *Journal of Magnetism and Magnetic Materials*, 61(1-2):48–60, 1986.

[52] Y. A. Genenko, et al. Mechanisms of aging and fatigue in ferroelectrics. *Materials Science and Engineering B: Solid-State Materials for Advanced Technology*, 192(C):52–82, 2015.

[53] D. C. Lupascu, Y. A. Genenko, and N. Balke. Aging in ferroelectrics. *Journal of the American Ceramic Society*, 89(1):224–229, 2006.

[54] A. Kholkin, et al. Interferometric study of piezoelectric degradation in ferroelectric thin films. *Microelectronic Engineering*, 29(1-4):261–264, 1995.

[55] M. Morozov and D. Damjanovic. Charge migration in Pb(Zr,Ti)O3 ceramics and its relation to ageing, hardening and softening. pages 1–20.

[56] W. A. Schulze and K. Ogino. Review of literature on aging of dielectric. *Ferroelectrics*, 87:361–377, 1988.

[57] L. Zhang and X. Ren. Aging behavior in single-domain Mn-doped BaTiO3 crystals: Implication for a unified microscopic explanation of ferroelectric aging. *Physical Review B - Condensed Matter and Materials Physics*, 73(9):17–19, 2006.

[58] A. L. Kholkin, et al. Piezoelectric and dielectric aging in Pb(Zr,Ti)O3 thin films and bulk ceramics. *Integrated Ferroelectrics*, 15(1-4):317–324, 1997.

[59] L. Laurson, et al. Modeling thermally activated domain wall dynamics in thin magnetic strips with disorder. *Journal of Physics: Conference Series*, 292(2):012008, 2011.

[60] H. Jung and D.-g. Gweon. Creep characteristics of piezoelectric actuators. *Review of Scientific Instruments*, 71(4):1896, 2000.

[61] D. Zhou and M. Kamlah. Determination of room-temperature creep of soft lead zirconate titanate piezoceramics under static electric fields. *Journal of Applied Physics*, 98(10):1–6, 2005.

[62] S. Sherrit et al. Piezoelectric multilayer actuator life test. *IEEE transactions on ultrasonics, ferroelectrics, and frequency control*, 58(4):820–8, 2011.

[63] Q. Y. Jiang, E. C. Subbarao, and L. E. Cross. Effect of composition and temperature on electric fatigue of La-doped lead zirconate titanate ceramics. *Journal of Applied Physics*, 75(11):7433–7443, 1994.

[64] Z. Luo, et al. Bipolar and unipolar fatigue of ferroelectric BNT-based lead-free piezoceramics. *Journal of the American Ceramic Society*, 94(2):529–535, 2011.

[65] D. Wang, Y. Fotinich, and G. P. Carman. Influence of temperature on the electromechanical and fatigue behavior of piezoelectric ceramics. *Journal of Applied Physics*, 83(10):5342–5350, 1998.

[66] V. Y. Shur, et al. Kinetic approach to fatigue phenomenon in ferroelectrics. *Journal of Applied Physics*, 90(12):6312–6315, 2001.

[67] A. Bratovsky and A. Levanyuk. Abrupt Appearance of the Domain Pattern and Fatigue of Thin Ferroelectric Films. *Physical Review Letters*, 87(17):179702, 2001.

[68] M. Hinterstein, et al. Structural description of the macroscopic piezo- and ferroelectric properties of lead zirconate titanate. *Physical Review Letters*, 107(7):10–13, 2011.

[69] S. Pojprapai, et al. Frequency effects on fatigue crack growth and crack tip domain-switching behavior in a lead zirconate titanate ceramic. *Acta Materialia*, 57(13):3932–3940, 2009.

[70] N. Zhang, et al. Frequency spectrum of ferroelectric fatigue in PLZT ceramics. *Ferroelectrics*, 259(1):109–114, 2001.

[71] J. Lee, et al. Effects of crystalline quality and electrode material on fatigue in Pb(Zr,Ti)O3 thin film capacitors. *Applied Physics Letters*, 63(1):27–29, 1993.

[72] W. L. Warren, et al. Electronic domain pinning in Pb(Zr,Ti)O3 thin films and its role in fatigue. *Applied Physics Letters*, 65(8):1018–1020, 1994.

[73] P. V. Lambeck and G. H. Jonker. The nature of domain stabilization in ferroelectric perovskites. *Journal of Physics and Chemistry of Solids*, 47(5):453–461, 1986.

[74] C. M. Fancher, et al. The contribution of 180Âř domain wall motion to dielectric properties quantified from in situ X-ray diffraction. *Acta Materialia*, 126:36–43, 2017.

[75] U. Robels and G. Arlt. Domain wall clamping in ferroelectrics by orientation of defects. *Journal of Applied Physics*, 73(7):3454–3460, 1992.

[76] K. Carl and K. H. Härdtl. Electrical after-effects in Pb(Ti, Zr)O3 ceramics. *Ferroelectrics*, 17(1):473–486, 1977.

[77] D. Berlincourt and H. H. A. Krueger. Domain processes in lead titanate zirconate and barium titanate ceramics. *Journal of Applied Physics*, 30(11):1804–1810, 1959.

[78] B. Jaffe, W. R. Cook, and H. Jaffe. Chapter 7 - solid solutions of Pb(Ti, Zr, Sn, Hf)O3. In *Piezoelectric Ceramics*, pages 135–183. Academic Press Inc., 1971.

[79] A. Ibrahim, et al. *Morphotropic Phase Boundary in Ferroelectric Materials*. InTech, 2011.

[80] G. H. Jonker. Nature of Aging in Ferroelectric Ceramics. *Journal of American Ceramic Society*, 55(1):57–58, 1972.

[81] K. W. Wu and W. A. Schulze. Aging of the weak-field dielectric response in fine-grain and coarse-grain ceramic BaTiO3. *Journal of the American Ceramic Society*, 75(12):3390–3395, 1992.

[82] H. Zhang, et al. Piezoelectric and dielectric aging of Bi0.5(Na 0.82K0.18)0.5TiO3 lead-free ferroelectric thick films. *Journal of Applied Physics*, 107(12):0–6, 2010.

[83] W. L. Cherry and R. Adler. Piezoelectric effect in polycrystalline Barium Titanate. *Physical Review*, 72(10):981–982, 1947.

[84] B. Jaffe, W. R. Cook, and H. Jaffe. Chapter 5 - Barium Titanate. In *Piezoelectric Ceramics*, pages 53–114. Academic Press Inc., 1971.

[85] M. G. Cain. Degradation of Piezoelectric Materials. *NPL Report CMMT (A) 148*, (January), 1999.

[86] M. H. Lente and J. A. Eiras. Interrelationship between self-heating and ferroelectric properties in PZT ceramics during polarization reorientation. *IOP Science*, 12:5939–5950, 2000.

[87] F. Mekic and Z. Gajic. Power Transformer Characteristics and Their Effect on Protective Relays. Technical report, ABB, 2006.

[88] W. R. Broughton, R. D. Mera, and G. Hinopoulos. The performance of adhesive joints: project PAJ3 - combined cyclic loading and hostile environments 1996-1999; report no. 8 - cyclic fatigue testing of adhesive joints test method assessment. Technical report, NPL, 1999.

[89] S. Sherrit, et al. Multilayer Piezoelectric Stack Actuator Characterization. *California Institute of Technology*, pages 692909–692909–12, 2008.

[90] K. T. Wan, C. K. Y. Leung, and N. G. Olson. Investigation of the strain transfer for surface-attached optical fiber strain sensors. *Smart Materials and Structures*, 17(3):035037, 2008.

[91] S. C. Her and C. Y. Tsai. Strain measurement of fiber optic sensor surface bonding on host material. *Transactions of Nonferrous Metals Society of China (English Edition)*, 19(SUPPL. 1), 2009.

[92] APC International. Piezo-Mechanics: An Introduction. Technical report, APCInternational, 2003.

[93] B. D. Metz-Noblat, F. Dumas, and C. Poulain. Cahier technique no 158: Calculation of short-circuit currents. Technical Report 158, Schneider Electric, 2005.

[94] Instrument Transformers Ltd. Personal communication, 2017.

[95] AST. Internal personal correspondence, 2017.

[96] ST Microelectronics. P6KE Transil, transient voltage surge suppressor datasheet. pages 1–9, 2012.

[97] ON Semiconductor. BTA30-800CW3G TRIAC datasheet. pages 1–6, 2008.

[98] BS EN 61869-9. Technical report, British Standards Institution, 2013.

[99] P6KE series transient voltage suppression diodes datasheet. Technical report, Littelfuse, 2015.

[100] Littelfuse. Transient Voltage Suppression Diodes SMCJ series datasheet. 2015.

[101] TVS peak pulse power, pulse duration & temperature. Technical report, Protek Devices.

[102] Innovation funding incentive annual report. Technical report, National Grid, 2011.

[103] BS EN 60115-2:2011+A11:2015. Technical report, BSI, 2015.

[104] Powertron (Vishay Precision Group). USR UNR 4-3425 Datasheet. Technical report, 2016.

[105] LTO 100 datasheet. Technical report, Vishay Sfernice, 2016.

[106] Fischer Elektronik WLFT 404 Thermally conductive foil datasheet. Technical report.

[107] Synaptec. Personal communication, 2017.

[108] Vishay. Shunts, current shunts and current-sensing resistors. Technical report.

[109] G. Andersson. Modelling and analysis of electric power systems. Technical report, EEH Power Systems Laboratory, ETH Zurich, 2008.

[110] Product catalogue. Technical report, Littelfuse, 2013.

Appendix A

LVT construction

This section describes in detail the construction of LVTs used in this thesis, for the reader who may desire to test the reproducibility of results contained within.

A.1 Unpackaged LVTs

All FBGs used in experiments described within this thesis are 7 ± 1 mm FBGs coated with ~140 µm HD Microsystems PI 2525 polyimide written in Corning SMF-28 single mode fibre. The FBGs have an FWHM around 0.3 nm and are apodised with side lobe suppression ratios of >15 dB and reflectivities in excess of 70%. All FBGs are connectorised with fibre-pigtails. Following cleaning of the bonding surface with ethanol and lint free lens cleaning tissue, a minimal amount of Epotek Epoxy 301 is applied along the long axis of the piezoelectric stack, and the FBG bonded onto it.

A rudimentary jig for building sensors was assembled. An aluminium block with a tight-fit groove for holding the PS against the end-blocks during curing and very thin grooves for holding the fibre in place upon the stack was used to secure the sensor in place. Acrylate coated fibre was temporarily spliced to the polyimide coated FBG as this was easier to clamp than the polyimide-coated fibre due to its having larger diameter. An aluminium platform provided elevation so that plenty of fibre could be spliced onto the

FBG. Aluminium blocks with smooth curved edges to prevent fibre damage were used to suspend a weight from the fibre for pre-tensioning, and a clamp was used to hold the fibre in place at the other end. The set-up was placed in an oven with a grill, with the weights suspended below the grill. Fig 3.1 in Section 3 (left) shows a schematic of the set-up, and (right) shows a photograph of the aluminium fibre guide, platform, sensor holder and weight attached to nut and bolt.

The bolt was tightened such that the fibre was squeezed against the weight, securing it in place. On completion of the curing process, the clamped fibre ends were cut off at the polyimide side of the splices and the fibre was connectorised with acrylate-coated pigtails having angle polished fiber connectors.

The following lessons were learned in building sensors:

- When bonding an FBG directly to a PS with Epotek Epoxy 301, the ink used to mark the FBG position on the fibre is soluble in the un-cured epoxy.
- A screw mechanism for holding the PS in place during stack - end block curing should be used as the tight fitting solid block made it difficult to extract the sensor post - cure.

For the testing in Chapter 3, two sensors were assembled, one consisting of an FBG directly epoxied along the full length of a brand new PICMA p883-51 PS ($3 \times 3 \times 18$ mm) and another with the fibre epoxied to $3 \times 4 \times 4$ mm alumina end blocks with grooves suspended above a shorter brand new PICMA p883-11 PS ($3 \times 3 \times 9$ mm). Epotek Epoxy 353ND cured at 100 ° C for one hour was used for the sensor possessing end blocks whilst Epotek Epoxy 301 cured at room temperature for 24 hr was used for the directly bonded sensor. No fibre pretension was applied to the directly-bonded sensor whilst a 250 g weight was used to pretension the sensor with end blocks.

Bonding surfaces were cleaned with isopropanol, which was allowed time to evaporate, before application of epoxy. Additionally, reasonable care was taken to ensure that the width of the epoxy applied orthogonal to the fibre axis and the epoxy thickness between

the bonded substrates were minimised and equal on both sensors. This was done by inspection only, by slowly incrementally adding the mixed epoxy to the substrate by hand using a narrow-headed firm cotton swab.

A.2 Packaged LVTs

The packaged LVTs described in this thesis were produced by Optocap Ltd. The actuated stack indirectly transfers strain to the FBG via the route; end block - epoxy bond - polyimide coat - fibre cladding - fibre core. The assembly is seen in Fig **??**. A polyimide coated, pre-stressed SM fibre with inscribed 7 mm FBG is suspended parallel to the stack actuation axis, with FBG aligned with the stacks centre. The PS used is PI Ceramic's PI-883.11 with dimensions $3 \times 3 \times 9$ mm. The transducer is hermetically sealed in an kovar 'butterfly' package with four feedthroughs comprising of two fibre feedthroughs and two kovar pin feedthroughs. The lid is sealed in a 100% nitrogen atmosphere using rolled seam electrical resistance welding. Glass frit is used to seal the kovar package to the fibre at the fibre-feedthrough interface, following stripping of the polyimide coating. kovar pins suspend the actuator within a viscous Nusil R-2614 gel encapsulant which is filled to within one mm of the lids inner surface. The pins are electrically connected to the PS via soldered wire leads. A Bi-Sn-Ag solder was used in bonding to the piezo stack electrodes and providing a hermetic seal through connection of a fibre stainless steel ferrule to pipes on the sensor packaging.

Appendix B

TVS device I-V characterisation results

B.1 Transil TVS diode I-V Plots for 10 ms DC V_{IN}

Fig B.1 shows the averages of linear fits to the I-V curves for positive and negative (arbitrarily defined here as diode and voltage polarity were not noted) DC operation of the TVS diodes. Only one voltage polarity was used to characterise P6KE27CA as the clamping waveform displayed an exponential decay rather than a stable value. This diode had previously been exposed to 1 s AC 126.0 ± 5.8 $\mathrm{V_{pkpk}}$ during which time the 10 Ω CLR failed, and was found to behave normally for a 20 ms AC waveform immediately after having done so, however this is still the likely cause of the asymmetric behaviour described. The most significant contribution to the TVS voltage and current measurement uncertainty comes from the oscilloscope. The DC V_{IN} used was 10 ms in duration. These DC curves can be used to represent a worse than worst case scenario of TVS diode performance owing to the fact that more heat is dissipated due the DC V_{IN} than a corresponding sinusoidal peak of the same peak voltage.

I-V curves were fit to the Shockley diode equation; however, fitting was poor and so linear fits were produced instead. Fig B.1 shows that TVS P6KE22CA, P6KE24CA

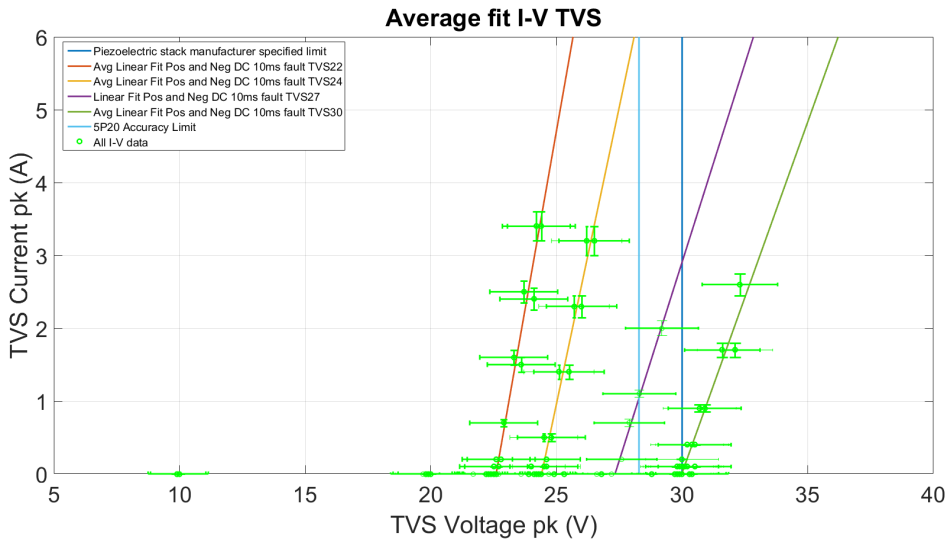

Figure B.1: Linear fit to I-V curve data under a 10 ms DC V_{IN} for TVS P6KE22CA (positive and negative voltage curve fit average for a single diode), P6KE24CA (positive and negative voltage curve fit average for a single diode), P6KE27CA (negative voltage curve fit for a single diode) and P6KE30CA (positive and negative voltage curve fit average for a single diode). The PS voltage limit is also shown.

and P6KE27CA, all clamp below the 30 V limit of the PS. The 5P20 class accuracy requirement demands that the sensor meets accuracy requirements up to 28.28 $\mathrm{V_{pk}}$, and TVS P6KE22CA, P6KE24CA or P6KE27CA all begin to clamp below this limit. TVS P6KE30CA clamps above the PS operating voltage limit making it unsuitable - the feasibility of using this diode depends upon whether the PS can tolerate a short excursion above the manufacturers specified operating limits and even then, diodes would have to be preselected for high breakdown voltages to avoid temperature fluctuations causing premature breakdown. This data has not been shifted in temperature for comparison with the datasheet breakdown voltage values as the voltage errors are already too large for a good comparison.

B.2 Transil TVS diode I-V Plots for 20 ms AC $V_{\mathbf{IN}}$

I-V curves of one TVS P6KE22CA, and three TVS P6KE24CA, TVS P6KE27CA and TVS P6KE30CA diodes were fit to the Shockley diode equation, however fitting was again poor and so linear fits were produced instead. These linear fits were then averaged and are plotted in Fig B.2 along with the PS voltage withstand (sensor limit).

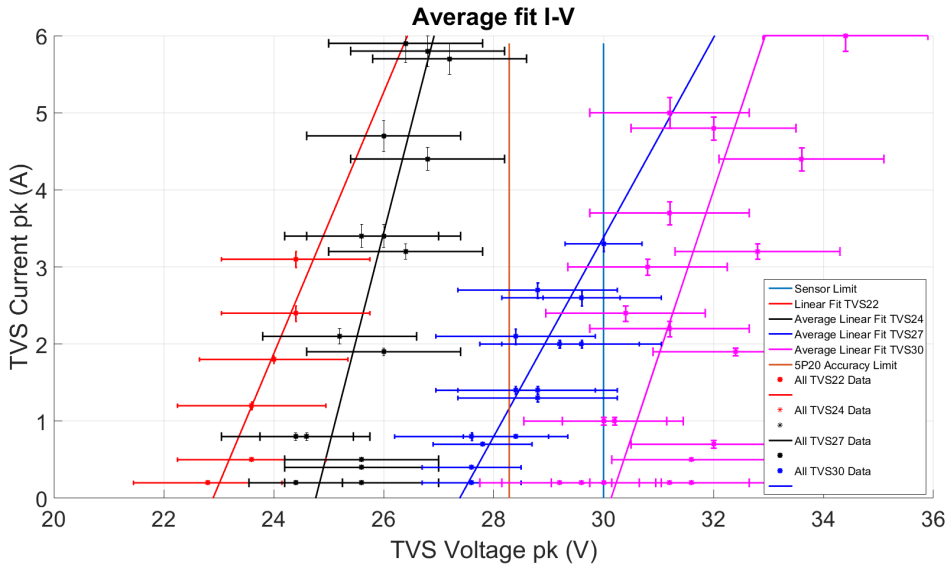

Figure B.2: Linear fits to I-V curve for the data obtained for TVS P6KE22CA, and the average of three runs on different diodes of the same class for TVS P6KE24CA, TVS P6KE27CA, and TVS P6KE30CA. Data superimposed onto fits.

This plot shows that TVS P6KE22CA, P6KE24CA and P6KE27CA again all clamp below the 30 V limit and again go into breakdown within the 5P20 accuracy requirement limits. In addition to this, TVS P6KE30CA clamps above the PS voltage withstand - the feasibility of using this diode again depends upon whether the sensor can tolerate a short excursion above PI ceramic's specified operating limits. This data has again, not been shifted in temperature for comparison with the datasheet breakdown voltage values as the voltage errors are already too large for a good comparison.

B.3 Littelfuse TVS diode I-V characterisation

The range of manufacturer specified breakdown voltages for the ST Transil P6KE27CA TVS diodes is 25.7-28.4 V, whilst that of the SMCJ24CA diodes is 26.7-29.5 V_{pk}. Thus the Littelfuse diodes are seemingly more suitable than their Transil counterparts for breaking down after the 5P20 accuracy limit. Given that the optical current sensors must satisfy 5P20 accuracy requirements up to 20 V_{RMS} (28.3 V_{pk}) it is desirable to either a) preselect for diodes with clamping voltages in this range and/or b) place additional diodes in series with the TVS diode to effectively shift the breakdown voltage by 0.7 V.

Fig B.3 shows temperature compensated I-V data for five Littelfuse SMCJ24CA TVS diodes [110] with linear fit to all those value pairs whose current exceeds 0.1 A. DC voltages were applied with the Chroma voltage source for a period of 10 ms. As before, room temperature was maintained at $19 \pm 0.3°$ C. There is a slight overshoot on the voltages measured on the oscilloscope. This has been attributed to either the oscilloscope or the voltage source. In order to obtain Fig B.3, the data has been averaged across the width of the DC pulse so the values shown are a slight overestimate of the actual values. The improvement in measurement accuracy on this data when compared to that used for the Transil diodes is due to using a different oscilloscope.

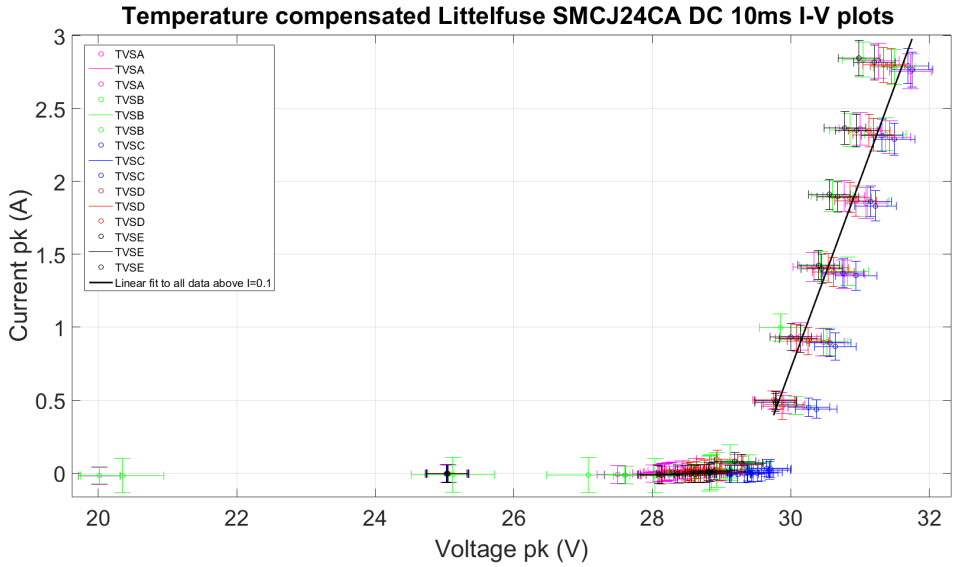

Figure B.3: Temperature compensated I-V curves for five Littelfuse SMCJ24CA TVS diodes with linear fit to all those value pairs whose current exceeds 0.1 A.

The voltage, current and error data have been corrected for temperature to compare the breakdown voltage with that specified on the datasheet. The linear fit was then extrapolated to 1 mA as this is the current the manufacturer uses to define the breakdown voltage. The result is $V_{BR} = 29.4 \pm 2.8$ V where the voltage error quoted here comes from the error in the gradient and slope of the fit. This falls within the manufacturer stated tolerance of 28.1 ± 1.4 V suggesting that the datasheet breakdown voltages are applicable to the present application.

If a voltage of 60 V_{pk} were to be applied across the burden resistor, then the current would be approximately 30 V/10 Ω = 3 A_{pk}. Thus if the 30 V limitation on PS operation holds, this diode should not be used, as the clamping voltage is seen to exceed this value by 1.5 V in Fig B.3.

B.4 TRIAC I-V curves

The TRIAC operates when a current of 75 mA is applied to the gate, or the voltage across the gate and terminal 2 (defined on the datasheet) exceeds the gate non trigger voltage of 0.15 V. Fig B.4 shows TRIAC I-V curve for positive and negative (arbitrarily defined) DC V_{IN}.

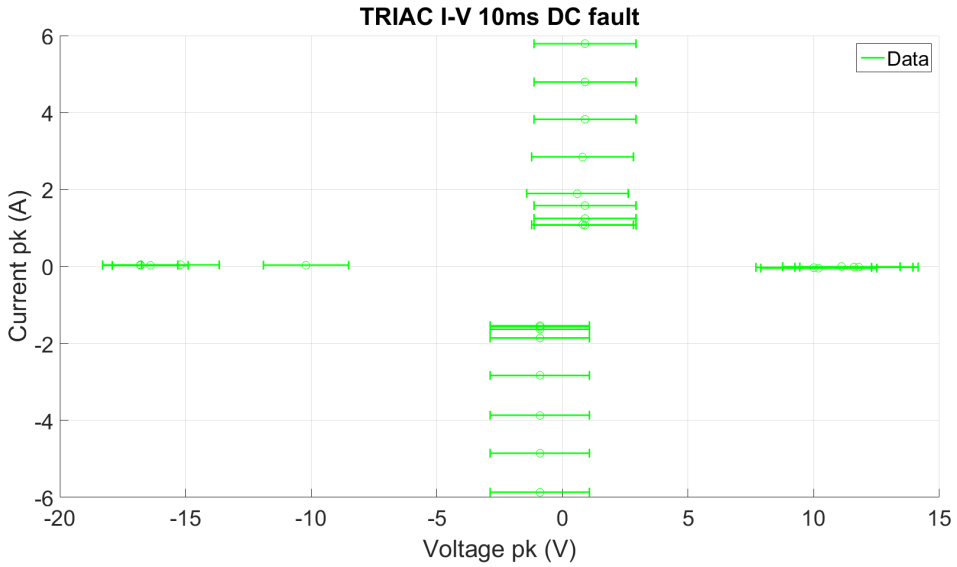

Figure B.4: I-V curve for TRIAC BTA30-800CW3G.

Under AC V_{IN}, the crowbar on first half period appeared to kick in at 12.1 V whilst crowbar on second half period took between 16.1 and 16.6 V to kick in. Under DC V_{IN} the positive (arbitrarily defined) crowbar kicked in at 13.6 V, and the negative crowbar kicked in at 18.8 V. These values are far too low - a higher resistance is recommended to replace the 1 kΩ resistor and limit the gate current, e.g. 30/16.6 × 1 kΩ ~1.8 kΩ.

Although the TRIAC circuit needs tweaking in this experiment, the simplest and recommended solution to the protection problem is the TRIAC option in the event that the PS fails at 30 $\mathrm{V_{pk}}$.